

**Search for
Lepton-Flavour-Violating Processes
in the Electron-Muon Channel
with the 2015 CMS Data**

von

Henning Keller

Masterarbeit in Physik

vorgelegt der
Fakultät für Mathematik, Informatik und
Naturwissenschaften der RWTH Aachen

angefertigt im
III. Physikalischen Institut A

bei
Prof. Dr. Thomas Hebbeker

Zweitgutachter
Prof. Dr. Christopher Wiebusch

September 2016

Eidesstattliche Versicherung

Name, Vorname

Matrikelnummer (freiwillige Angabe)

Ich versichere hiermit an Eides Statt, dass ich die vorliegende Arbeit/Bachelorarbeit/
Masterarbeit* mit dem Titel

selbständig und ohne unzulässige fremde Hilfe erbracht habe. Ich habe keine anderen als
die angegebenen Quellen und Hilfsmittel benutzt. Für den Fall, dass die Arbeit zusätzlich auf
einem Datenträger eingereicht wird, erkläre ich, dass die schriftliche und die elektronische
Form vollständig übereinstimmen. Die Arbeit hat in gleicher oder ähnlicher Form noch keiner
Prüfungsbehörde vorgelegen.

Ort, Datum

Unterschrift

*Nichtzutreffendes bitte streichen

Belehrung:

§ 156 StGB: Falsche Versicherung an Eides Statt

Wer vor einer zur Abnahme einer Versicherung an Eides Statt zuständigen Behörde eine solche Versicherung falsch abgibt oder unter Berufung auf eine solche Versicherung falsch aussagt, wird mit Freiheitsstrafe bis zu drei Jahren oder mit Geldstrafe bestraft.

§ 161 StGB: Fahrlässiger Falscheid; fahrlässige falsche Versicherung an Eides Statt

(1) Wenn eine der in den §§ 154 bis 156 bezeichneten Handlungen aus Fahrlässigkeit begangen worden ist, so tritt Freiheitsstrafe bis zu einem Jahr oder Geldstrafe ein.

(2) Strafflosigkeit tritt ein, wenn der Täter die falsche Angabe rechtzeitig berichtigt. Die Vorschriften des § 158 Abs. 2 und 3 gelten entsprechend.

Die vorstehende Belehrung habe ich zur Kenntnis genommen:

Ort, Datum

Unterschrift

Abstract

This thesis is concerned with the search for lepton-flavour-violating processes. The electron-muon final state is studied in 2015 CMS data with an integrated luminosity of 2.7 fb^{-1} of proton-proton collisions at a centre-of-mass energy of 13 TeV. In this search no evidence for physics beyond the standard model is observed in the invariant electron-muon mass spectrum. Upper limits on the cross section times branching ratio have been set on several theories extending the standard model and predicting charged lepton flavour violation. Scenarios of resonant tau sneutrino production in R-parity violating supersymmetry are excluded for masses below 1.0 TeV for couplings $\lambda_{132} = \lambda_{231} = \lambda'_{311} = 0.01$ and below 3.3 TeV for $\lambda_{132} = \lambda_{231} = \lambda'_{311} = 0.2$. In the context of the sequential standard model, a heavy gauge boson Z' with mass below 3.3 TeV is excluded. The observed invariant mass spectrum is also interpreted in terms of the non-resonant signal of quantum black hole production in models with extra dimensions. The observed exclusion limits range from 2.5 TeV for one extra dimension to 4.5 TeV for six extra dimensions. All limits are set at 95 % confidence level.

Zusammenfassung

Diese Masterarbeit beschäftigt sich mit der Suche nach leptonzahlverletzenden Prozessen. Der zu untersuchende Endzustand besteht aus einem Elektron und einem Myon und wird in CMS Daten aus 2015 mit einer integrierten Luminosität von 2.7 fb^{-1} von Protonenkollisionen bei einer Schwerpunktsenergie von 13 TeV analysiert. In dieser Suche wurde kein Hinweis auf neue Physik im Spektrum der invarianten Massenverteilung des Paares aus selektierten Elektronen und Myonen gefunden. Ausschlussgrenzen auf das Produkt von Wirkungsquerschnitt und Verzweigungsverhältnis wurden für mehrere Theorien, die das Standard Model erweitern und Leptonzahlverletzung mit geladenen Leptonen erlauben, bestimmt. Für Szenarien, in denen die resonante Produktion von einem Tau-Sneutrino in supersymmetrischen Modellen mit R-paritätsverletzenden Prozessen eine Rolle spielt, werden Massen des tau sneutrino von unter 1.0 TeV für Kopplungen von $\lambda_{132} = \lambda_{231} = \lambda'_{311} = 0.01$ und unter 3.3 TeV für $\lambda_{132} = \lambda_{231} = \lambda'_{311} = 0.2$ ausgeschlossen. Im Kontext des sequentiellen Standardmodells werden Massen eines neuen und schweren Eichbosons Z' von unter 3.3 TeV ausgeschlossen. Die beobachtete invariante Massenverteilung wird desweiteren in Bezug auf die nicht resonante Produktion von Schwarzen Quantenlöchern in Modellen mit zusätzlichen Raumdimensionen untersucht. Die beobachteten Ausschlussgrenzen reichen von 2.5 TeV für eine zusätzliche Raumdimension bis zu 4.5 TeV für sechs zusätzliche Raumdimensionen. Alle Ausschlussgrenzen wurden mit einem Konfidenzniveau von 95 % bestimmt.

Contents

1	Introduction	1
2	Theory	3
2.1	Standard Model of Particle Physics	3
2.1.1	Electroweak Theory	6
2.1.2	Quantum Chromo Dynamics	7
2.2	Beyond the Standard Model	8
2.2.1	R-Parity-Violating Supersymmetry	11
2.2.2	Sequential Standard Model Z'	15
2.2.3	Quantum Black Holes	16
3	Experimental Setup	19
3.1	General Information about the Large Hadron Collider	19
3.2	Compact Muon Solenoid	20
3.2.1	Coordinate System	21
3.2.2	Tracker	21
3.2.3	Electromagnetic Calorimeter	22
3.2.4	Hadronic Calorimeter	23
3.2.5	Superconducting Magnet	24
3.2.6	Muon System	24
3.2.7	Triggering, Data Acquisition and Computing	27
4	Physical Objects	29
4.1	Muon	29
4.1.1	Muon Reconstruction	29
4.1.2	Muon Selection	31
4.1.3	Muon Trigger	32
4.2	Electron	32
4.2.1	Electron Reconstruction	32
4.2.2	Electron Trigger	33
5	Analysis	35
5.1	Recorded Data	35
5.2	Simulation	35
5.3	Scale Factors	35
5.4	Pileup	36
5.5	Analysis-Specific Selection	37
5.5.1	Muon Criteria	37
5.5.2	Electron Criteria	37
5.5.3	General Selection Criteria	39
5.6	Standard Model Backgrounds	40
5.6.1	Prompt Background	40
5.6.2	Misidentified Background	40
5.7	Signal Models	44
5.7.1	Signal Efficiency	44
5.7.2	Invariant Mass Resolution	45
5.8	Systematic Uncertainties	47
5.8.1	Standard Model Background Systematic Uncertainties	47
5.8.2	Systematic Uncertainties of Resonant-like Models	52

5.8.3	Systematic Uncertainties of QBH models	53
6	Results of Analysis in Electron-Muon Channel	55
6.1	Invariant Mass Distribution	55
7	Statistical Interpretation	61
7.1	Limit Setting	61
7.2	Exclusion Limits	63
7.2.1	RPV-SUSY Limits	64
7.2.2	SSM Z' Limits	66
7.2.3	QBH Limits	67
7.3	Influence of Systematic Uncertainties on Limit Setting	68
7.4	Comparison with other Searches for Lepton-Flavour-Violating Processes . . .	68
8	Summary and Conclusion	73
A	Appendix	75
A.1	Notation and Units	75
A.2	Narrow Width Approximation	75
A.3	Details of Trigger Strategy	76
A.4	Signal Samples	77
A.5	Standard Model Background Samples	81
A.6	Distributions of Lepton Kinematics	83
A.7	Investigations on Mass Resolution	86
A.8	Additional Signal Efficiency Plots	87
	Bibliography	89

1 Introduction

Since the beginning of modern physics at the end of the 19th century, physicists are driven by the challenge to find a fundamental theory to describe all known elementary particles and their interactions. During this period our picture of nature has changed along with the discovery of new particles. In 1897, J.J. Thomson measured the ratio of charge and mass of the electron. The antiparticle of the electron, called positron, as well as the muon were discovered using cosmic rays in the 1930s. The properties of the photon have been examined by looking at the photoeffect in 1905 and the Compton effect in 1922. The existence of neutrinos was postulated in 1930 by Pauli who studied the spectrum of the β -decay of a neutron. In 1956, for the first time an electron antineutrino was observed. In the 1960s, it has been proposed that the nucleons are made of partons. Two partons, namely the u- and d-quark were subsequently detected. As the energy rose in collider experiment, the heavier quarks were observed as well, ending with the top-quark in 1995 at the Tevatron. The massive gauge bosons were spotted the first time in 1983 at the proton-antiproton accelerator SPS at CERN. The particle most recently discovered is the Higgs boson in 2012 at the LHC. The best approach to describe all those known particles and their interactions until today is the standard model of particle physics. The standard model has passed many experimental precision tests since its finalization in the 1970s. However, there are theoretical aspects and experimental evidences suggesting that the description of the standard model is not complete. This search is part of the ongoing quest for physics beyond the standard model anticipating that the end of the road of discoveries is not yet reached.

The absence of flavour changing neutral currents in the standard model opens a search window for new physics. There are several extensions of the standard model that include such currents realized by heavy, neutral particles which are allowed to decay via a lepton-flavour-violating process into a pair of standard model particles. In this thesis, three different models are studied. The R-parity-violating supersymmetry model predicts a neutral tau sneutrino that can decay into an electron-muon pair. In the context of the sequential standard model an additional gauge boson called Z' is allowed to decay into $e\mu$. The third category of models that is studied consists of theories introducing extra dimensions. In these theories quantum black holes can be produced and decay into an electron-muon pair.

The Large Hadron Collider at CERN provides an excellent environment to perform a search for new physics in high energy collisions. Events of proton-proton collisions recorded by the CMS detector in 2015 at a centre-of-mass energy of 13 TeV are analysed. The amount of recorded data sums up to an integrated luminosity of 2.7 fb^{-1} . In this thesis events with a highly energetic electron-muon pair are selected.

This search for lepton-flavour-violating processes is complemented by numerous direct and indirect searches. At the LHC several direct searches have been performed. The ATLAS collaboration has looked into the electron-muon channel at a centre-of-mass energy of 7 TeV [1], 8 TeV [2] and 13 TeV [3]. This search with the CMS detector has a predecessor at 8 TeV [4]. Indirect searches also looking for lepton-flavour-violating processes have been performed for example by the SINDRUM [5], COMET [6] and DeeMe [7] collaborations.

This thesis is structured as follows. First, the theoretical basics of this analysis are presented beginning with the standard model. Processes predicted by the standard model constitute the background of this analysis. Theories extending the standard model, such as R-parity-violating supersymmetry, the sequential standard model and models introducing extra dimensions, are discussed in section 2. Section 3 introduces the experimental setup consisting of the circular collider LHC and the detector CMS. Afterwards, the electron and the muon and how they are reconstructed and identified are discussed in section 4. The details of the analysis are presented in section 5 which deals with the data and simulated sam-

ples in this analysis. The selection criteria are listed and the standard model backgrounds are discussed. The evaluation of the systematic uncertainties is also part of section 5. The results of the analysis are described in section 6. The statistical interpretation of the results, which consists of setting limits for the signal models, is the topic of section 7. Additionally, a comparison of this search with other direct searches at collider experiments as well as a comparison with indirect low-energy experiments is provided. Finally, section 8 gives a conclusion of this thesis. Conventions concerning notation and units that are used in this analysis are listed in section A.1.

2 Theory

This section is concerned with a brief introduction of the general concepts of quantum field theory. The topic of quantum field theory is more thoroughly discussed in reference [8]. One example of a quantum field theory which is of utmost importance for this analysis is the standard model of particle physics (SM). The fundamental principles of the standard model are discussed in section 2.1. The focus lies on topics that are directly connected to the analysis of this search. Furthermore, this section deals briefly with the question why there is no flavour-changing neutral current (FCNC) in the SM. This is followed by a discussion of theoretical problems within the standard model and the latest experimental evidence that is not compatible with the predictions of the standard model. This leads us to theories which extend the standard model of particle physics, often called beyond standard model (BSM) physics (section 2.2). Naturally, these theories intend to solve the apparent difficulties of the standard model. In sections 2.2.1, 2.2.2 and 2.2.3 we focus on the theoretical models that are studied in this analysis, namely R-parity-violating supersymmetry (RPV-SUSY), the sequential standard model (SSM) and extra dimensions. Those contents of this section that are more focused on theoretical issues are mostly based on references [9; 10]. References [11; 12; 13] provide the foundation of those parts of this section that are more directed towards experimental particle physics.

2.1 Standard Model of Particle Physics

The standard model of particle physics offers a unification of the theory of special relativity and quantum mechanics. Quantum field theories, like the standard model, tell us about quantum fields which are in the interpretation of particle physics the elementary particles of nature. The standard model describes the currently known elementary particles and their interactions except gravity. The particle content of the standard model is shown in figure 2.1. This content can be divided in two categories, matter particles and force carriers.

All the matter particles have spin $\frac{1}{2}$ ¹ and are therefore called fermions. The fundamental interactions, being the electromagnetic, weak and strong interactions, are mediated by force carriers which have spin 1 and are therefore called bosons. Additionally the Higgs boson enters the game, which has spin 0 according to today's knowledge.

The standard model is a so-called gauge theory. That means that there is a certain degree of freedom within the theory. This degree of freedom manifests itself in gauge symmetries. Gauge symmetries indicate that the theory is invariant under a certain set of local and continuous transformations. That implies that the physical predictions of the theory do not change if a gauge transformation is applied. This is called gauge invariance of the theory with respect to model-dependent gauge transformations. Gauge invariance is a fundamental requirement in gauge theories and a powerful tool to narrow down the theory to the processes that are consistent with gauge invariance. The gauge group² of the standard model is $SU(3) \times SU(2) \times U(1)$. These gauge symmetries are closely related to the force carriers of the standard model by group theoretical aspects. This is why the force carriers are often called gauge bosons.

The $SU(3)$ is the gauge group of quantum chromodynamics (QCD) or strong interaction. The gauge bosons of QCD are called gluons, which are massless. In total there are 8 gluons, which can be derived from group theory [10]. They couple only to particles carrying colour charge, i.e. to themselves and to only a subset of the matter particles, called quarks. Gluons do not interact with leptons since they are not colour-charged.

¹In this thesis natural units are used as discussed in section A.1.

²One can find the link between groups and symmetries in reference [15].

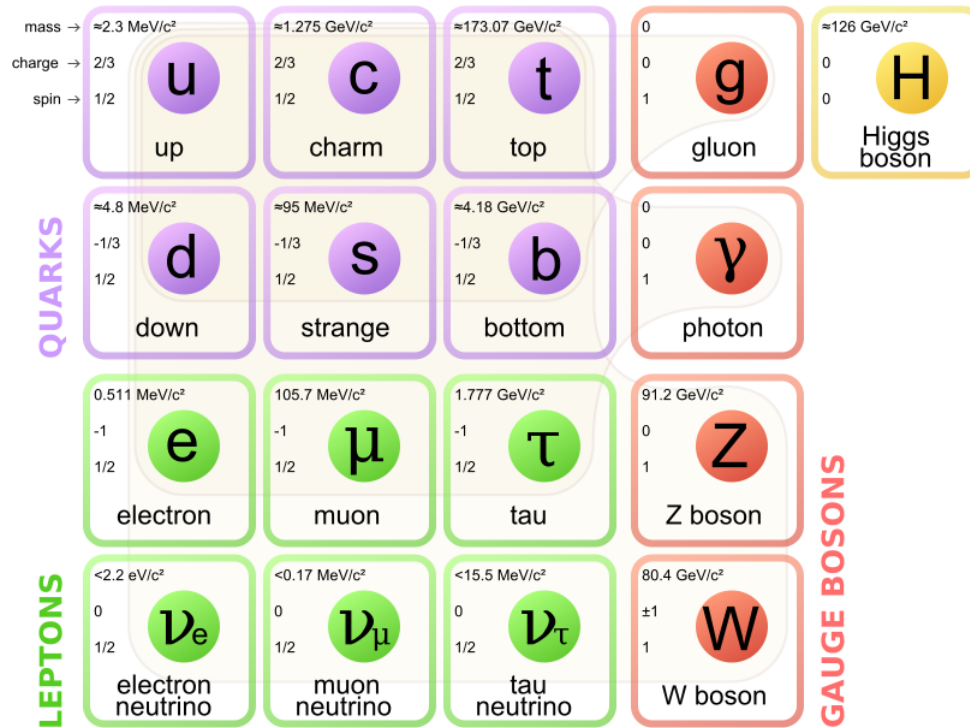


Figure 2.1: Particle content of the standard model showing the matter particles with spin $1/2$, called fermions, the gauge bosons with spin 1 and the Higgs boson with spin 0 . The fermions are divided into leptons and quarks. Properties such as mass, spin and charge of the standard model particles are listed. [14]

The $SU(2) \times U(1)$ forms the gauge group of the electroweak theory, which unifies the electromagnetic and weak force. The mediators of the electroweak force are the W^\pm and Z boson as well as the photon. The photon couples to all particles with electric charge, whereas the W and Z bosons couple to all fermions as well as to each other. The unification of electromagnetism and the weak sector goes back to the physicists Glashow, Weinberg and Salam [16; 17].

The particle that was experimentally discovered most recently is the Higgs boson [18]. This particle emerges from the theoretical idea of spontaneous symmetry breaking of the electroweak gauge group. This idea goes back to the physicists Brout, Englert and Higgs [19; 20]. Thanks to symmetry breaking it is - inside the standard model - theoretically allowed to give masses to fermions as well as to the W and Z bosons. The Higgs boson is the only particle with spin 0 in the standard model [21].

Other properties of the standard model, such as the renormalizability or the perturbative structure, are briefly discussed in the following.

A perturbative theory, in general, denotes the fact that one knows that a certain physical theory is easy to solve in a simplified version but the solution of the full theory is very hard to obtain. Now the assumption is that there is an expansion parameter α which defines a power series giving in the limit of infinite power in α the physics of the full theory. As long as the expansion parameter is small enough, this procedure works well. By calculating each term corresponding to a power in α theoreticians hope to decrease the difference with respect to the full theory. The terms corresponding to the growing number of orders in α is denoted as leading order (LO), next-to-leading order (NLO) and so on. Feynman graphs present a way to visualize the technique. Each power term is associated with a set of Feynman diagrams.

The complete theoretical prediction is then given by summing up all graphs according to the Feynman rules.

Renormalizability is a feature which tells us that the divergences appearing in our model can be handled. For example, if the perturbation series contains divergent integrals, these can be compensated by divergent bare quantities which are not measurable. This bare quantity is connected to the physical quantity. An example of this procedure is the Higgs mass which can be measured in an experiment. This measurable quantity is composed of an unphysical Higgs bare mass and quantum loop corrections (see section 2.2).

From a theoretical point of view perturbative structure and renormalizability of a model are often seen as a necessity to construct a meaningful and consistent theory of particle physics. This is why they are usually also imposed on theories extending the standard model. The enthusiastic reader can look into [8] to get some more insights.

In the context of quantum field theories the particle fields and their interactions can be expressed by the Lagrangian. The Lagrangian has to be gauge invariant, renormalizable and Lorentz-invariant. The gauge invariance is discussed above and mainly motivated by experimental evidence. Renormalizability is required due to the theoretical advantages discussed above. The Lorentz invariance is imposed because of Einstein's postulates of relativity. Given the Lagrangian, one can calculate for example processes like particle collisions. Those processes are studied intensively by the experiments at the LHC. Figure 2.2 presents high precision measurements of production cross sections of standard model processes. For comparison, the theoretical expectation is shown. It is remarkable, how good the agreement of the measurements with the theoretical expectation is over such a large range of 8 orders of magnitude in cross section. One gets a feeling why the standard model is supposed to be

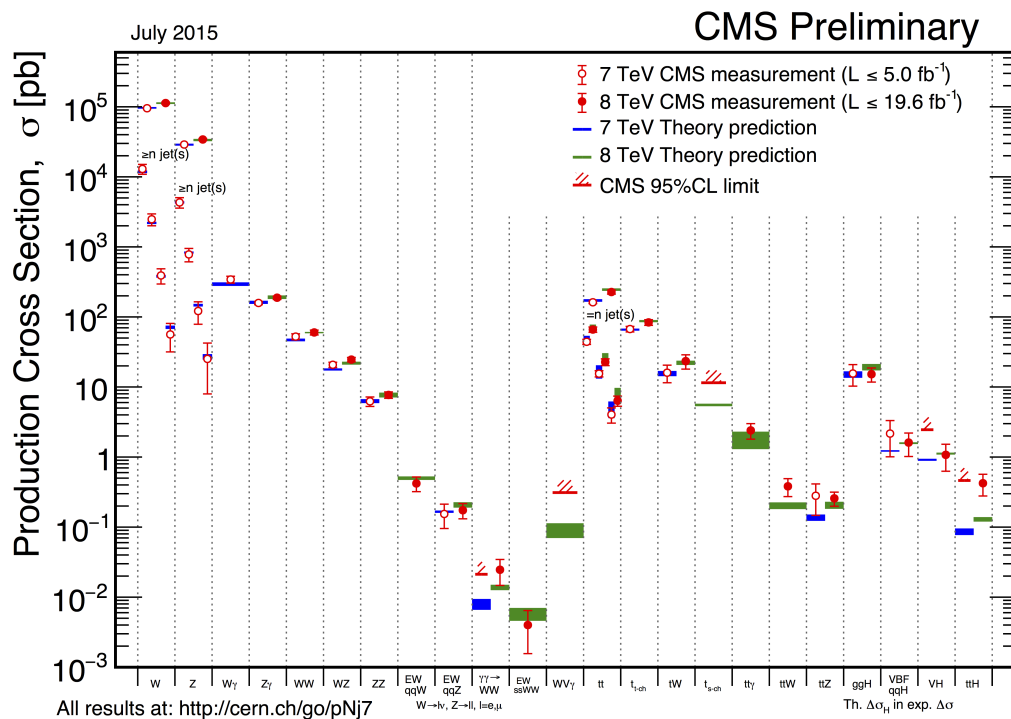


Figure 2.2: Comparison of CMS measurements studying standard model processes with their theoretical prediction. The horizontal axis shows many different processes covering electroweak processes from Diboson production to Higgs physics. The agreement of measurement and expectation over a range of 8 orders of magnitude in cross section is remarkable. [22]

the best-tested physical theory of all time.

For this analysis, one important aspect of the standard model is the electroweak sector since we are dealing with electrons and muons in the final state. It is also worth mentioning what kind of processes are forbidden in the electroweak sector. This analysis focuses on flavour violating processes and tries to answer the question why there is no FCNC in the standard model. In the environment of a hadron collider, such as the LHC, quantum chromo dynamics also deserves some considerations since the initial state consists of quarks and gluons. In order to dive into the formalism, the notation conventions have to be fixed. They are listed in section A.1.

2.1.1 Electroweak Theory

The electroweak theory is given by the Lagrangian

$$\mathcal{L}_{EW} = \underbrace{-\frac{1}{4}F_{\mu\nu}^a F^{a,\mu\nu} - \frac{1}{4}F_{\mu\nu}^1 F^{1,\mu\nu}}_{\mathcal{L}_G} + \underbrace{\bar{\Psi}i\not{D}\Psi}_{\mathcal{L}_F} - \underbrace{G_{ij}\bar{\Psi}_i\psi_j^d\Phi + \tilde{G}_{ij}\bar{\Psi}_i\psi_j^u\Phi + h.c.}_{\mathcal{L}_Y} + \underbrace{|D^\mu\Phi|^2 - V(\Phi)}_{\mathcal{L}_H}. \quad (2.1)$$

The gauge term \mathcal{L}_G represents the self-interactions of the gauge bosons (W^\pm , Z and γ). \mathcal{L}_F denotes the kinetic term, where the coupling of fermions to the gauge bosons as well as their kinematic term are contained. The fermions are denoted by the fields Ψ . The Yukawa term \mathcal{L}_Y gives the interaction of the fermions, leptons and quarks, with the Higgs boson. \mathcal{L}_H gives the Higgs term and its potential $V(\Phi)$, where Φ denotes the Higgs field. We have to dig a little bit deeper to be able to discuss peculiarities like FCNC. We start with the gauge term \mathcal{L}_G . First, we state what is meant by the field strength tensor $F_{\mu\nu}^{1/a}$

$$\begin{aligned} F_{\mu\nu}^1 &= \partial_\mu B_\nu - \partial_\nu B_\mu \\ F_{\mu\nu}^a &= \partial_\mu W_\nu^a - \partial_\nu W_\mu^a + g_2\epsilon^{abc}W_\mu^b W_\nu^c, \quad a = 2, 3, 4. \end{aligned} \quad (2.2)$$

The fields W^a and B denote the electroweak gauge fields and g_1 and g_2 are the corresponding gauge couplings. The fields of the photon, the W and Z bosons are linear combinations of these fields. In the Higgs term the abbreviation of the covariant derivative D_μ is defined by

$$D_\mu = \partial_\mu - ig_2 I^a W_\mu^a + ig_1 \frac{Y}{2} B_\mu, \quad (2.3)$$

where Y is the hypercharge and the I^a are the Pauli-matrices of the $SU(2)$ group³. The Higgs potential can be written as

$$V(\Phi) = -\mu^2\Phi^\dagger\Phi + \frac{\lambda}{4}\left(\Phi^\dagger\Phi\right)^2 \quad (2.4)$$

where the first term appears like a mass term for the Higgs and the second term gives a Higgs self-interaction. We impose $\mu^2, \lambda > 0$. In this case spontaneous symmetry breaking is possible since the vacuum expectation value (VEV) of this potential assumes the value $\langle\Phi\rangle = (0, v/\sqrt{2})^T$ and hence the VEV is non-zero⁴. The parameter v is the value where the Higgs potential is minimal. We require $\lambda > 0$ since then the vacuum is stable. Due to symmetry breaking three of the four electroweak gauge bosons acquire mass. We know that the massless gauge boson is the photon.

³These matrices are the generators of the $SU(2)$ group.

⁴That is a necessity for symmetry breaking. [10]

In the Yukawa sector, one finds a peculiarity of the electroweak theory written out in the Lagrangian. The fields Ψ and ψ both denote fermionic fields with the difference that Ψ is a left-handed doublet field and ψ represent a right-handed singlet field. The group acts differently on left- and right-handed fields. This is the chiral structure of the $SU(2)$ group. One can also find the fermionic mass terms in the Yukawa term which become obvious by expanding the Higgs field around its vacuum expectation value and looking at the constant term. The masses of the fermions can be predicted directly from the VEV of the Higgs field. There is another peculiarity in this procedure. The matrices G_{ij} and \tilde{G}_{ij} in \mathcal{L}_Y need to be diagonalized to obtain the fermionic mass terms. This diagonalization results in a rotation between the mass states and the interaction states of the fermionic fields. This rotation is represented by the Cabibbo-Kobayashi-Maskawa (CKM) matrix in the quark sector [23]. In the lepton sector, the same arguments apply and the so-called Pontecorvo-Maki-Nakagawa-Sakata (PMNS) matrix is obtained [24]. These matrices then appear in the kinematic term \mathcal{L}_F which results in the mixing of quarks and lepton flavours in the charged currents (W^\pm) of the electroweak sector. The strength of the mixing is given by the elements of the matrices. In the PMNS and CKM matrices diagonal elements are the biggest, i.e the mixing of flavours is existent but suppressed.

After discussing the charged current, we intend to discuss the neutral current sector of the electroweak theory with a few words. The only neutral current that is mediated by a massive particle in the standard model is realized by the Z boson. In contrast to the charged currents, there is no quark or lepton flavour mixing in the terms of the Z boson due to its diagonal structure with respect to the weak isospin [10]. We see that FCNCs are not included in the standard model. This statement is of utmost importance for this search since observing these processes would be a clear signature of physics beyond the standard model. Theories extending the standard model and allowing for FCNC are discussed in section 2.2.

2.1.2 Quantum Chromo Dynamics

The physics of quantum chromo dynamics is given by the Lagrangian

$$\mathcal{L}_{\text{QCD}} = \underbrace{-\frac{1}{4}F_{\mu\nu}^a F^{a,\mu\nu}}_{\mathcal{L}_G} + \underbrace{\bar{\Psi}i\not{D}\Psi}_{\mathcal{L}_M}, \quad (2.5)$$

where $a = 1, \dots, 8$ since the gauge symmetry of QCD is $SU(3)$. The gauge sector is constructed similar to the $SU(2)$ case. One striking difference is that we are dealing with 8 instead of 3 gauge bosons. One can write the field strength tensor as

$$F_{\mu\nu}^a = \partial_\mu A_\nu^a - \partial_\nu A_\mu^a + g_s f^{abc} A_\mu^b A_\nu^c, \quad (2.6)$$

where A^a represent the gluon fields, g_s denotes the strong gauge coupling and f^{abc} are the so-called structure constants of QCD. There are also self-interacting terms in the gauge sector like in the case of $SU(2)$. The matter part of the Lagrangian \mathcal{L}_M is dictated by the covariant derivative

$$D_\mu = \partial_\mu - ig_s A_\mu^a G^a, \quad (2.7)$$

where G^a denotes the 8 Gell-Mann matrices times $\frac{1}{2}$. In the matter sector of the QCD Lagrangian only fermions with colour charge are meant by writing Ψ .

There are two striking features of QCD to be mentioned in the context of a hadron collider search. Both of these features are due to the fact of the running coupling constant [25]

⁵. Figure 2.3 shows the running of the strong gauge coupling as a function of the momentum transfer Q .

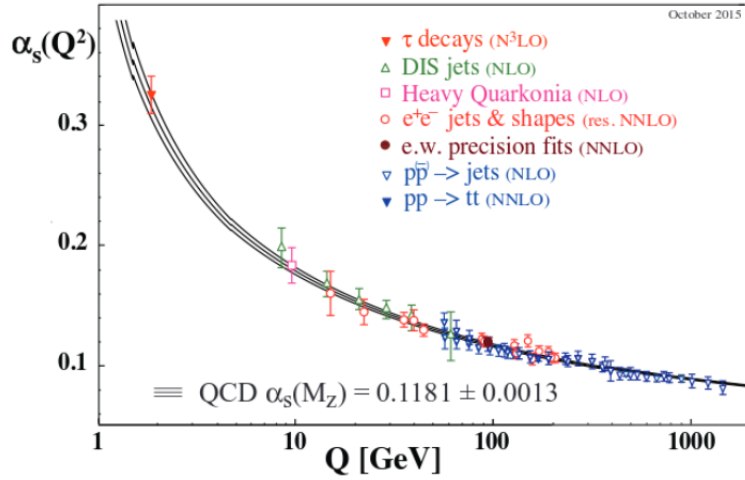


Figure 2.3: Running of the strong gauge coupling α_s as a function of the momentum transfer Q . Several measurements (different coloured symbols with error bars) are plotted along with the theoretical expectation (solid black lines) from the standard model. In the legend, where all measurements are listed, the respective order of QCD perturbation theory used in the extraction of α_s is indicated inside the brackets. The range of momentum transfer Q that is shown in this figure is well inside the perturbative regime of QCD. However, the tendency that the coupling is going up for low momentum transfers < 1 GeV can already be seen. [25]

In QCD, the running points out that the strong coupling is decreasing with increasing energy transfers in processes of QCD interactions. This fact allows to treat the QCD as a perturbative theory in the environment of the LHC. The other property is the so-called confinement. Confinement is a feature of QCD in the region of low energy transfers (large distances). For this energy regime the coupling increases leading to a rising attraction between colour-charged particles (quarks and gluons) that are moving away from each other⁶. This is why one cannot observe single quarks or gluons as free particles. Instead they form hadrons resulting from the energy stored in the strong field between them when moving apart. In collider physics this effect is called hadronization. A collimated bunch of hadrons is called jet, which is another term often used in the context of collider searches.

2.2 Beyond the Standard Model

Although the standard model of particle physics has been tested extensively in numerous high precision measurements for example at the LHC (see figure 2.2) and all those measurements found no deviation from standard model physics, there are nonetheless several topics apparent in particle physics which are not consistent with the standard model. These topics can be divided into two categories. One category consists of theoretical problems within the standard model. The other category contains latest experimental evidence that is not compatible with the standard model. In the following several examples of the two categories are briefly discussed.

In the standard model, the predicted Higgs mass m_h , that one would measure in an

⁵Also the coupling constants of the electroweak coupling are running but their running with respect to the energy transfer does not change the theoretical properties as much as in the QCD case.

⁶This is the opposite behaviour than in the case of the electric force.

experiment, is composed of two contribution, the so-called bare mass m_b and the quantum corrections to its mass by loop corrections δm_h . In an effective field theory approach, the loop corrections have been determined to be

$$(\delta m_h)^2 \propto G_F^2 [\Lambda_{UV}^2 + \dots]. \quad (2.8)$$

The G_F^2 denotes the coupling to the fermions and Λ_{UV} represents the fundamental scale of new physics. If the scale of new physics is the Planck scale of $\approx 10^{19}$ GeV, then the quantum corrections would be very large compared to the measured value of 125 GeV. This implies also a huge bare mass $m_b \gg m_h$. That such a fundamental variable of the standard model is the result of a difference of quantities that are 17 orders of magnitude away is supposed to be unnatural. This problem is often referred to as the hierarchy or fine-tuning problem of the Higgs mass [26].

Another theoretical issue is that gravity is not included into the standard model. Gravity is described with high precision by general relativity. Unfortunately, theoreticians did not succeed so far in unifying the concepts of general relativity and quantum field theory. Quantum effects of gravity play an important role at the Planck scale which corresponds to the Planck mass of $M_{\text{Pl}} = 1.22 \cdot 10^{19}$ GeV. So we know that there has to be physics beyond the standard model between the electroweak scale (\sim TeV) where the standard model without gravity works quite well and the Planck scale.

There exists some experimental evidence by astrophysical observations that a type of matter exists that we cannot describe properly with standard model physics. This type of matter is called dark matter. In the following a list of some of the observations hinting towards dark matter are given. A more complete list can be found in reference [27].

- Using precision measurements of the Cosmic Microwave Background (CMB) and nucleosynthesis it is possible to determine the matter content of the universe to be $30.8 \pm 1.2\%$ ⁷. The baryon density is measured to be $\approx 5\%$ which leaves $\approx 26\%$ for the dark matter content. [28]
- The observation of the cluster merger 1E0657558 yields strong evidence of dark matter [29]. This cluster merger is measured using X-ray detection and simultaneously using gravitational lensing. With the X-ray detection the distribution of ordinary matter can be determined. Gravitational lensing allows to detect the distribution of all kinds of matter interacting via gravity in the cluster merger. These two detection methods result in matter distributions that differ significantly. This difference cannot be explained by a modification of the gravitational force. However, this observation could be explained by introducing a new type of matter not yet included in the standard model, called dark matter. A picture illustrating the measurement can be seen in figure 2.4.
- The concept of a weakly interacting massive particle (WIMP) plays an important role in dark matter searches. The concept proposes a massive elementary particle χ that is stable, has no electric charge and yet undiscovered. These χ 's are supposed to be in thermal equilibrium in the early universe, meaning that the back-and-forth processes like $\chi\bar{\chi} \leftrightarrow f\bar{f}$ are keeping the particles in equilibrium with the SM particles denoted by f . As time goes on after the Big Bang, the universe expands and the temperature drops. This causes the particles to be less energetic and consequently the direction of $\chi\bar{\chi} \rightarrow f\bar{f}$ is kinetically disfavoured due to the expected high mass of the χ 's ($m_\chi \geq 100$ GeV)⁸.

⁷This is expressed with respect to the total energy density of the universe ρ_{crit} . This total energy density is very close to the critical energy density, which causes the universe to be flat.

⁸The assumption that the dark matter candidate has a mass of ≥ 100 GeV is substantiated by exclusion limits from collider searches. [30]

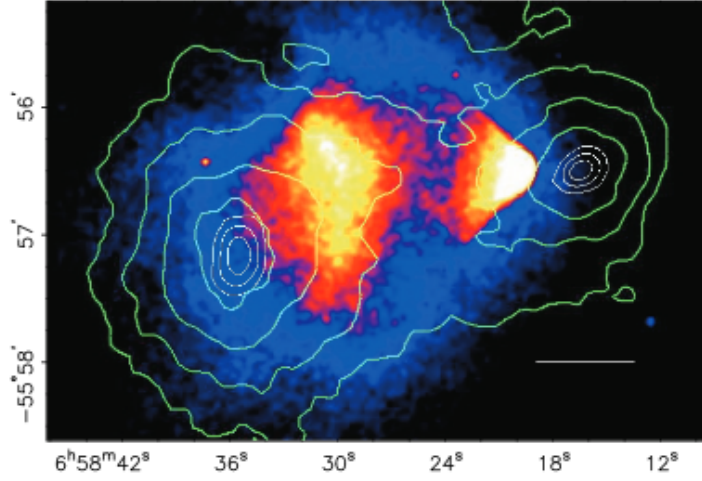


Figure 2.4: The coloured image shows the X-ray detection of the cluster merger 1E0657558. Shown in green contours are results of measuring the same cluster merger using gravitational lensing. A significant difference between the two methods can be seen which hints towards the existence of dark matter. [29]

The χ 's decouple from the standard model particles and the amount of χ 's stays more or less constant. This is called freeze-out. The remaining cosmological abundance can be approximated by

$$\Omega_{\chi} = \frac{10^{-37} \text{ cm}^2 \cdot c}{\langle v \cdot \sigma_{\chi\bar{\chi} \rightarrow f\bar{f}} \rangle_{\text{freeze}}}, \quad (2.9)$$

where $\sigma_{\chi\bar{\chi} \rightarrow f\bar{f}}$ is the annihilation cross section, c denotes the speed of light and v the velocity of the χ 's. The denominator is taken as an average at the time of the freeze-out. If one assumes the velocity of the χ 's to be $v \approx \frac{1}{3}c$ ⁹ and inserting the abundance of dark matter in the universe Ω_{χ} , one finds

$$\sigma_{\chi\bar{\chi} \rightarrow f\bar{f}} \approx 10^{-36} \text{ cm}^2 = 1 \text{ pbarn}. \quad (2.10)$$

This order of magnitude is typical for processes of the weak interaction of the standard model. This is the reason why this concept is called WIMP miracle. A thorough calculation of the approximations above can be found in reference [31].

Another piece of evidence for physics beyond the standard model is that the universe is full of matter but there is almost no antimatter (matter-antimatter asymmetry). By first principles, matter and antimatter should have been created equally during the Big Bang. However, one can construct theories that treat matter different than antimatter. Actually the standard model of particle physics is one of them. The difference is induced by CP violation. However, the amount of CP violation in the standard model is not sufficient to describe the matter-antimatter asymmetry properly. This is why an extension of the standard model is expected to have more CP-violating terms.

With the list of evidences for physics beyond the standard model, the focus moves towards the different BSM theories that are studied in this search. R-parity violating supersymmetry, the sequential standard model and extra dimensions are introduced and discussed.

⁹This estimate is based on freeze-out calculation of heavy particles. [31]

2.2.1 R-Parity-Violating Supersymmetry

One of the models which are studied is a supersymmetric extension of the standard model which allows R-parity violating processes (RPV-SUSY). Before we discuss what R-parity stands for, a brief introduction into supersymmetric extensions of the standard model and their motivation is given.

Supersymmetry (SUSY) is among the most promising theories to solve for example the hierarchy/fine-tuning problem as well as to provide a dark matter candidate. A ground-laying version of a supersymmetric model is the so-called minimal supersymmetric extension of the standard model (MSSM). It is minimal in the sense that if you construct a supersymmetric model as an extension of the standard model the particle content in the MSSM is minimal [32]. In MSSM each particle of the standard model has a corresponding superpartner, whose spin differs by half a unit compared to the SM partner. Every fermion gets a bosonic superpartner and every boson gets a fermionic superpartner. The SM particles and their superpartners are merged into so-called superfields. Table 2.1 shows a list of the superfields.

These SUSY models introduce a new symmetry. If this symmetry were an exact symmetry of nature, then SM particles and their superpartners would be degenerate in mass. However, until today no superpartner has been observed by experiments. Thus, supersymmetry is expected to be broken and subsequently to be reduced to the SM gauge symmetries at the electroweak scale.

The most generic and renormalizable Lagrangian in supersymmetric extensions includes terms that violate both baryon and lepton number. Since these terms are strongly constrained by experiment, in many SUSY models an additional symmetry is introduced, called R-parity, in order to remove those terms from the Lagrangian. R-parity manifests itself by assigning a multiplicative quantum number to each particle. Standard model particles have an even R-parity whereas the superpartners have odd R-parity. There are two important phenomenological consequences due to R-parity conservation. Supersymmetric particles can only be produced in pairs and the lightest supersymmetric particle cannot decay into

Superfields	representation ($SU(3), SU(2)$)	SM content
Q	(3,2)	$\begin{pmatrix} u \\ d \end{pmatrix}_L$
U^c	$(\bar{3},1)$	\bar{u}_R
D^c	$(\bar{3},1)$	\bar{d}_R
L	(1,2)	$\begin{pmatrix} \nu_l \\ l \end{pmatrix}_L$
E^c	(1,1)	\bar{l}_R
H_u	(1,2)	Higgs doublet
H_d	(1,2)	Higgs doublet

Table 2.1: List of superfields which is a compactified notation for both the SM particles and their superpartners. In the middle column, one can see which superfield belongs to which representation of the corresponding gauge symmetry of the standard model. In the right column, one can read off the SM content of each superfield.

standard model particles and is therefore a candidate for dark matter. Another problem that would arise due to the baryon-number-violating terms consists of the prediction that the proton can decay which is in strong contrast to experimental results [33]. This is also solved by introducing R-parity conservation.

Despite all those facts, this analysis is concerned with R-parity violating SUSY models. After this long plea for R-parity conservation, the motivation for a RPV-SUSY search deserves some explanation. As a first step we have a look at the structure of the RPV terms in the superpotential :

$$\mathcal{W}_{RPV} = \underbrace{\frac{1}{2}\lambda_{ijk}L_iL_jE_k^c + \lambda'_{ijk}L_iQ_jD_k^c}_{\mathcal{W}_\lambda + \mathcal{W}_{\lambda'}} + \underbrace{\frac{1}{2}\lambda''_{ijk}U_i^cD_j^cD_k^c}_{\mathcal{W}_{\lambda''}} + \mu_i H_u L_i. \quad (2.11)$$

The capital letters represent the superfields containing both standard model particles and their superpartners (which differ in spin). The indices i, j, k denote the fermion generation. The L_i denotes the superfields of the left-handed leptons and the E_i^c correspond to the superfields of the right-handed leptons. Q_i denotes the superfields of the left-handed quarks and the U_i^c, D_i^c denote the superfields of the right-handed up-type and down-type quarks, respectively. The last term containing the Higgs superfield H_u is neglected in the following since one can eliminate this term by rotating the Higgs field [34]. Details of how to construct the corresponding Lagrangian out of the terms in the RPV superpotential as well as the notation conventions of the superfields are given in reference [34].

The term $\mathcal{W}_{\lambda''}$ leads to baryon number violation. In order to account for the fact that there are tight constraints on the lower limit of the lifetime of the proton [33] it is better to remove the baryon-number-violating terms. This is accomplished by introducing an additional symmetry. In this analysis, the so-called Baryon Triality is introduced as an additional discrete symmetry [35]. Thanks to Baryon Triality the baryon-number-violating terms disappear and this stabilizes the proton. This is how the problem is solved from a theoretical point of view. However, if one focuses on the couplings that are allowing the proton to decay, one ends up with the couplings λ''_{11k} with $k = 1, 2, 3$. Consequently, introducing the additional symmetry called Baryon Triality yields stronger constraints than demanding the stability of the proton.

The terms \mathcal{W}_λ and $\mathcal{W}_{\lambda'}$ are responsible for lepton flavour violation. These terms are of course not excluded from the model since these predict exactly the processes we are looking for. The fundamental requirement of gauge invariance helps us to constrain some parameters. From gauge invariance one can conclude that $\lambda_{ijk} = -\lambda_{jik}$, giving antisymmetry in their first two indices.

In the following we discuss the model in the context of a hadron collider search like the LHC. One can extract a few more aspects from the Lagrangian in equation (2.11) showing that a collider search is possible. The single production of a supersymmetric particle is possible for example in a resonance. The coupling λ' allows for a production of a slepton via quark-antiquark fusion in the proton-proton collisions of the LHC. The coupling λ allows the decay of the slepton into a lepton-flavour-violating final state. Since there are many parameters in this model one has to simplify the model to be able to perform a search. In the following a list of assumptions is given that reduces the number of parameters in the search to a minimum of 3.

- The first assumption to simplify the model deals with the tau sneutrino $\tilde{\nu}_\tau$. In this simplification it is the lightest supersymmetric particle (LSP) and can be resonantly produced. If it is the LSP, only decays into standard model particles are allowed ¹⁰.

¹⁰Since decays into standard model particles are not forbidden in the RPV-SUSY, the LSP is unfortunately not a good candidate for dark matter anymore.

- The coupling λ'_{311} allows for tau sneutrino production via $d\bar{d}$ annihilation¹¹. Here the first generation is chosen since this generation provides the largest production cross section at a proton-proton collider due to the parton distribution function (PDF) of the proton [36]. The coupling λ_{132} gives the decay to the lepton flavour violating final state of an electron-muon pair. We assume $\lambda_{132} = \lambda_{231}$ so that the decay parameters are independent of how the products are charged.
- The remaining couplings in the RPV Lagrangian in equation (2.11) are set to zero. The only relevant supersymmetric particle for this model is the tau sneutrino.

These assumptions leave us with the process of a tau sneutrino $\tilde{\nu}_\tau$ produced via $d\bar{d}$ fusion and decaying into an electron-muon pair. One should keep in mind that also the decay into a $d\bar{d}$ pair is possible but this is not the signature we are looking for in our detector. The corresponding Feynman diagram is shown in figure 2.5.

In this search, this process determines the signal process of the RPV-SUSY model. The parameter of the search are the tau sneutrino mass $M_{\tilde{\nu}_\tau}$ and the coupling parameters of the production λ'_{311} and the decay into an electron-muon pair $\lambda_{231} = \lambda_{132}$. In the calculation of the cross section of this process the narrow width approximation (NWA) is used. More information about the conditions under which the NWA is valid and the implications of the NWA on the calculation are summarized in section A.2. In the NWA the cross section times branching ratio assumes the form

$$\sigma \cdot \text{BR}(\tilde{\nu}_\tau \rightarrow e^\pm \mu^\mp) \sim (\lambda'_{311})^2 \frac{\Gamma_{\tilde{\nu}_\tau}^{e\mu}}{\Gamma_{\tilde{\nu}_\tau}^{\text{tot}}} \sim \frac{(\lambda'_{311})^2 \left((\lambda_{132})^2 + (\lambda_{231})^2 \right)}{3 (\lambda'_{311})^2 + \left((\lambda_{132})^2 + (\lambda_{231})^2 \right)} \quad (2.12)$$

as a function of the coupling parameters. $\Gamma_{\tilde{\nu}_\tau}^{e\mu}$ and $\Gamma_{\tilde{\nu}_\tau}^{\text{tot}}$ denote the partial width of the tau sneutrino into an electron-muon pair and the total width, respectively. We discuss some limit cases of this cross section formula. For $\lambda'_{311} \gg \lambda_{132}$, the cross section times branching ratio is not dependent on λ'_{311} anymore. Increasing λ'_{311} does not result in an increasing sensitivity. For a very small coupling λ_{132} , the tau sneutrino becomes a long-lived particle.

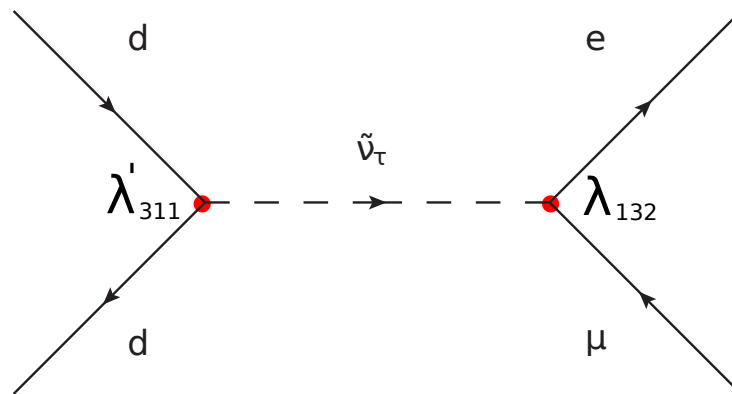


Figure 2.5: Feynman graph presenting $\tilde{\nu}_\tau$ production via $d\bar{d}$ fusion and decaying into an electron-antimuon pair. In Feynman notation the solid and dashed lines denote fermions and bosons, respectively. Each vertex is accompanied by a coupling, here λ'_{311} and λ_{132} . These go into the matrix element calculation leading to the cross section of the process.

¹¹A production of a tau sneutrino by up-type quark annihilation is forbidden because of SU(2) invariance of the $\mathcal{W}_{\lambda'}$ term.

This would result in a signature of displaced vertices, i.e. the tau sneutrino travels a distance through the detector and decays then into an electron-muon pair. This search cannot study this part of the parameter space. For $\lambda'_{311} \ll \lambda_{132}$, equation (2.12) becomes independent of the λ_{132} coupling, which means that the branching fraction for an $e\mu$ decay of the tau sneutrino is $\sim 100\%$. The sensitivity of the search only scales with the production cross section driven by λ'_{311} .

The total width of the tau sneutrino can be written as

$$\frac{\Gamma_{\tilde{\nu}_\tau}}{M_{\tilde{\nu}_\tau}} = \frac{1}{16\pi} \cdot (3(\lambda'_{311})^2 + 2(\lambda_{132})^2). \quad (2.13)$$

The numerical factor in equation (2.13) is coming from phase space calculations. We consider the RPV-SUSY model in a parameter space of λ_{132} , λ'_{311} and $M_{\tilde{\nu}_\tau}$ where both couplings are smaller than 0.1. Thus, comparing the relative width with the invariant mass resolution given by the CMS detector, leads to

$$\frac{\Gamma_{\tilde{\nu}_\tau}}{M_{\tilde{\nu}_\tau}} \ll \frac{\sigma_{M_{e\mu}}}{M_{e\mu}}. \quad (2.14)$$

Typical values of the invariant mass resolution of an electron-muon pair are 2 – 6 % (figure 5.7). If equation (2.14) holds then the search can be declared to be a search for a resonance. This has several implications on the statistical interpretation of the results and especially in the limit setting procedure in section 7.2.1.

The formulae (2.12) and (2.13) are given at leading order of perturbation theory. In order to account for next-to-leading order (NLO) QCD effects a k-factor for the production cross section is introduced. The correction is based on a program provided by the authors of [37]. In figure 2.6 the k-factor is presented as a function of the tau sneutrino mass $M_{\tilde{\nu}_\tau}$.

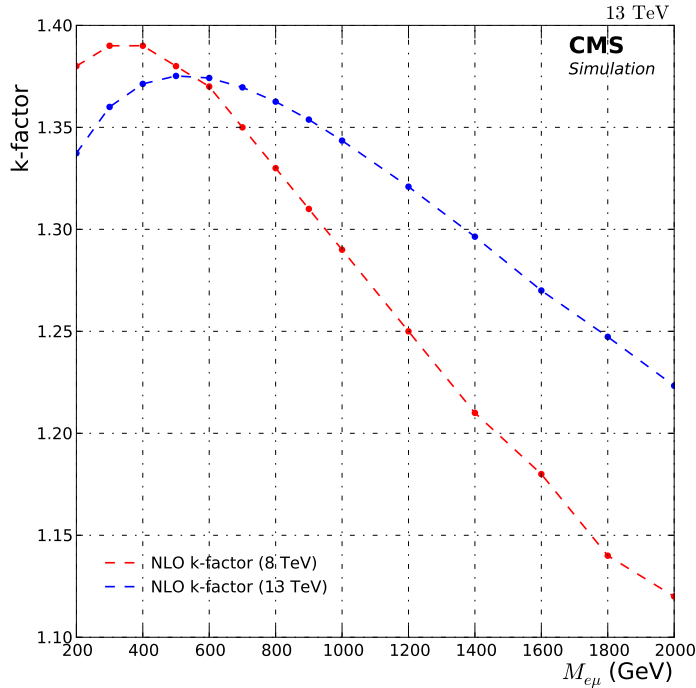


Figure 2.6: The applied k-factor in the RPV-SUSY model as a function of $M_{\tilde{\nu}_\tau}$ is shown on the right vertical axis. Additionally a comparison with the k-factor at $\sqrt{s} = 8$ TeV is presented. The k-factor is calculated by using a program which is provided by the authors of [37].

A typical shape of the invariant mass spectrum of a signal model simulated for the CMS detector coming from the tau sneutrino process is presented in figure 2.7.

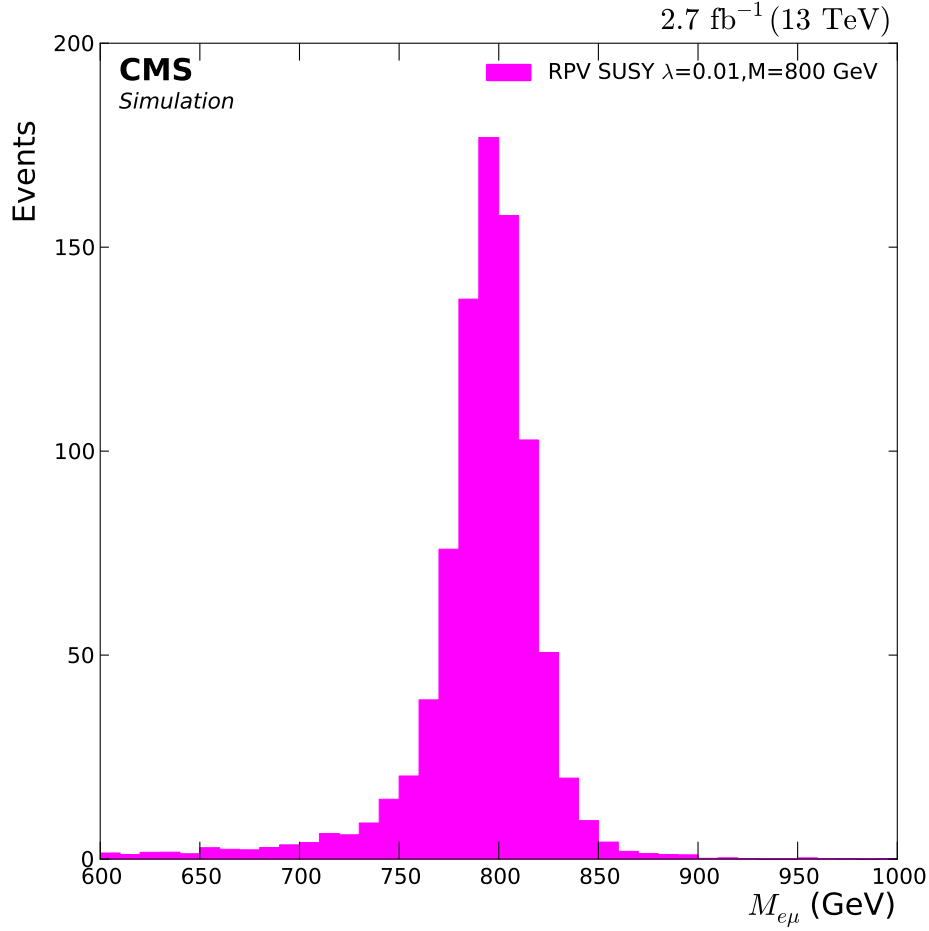


Figure 2.7: Signal shape of a tau sneutrino in RPV-SUSY with a mass of $M_{\tilde{\nu}_\tau} = 1$ TeV and couplings of $\lambda_{132} = \lambda'_{311} = 0.01$ leading to $\sigma \times \text{BR} \sim 5$ fb at leading order. This is presented as a function of the invariant $e\mu$ mass $M_{e\mu}$ after full reconstruction (see section 5).

2.2.2 Sequential Standard Model Z'

The Sequential Standard Model (SSM) extends the Standard Model by introducing an additional $U(1)$ gauge symmetry. This new symmetry is naturally accompanied by an additional neutral gauge boson called Z' . The SSM is a rather simple extension of the SM, which is why it is suitable to use as a benchmark model in a search for lepton-flavour-violating decays. A more detailed description of the SSM can be found in [38]. We assume that the Z' has the same couplings to the quarks as the SM Z boson of the electroweak force. In addition, the model allows us to write

$$\mathcal{L}_{Z' \rightarrow l_i l_j} = \frac{g_{EW}}{2 \cos \theta_W} \kappa_{ij} Z'_\mu \left[\frac{1}{2} \bar{l}_i \gamma^\mu \gamma_5 l_j - \left(\frac{1}{2} - 2 \sin^2 \theta_W \right) \bar{l}_i \gamma^\mu l_j \right].$$

l_i, l_j denote the lepton fields, the indices i, j represent the fermion generation and Z'_μ denotes the Z' vector field, the constants g_{EW} and θ_W are the electroweak coupling constant and the Weinberg angle, respectively. The Lagrangian has the same structure as the couplings of the Z to the SM leptons. The only difference is the coupling constant κ_{ij} , which

allows for lepton flavour violation. We impose a single dominant assumption, i.e. $\kappa_{12} = 1$, all other $\kappa_{ij} = 0$. In other words, we only consider the LFV decay $Z' \rightarrow e\mu$. This is the only decay mode considered in this search.

The Z' couples to the quarks like the standard model Z boson. Thus, a search for the production of the Z' can be performed with CMS data. The most probable initial states are given by the fusion of a light quark-antiquark pair, like $u\bar{u}$ or $d\bar{d}$. This is different than in the RPV-SUSY search where only down-type quarks are allowed in the initial state. For simplicity, interference between the SM Z boson and the Z' is not included in this model.

This search is similar to the search for a tau sneutrino in the RPV-SUSY case since it is also a resonance search. We have to check if equation (2.14) holds. For this, we take a look at the total width $\Gamma_{Z'}$. We consider the branching ratio into the electron-muon pair to be $\text{BR}(Z' \rightarrow e\mu) = 10\%$ staying constant over the studied mass range. With this assumption and the input that all other branching ratios are the same as for the standard model Z , the LFV decay basically replaces the branching ratios of $Z \rightarrow l\bar{l}$. For the mass region of this search ($500 \text{ GeV} < M_{Z'} < 5 \text{ TeV}$) we can write $\frac{\Gamma_{Z'}}{M_{Z'}} < 0.01$ and that is below the invariant mass resolution (see figure 5.7).

In this model, there is a single parameter, namely the mass of the Z' , $M_{Z'}$, which is varied for the different samples.

2.2.3 Quantum Black Holes

In section 2.2 we argued that the energy scale corresponding to the Planck mass should yield new physics. However, the Planck mass of $M_{\text{Pl}} = 1.22 \cdot 10^{19} \text{ GeV}$ is clearly out of the testable range of present and future collider searches. Fortunately, there are BSM theories on the market that effectively lower the Planck scale to the TeV range, which would make a collider search at the Planck scale possible. Models introducing extra dimensions belong to that category. There is a variety of extra-dimension models with different types and numbers of extra dimensions. For this analysis the topology of the extra dimensions and its connection to the $3 + 1$ space-time dimensions is not of utmost importance. One can find theoretical details of the models in references [39; 40].

The fact that these models allow for the production of microscopic black holes¹² in high energy particle collisions is however of utmost importance for this search. In extra dimensions the threshold masses for a production of microscopic black holes are expected to be at the reduced Planck mass $M_D \sim \text{TeV}$, where quantum gravity effects begin to play a role. For the region where the energy scale of physics Q is much greater than the reduced Planck mass $Q \gg M_D$ a semiclassical description of gravity is sufficient. In this region ($Q \sim 5 - 20 \text{ TeV}$) semiclassical black holes are produced. Since they are thermal objects, their decay is described by Hawking radiation¹³. However, with a production threshold of $5 - 20 \text{ TeV}$ it is either very unlikely or totally impossible that semiclassical black holes can be observed at the LHC ($\sqrt{s} = 13 \text{ TeV}$). Fortunately, there is the region close to the reduced Planck mass, $Q \sim M_D$. In this region, non-thermal quantum black holes (QBHs) can be produced. In contrast to the semiclassical black holes, QBHs are expected to decay into a pair of standard model particles. Among the different decays, there is the compelling possibility to decay into a LFV final state like an electron-muon pair. Since we assume the QBHs to have spin-0, be colourless and neutral, the most important initial states in a proton-proton collider are quark-antiquark pair ($q\bar{q}$) and two gluons (gg). This is why the QBH is our candidate in the context of extra-dimension models that is to be observed at the LHC [41; 42].

¹²Microscopic denotes the difference to their astrophysical brothers, also called black holes.

¹³Hawking radiation predicts a democratically decay into all standard model particles.

In the following, we want to have a look at the cross section of a process involving a production of a QBH at a proton-proton collider like the LHC. First, there is the question whether the mass spectrum of the QBHs is discrete or continuous. In this search the spectrum is assumed to be continuous.¹⁴ The production cross section can be written as

$$\sigma_{\text{QBH}}^{pp}(s, M_{\text{QBH}}, n, M_D) = \pi r_s^2(M_{\text{QBH}}^2, n, M_D) \int_0^1 2z dz \int_{\frac{(M_{\text{QBH}})^2}{y(z)^2 s}}^1 du \int_u^1 \frac{dv}{v} \times F(n) \sum_{i,j} f_i(v, Q) f_j(u/v, Q). \quad (2.15)$$

Here, s is the centre-of-mass energy squared, n the number of extra dimension in the model, M_{QBH} denotes the threshold for a QBH production and M_D represents the reduced Planck mass. QBHs can be described as heavy particles with a very short lifetime. Using dimensional analysis one obtains $\Gamma(\text{QBH} \rightarrow 2 \text{ particles}) \sim \frac{1}{64\pi^2} M_{\text{QBH}}$ for the total width [42]. In equation (2.15), one assumes that the cross section can be extrapolated from the cross section of semiclassical black holes meaning the geometrical cross section πr_s^2 with the Schwarzschild radius given in n -dimensions by

$$r_s(M_{\text{QBH}}^2, n, M_D) = k(n) M_D^{-1} [M_{\text{QBH}}/M_D]^{1/(1+n)} \quad (2.16)$$

with

$$k(n) = \left[2^n \sqrt{\pi}^{n-3} \frac{\Gamma((3+n)/2)}{2+n} \right]^{1/(1+n)}. \quad (2.17)$$

The parameter z in equation (2.15) denotes the rescaled impact parameter, $F(n)$ and $y(z)$ are calculated in the framework of classical black holes and not for the non-thermal QBHs. Thus they are set to $F(n) = y(z) = 1$. The labels i, j run over the different particle species, f_i, f_j are parton distribution functions evaluated at the scale of momentum transfer Q , u and v are the momentum fractions of the incoming particles. The respective form factor for the case of n dimensions which should be introduced for the parton-level cross section to reproduce the correct cross section from the Lagrangian with contact interactions is

$$FF = (4\pi k(n))^2 \left(\frac{M_{\text{QBH}}}{\sqrt{\hat{s}}} \right)^{\frac{2n}{1+n}} \Theta(\sqrt{s} - M_{\text{QBH}}). \quad (2.18)$$

Here, the Θ function is a step function. This yields the characteristic shape of the turn-on of the signal shape at the threshold mass M_{QBH} followed by a plateau. In figure 2.8, an example of a QBH signal spectrum is shown with a threshold mass of 1 TeV and $n = 1$. The turn-on at the threshold mass is smeared out and the plateau is replaced by a decreasing tail due to the PDFs of the proton.

The parameter for the QBH search are the number of extra dimensions n and the threshold mass for QBH production $M_{\text{QBH}} \equiv M_{th}$. In this search, two different models of extra dimensions are studied. For $n = 1$, the Randall-Sundrum (RS) model is used [39]. The RS models consist of a single warped extra dimension. Gravity is localized on a so-called brane and the SM particles are confined to another brane. This denotes the fact that these particles cannot propagate in the extra dimensions. In contrast, in the ADD models, gravity is allowed to propagate in the extra dimensions and is not localized on a brane. The SM particles are still confined to a brane within the extra dimensions. The ADD models have several large¹⁵ compactified extra dimensions. For $n = 4, 5, 6$, ADD models are studied [40].

¹⁴However, this topic is a question under debate for QBHs. For example in reference [43], one finds an argumentation for discrete mass spectrum.

¹⁵Extra dimensions are called 'large' in comparison to the weak energy scale.

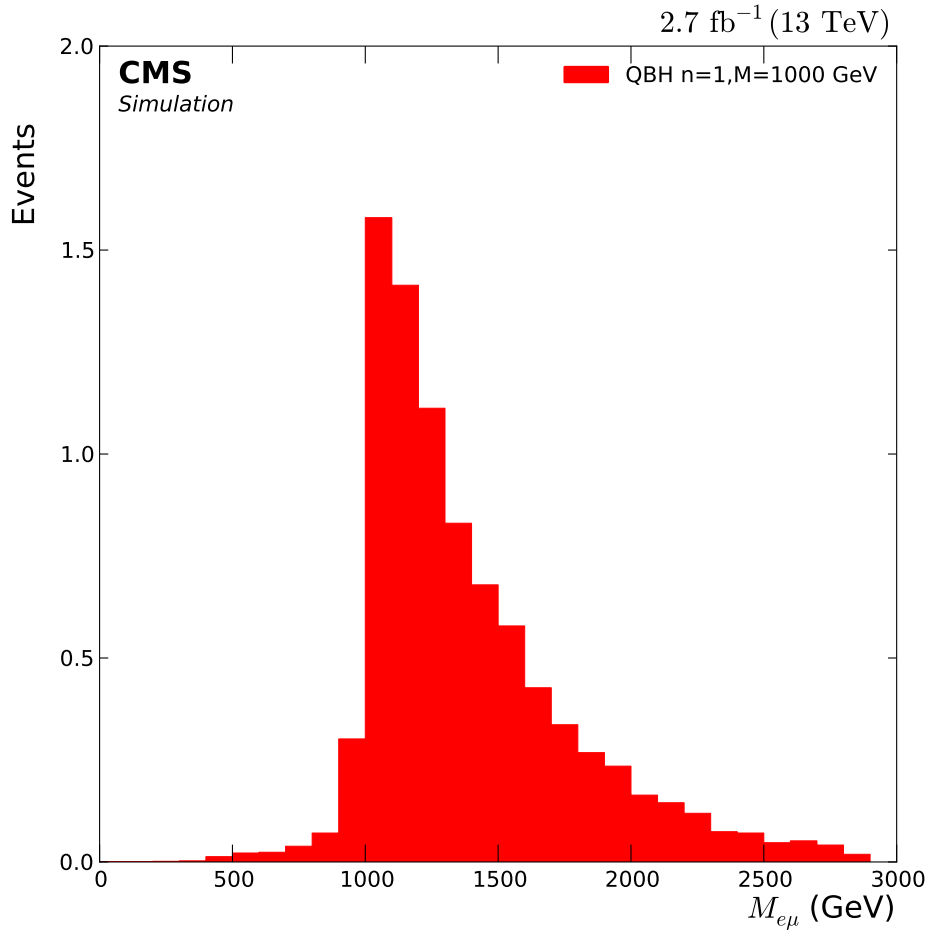


Figure 2.8: Signal shape of a QBH with $M_{\text{th}} = 1$ TeV and $n = 1$. This is presented as a function of the invariant $e\mu$ mass $M_{e\mu}$ after full reconstruction (see section 5). The plateau of the step function, which is expected from the form factor, is smeared out due to the influence of the PDFs of the proton.

3 Experimental Setup

This chapter is devoted to introduce and explain the accelerator LHC and the detector CMS. First, a brief description of the LHC is given. Then the CMS detector with its subdetectors is discussed.

3.1 General Information about the Large Hadron Collider

The Large Hadron Collider (LHC) is a circular particle accelerator and is installed underground near Geneva at the European Centre For Nuclear Research (CERN). The LHC has a circumference of 27 km. A detailed description of the LHC can be found in reference [44].

In this analysis proton-proton collisions are analysed. Before the protons enter the LHC there are different steps to go through. By ionizing hydrogen protons are produced. Afterwards they are accelerated in bunches by a linear accelerator (LINAC2) and three ring accelerators (BOOSTER, PS, SPS). Inside the LHC, the protons are again accelerated to reach the total energy of 6.5 TeV. Figure 3.1 shows the full acceleration chain of the LHC. The LHC has four collision points surrounded by complex detectors, namely ALICE, LHCb, ATLAS

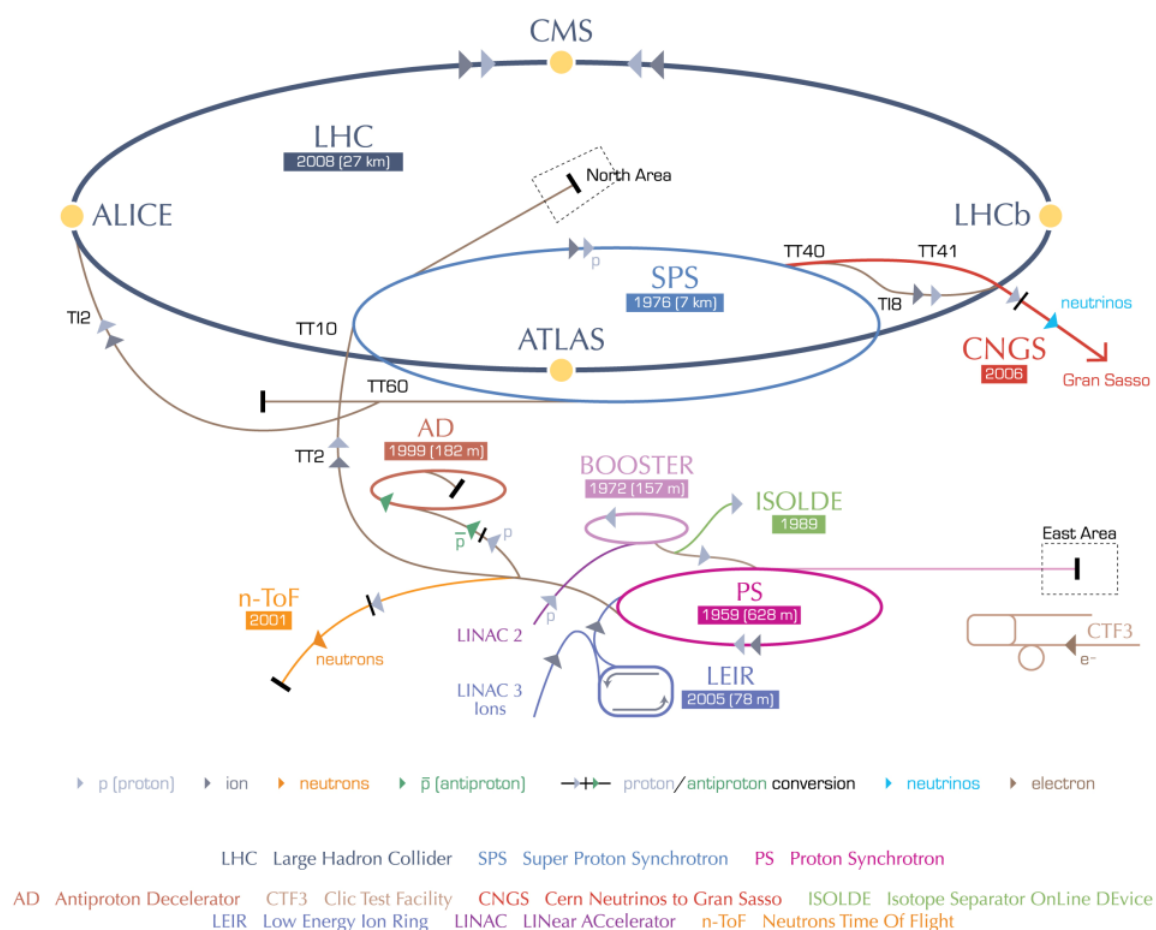


Figure 3.1: Accelerator complex at CERN: For each accelerator its year of construction is given and in the circular case its circumference. Additionally one can see which particle is accelerated in which part of the chain. For this analysis, only the proton line is relevant. [45]

and CMS. The dataset used in this analysis stems from the Compact Muon Solenoid (CMS) detector and is recorded in the year 2015. The amount of data for this analysis provided by the LHC in 2015 sums up to an integrated luminosity of 2.7 fb^{-1} at a centre-of-mass energy of $\sqrt{s} = 13 \text{ TeV}$. The maximum instantaneous luminosity of the LHC machine in 2015 is determined to be $5 \times 10^{33} \text{ cm}^{-2}\text{s}^{-1}$. With a bunch spacing of 25 ns and considering the number of colliding bunches, one can conclude that roughly 10 collisions occur per bunch crossing. This reflects the problem that beside the physically interesting interactions many other interactions take place. This is called pileup, whose influence on the analysis will be discussed later.

3.2 Compact Muon Solenoid

The Compact Muon Solenoid (CMS) is a general multi-purpose detector. A view inside the CMS detector is given in figure 3.2. The main goals of the design is the full coverage of the interaction region and the high precision measurement of outgoing particles. The detector is divided into a barrel region and two endcap regions. The centrepiece of the detector is the superconducting solenoid providing a homogeneous magnetic field of 3.8 T along the beam direction which causes charged particles to bend and consequently allows to measure the momentum of charged particles. In order to perform the measurement as accurate as possible the innermost subdetector of CMS is a silicon tracker. Going outwards, you can find the electromagnetic and hadronic calorimeter to determine the energy of the particles.

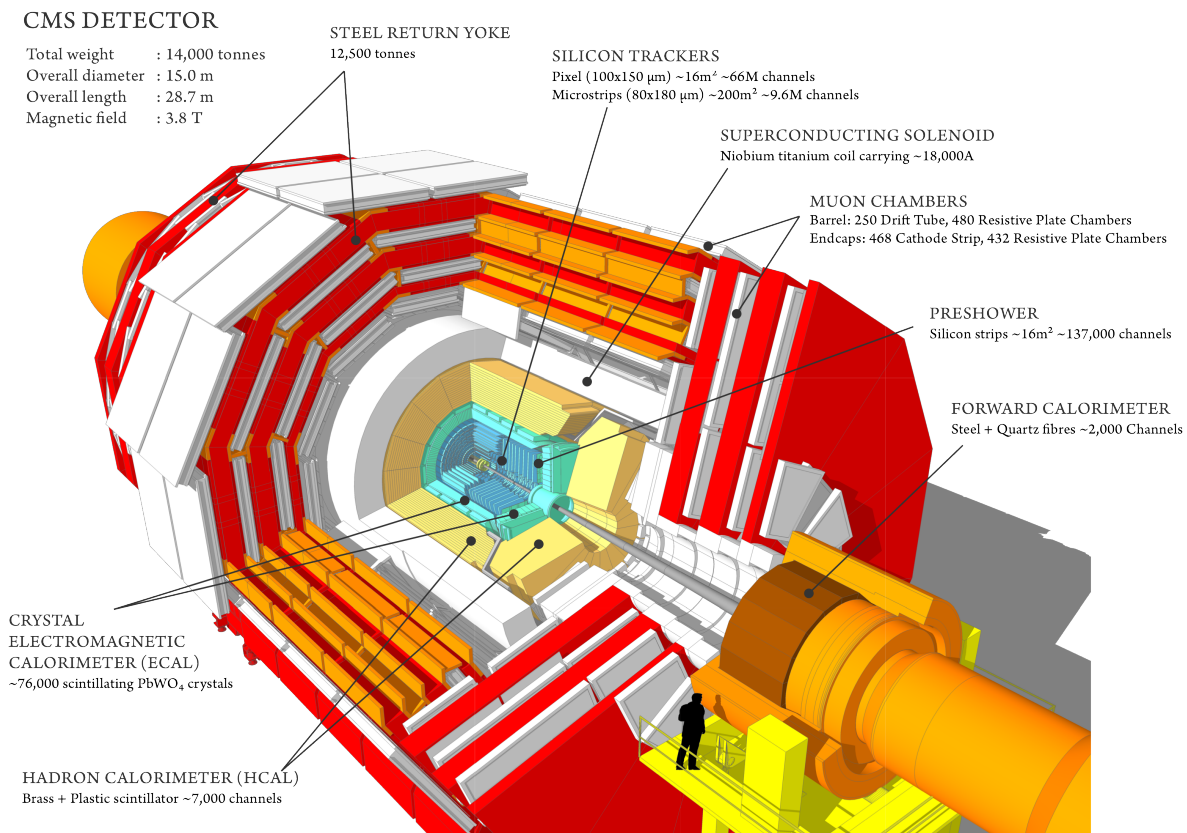


Figure 3.2: View inside the CMS detector: The different subdetectors with their properties are shown. [46]

Outside of the superconducting solenoid there are the muon detectors. In order to confine the magnetic field an iron magnet return yoke is interleaved inside the muon chambers. In total the CMS detector is roughly 28 m long, 15 m wide and 15 m high and weighs about 14×10^3 t, mostly caused by the return yoke.

3.2.1 Coordinate System

One has to fix a spatial coordinate system to be able to describe positions and directions inside the CMS detector. By setting the origin at the nominal interaction point (centre of the CMS detector) and letting the x -axis point towards the centre of the LHC, the y -axis point upwards and the z -axis point in beam direction, we define a right-handed Cartesian coordinate system. However, it is often more comfortable not to use the Cartesian coordinates but instead spherical coordinates. The azimuthal angle ϕ is measured in the xy -plane starting from the x -axis. The polar angle θ is measured starting from the z -axis. One can transform the polar angle by writing

$$\eta = \ln \left(\tan \frac{\theta}{2} \right).$$

This new quantity is called pseudorapidity. This variable transformation is done since differences in pseudorapidity are invariant under Lorentz transformations and thus better to handle in physics analyses. Another variable is defined by

$$\Delta R = \sqrt{\Delta\eta^2 + \Delta\phi^2},$$

which gives the distance of two different directions in the $\eta\phi$ -plane.

3.2.2 Tracker

The precise measurement of the momentum of particles emerging from the collisions is crucial in order to find out what happened at the collision point. Furthermore, we know that for a charged particle the saying 'the more curved its track inside a magnetic field is, the less momentum it has' holds. Thus, a possibility to get the momentum of particles is to measure their tracks. This is the purpose of the tracker inside the CMS detector. The CMS tracker consists of pixel barrel layers starting at a radius of 4.4 cm and silicon strip layers reaching up to a radius of 1.1 m. In the endcaps, the tracker system is completed by 2 disks in the pixel region and 12 disks in the silicon strip region. Figure 3.3 presents a schematic view of the different components. One can also see the covered η range of the tracking system $|\eta| < 2.5$ in figure 3.3. In total the tracker has a length of 5.8 m and has 2.5 m in diameter. Thanks to the CMS solenoid a 3.8 T magnetic field penetrates the whole volume of the tracker.

One has to bear in mind that the tracker has to withstand the harsh environment of the LHC. Due to its design luminosity of $10^{34} \text{ cm}^{-2}\text{s}^{-1}$ one expects products of roughly 20 proton-proton interactions per bunch crossing, i.e. every 25 ns. Thus, a compromise has to be found between the ability to measure the track (spatial resolution) and the life-time of the tracker as well as the fast readout electronics. In this light, it is astonishing that the tracker manages to measure the momentum at percent level. A particle with momentum of $p = 100(1000) \text{ GeV}$ can be measured with a resolution of $\frac{\Delta p}{p} \approx 1(5)\%$ [48]. The order of magnitude for the impact parameter is about $10 - 100 \mu\text{m}$ depending on the η and momentum of the particles [47].

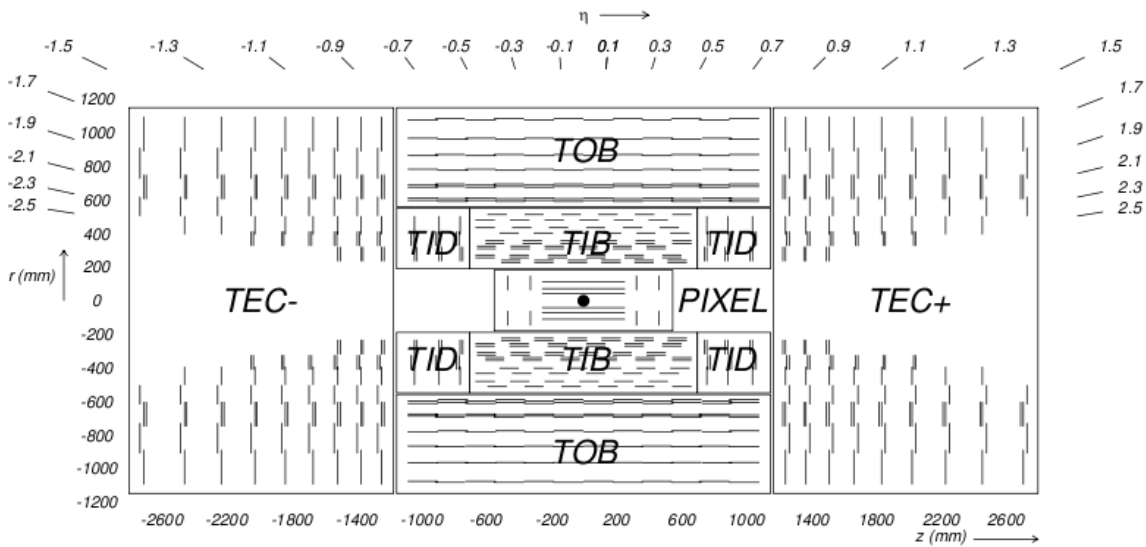


Figure 3.3: Schematic layout of the CMS tracker in the rz -plane. Components of the tracker system: PIXEL (inner pixel layers), TIB/TID (tracker inner barrel/disk layers), TOB (tracker outer barrel) and the TEC (tracker endcap layers). [47]

3.2.3 Electromagnetic Calorimeter

The electromagnetic calorimeter (ECAL) builds the centrepiece of the energy measurement of electrons, positrons and photons. However, one should also add hadrons to the list of particles whose energy is measured by the ECAL, since they are also depositing a non-negligible amount of energy inside the ECAL. In a simplified way the main physical processes that contribute to the detection method are introduced in the following. Suppose a photon traverses the ECAL material. After a certain distance, it can eventually produce an electron-positron pair via pair-production. Following the electron leg while traversing the material, it radiates Bremsstrahlung. Combining these processes, one obtains a so-called electromagnetic shower of positrons, electrons and photons. Assuming that, for the two processes, the energy of the initial particle is distributed approximately equally among the products one gets an estimation of the energy of the incoming particle by counting the number of photons inside the shower at several depths of the shower.

Figure 3.4 offers a view of the ECAL layout. The ECAL is made of lead tungsten (PbWO_4) crystals. It is divided into two parts. One of them is the barrel part (EB) which covers a pseudorapidity range of $|\eta| < 1.479$. The other part called endcaps (EE) covers $1.479 < |\eta| < 3.0$. The barrel part consists of 61200 crystals and each endcap consists of 7324 crystals. The lead tungsten crystal length in the barrel is 23 cm which corresponds to 25.8 radiation lengths.¹⁶ The endcap crystals are slightly shorter (22 cm or 24.7 radiation lengths) since a preshower of 3 radiation lengths of lead is installed [49]. The emitted light is detected by avalanche photodiodes in the barrel and by vacuum phototriodes in the endcaps. This difference is due to different level of radiation in the two regions. In general, the photo-detection has to fulfil high expectations, namely a fast response, high radiation tolerance and a good ability to operate inside the magnetic field.

¹⁶A radiation length is the distance after which the remaining energy of an electron is $\frac{1}{e}$ of the initial energy.

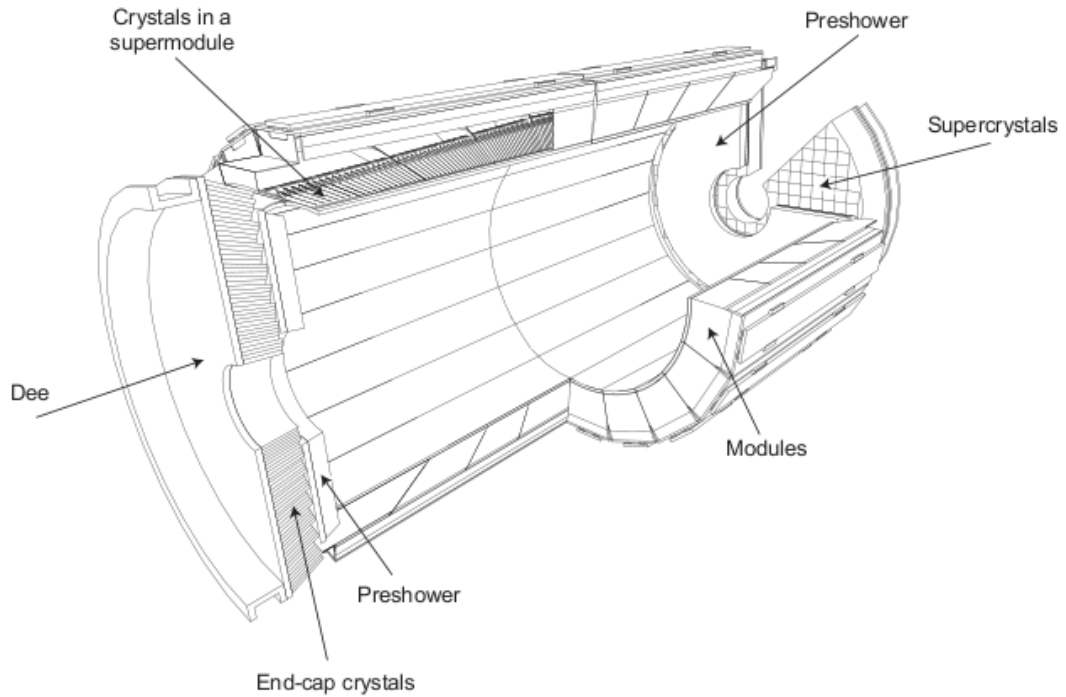


Figure 3.4: Layout of the CMS ECAL: Arrangements of crystal modules in barrel and endcaps with the preshower in front. [47]

The energy resolution of the ECAL is determined to be

$$\frac{\sigma}{E} = \frac{2.8\%}{\sqrt{E/\text{GeV}}} \oplus \frac{12\%}{E/\text{GeV}} \oplus 0.3\%$$

divided into a stochastic, noise and constant term [50]. The \oplus specifies that the errors are combined in quadrature.

3.2.4 Hadronic Calorimeter

The main purpose of the hadronic calorimeter (HCAL) is to determine the energy of hadronic jets. Additionally, the HCAL is indispensable for a precise measurement of missing transverse energy which relies on the energy measurement of all detectable particles. Due to nuclear interactions with the detector material hadrons are stopped inside the calorimeter. The energy deposited by the hadrons leads to various types of excitation and ionizations of the atoms and nuclei inside the HCAL. By emitting radiation light, these excited states return to their ground state. The emitted light can be detected. One could say that this is a similar principle as in the electromagnetic case, only applied in the context of the strong interaction.

The hadronic calorimeter barrel (HB) and the two endcaps (HE) sit behind the tracker system and electromagnetic calorimeter as seen from the interaction point (see figure 3.5). The barrel covers $|\eta| < 1.3$ and the endcaps $1.3 < |\eta| < 3.0$ in pseudorapidity. There are two additional modules of the HCAL. One is placed in the very forward direction (HF) $|\eta| < 5$ and the other module named hadron outer (HO) sits outside of the magnet and catches all remaining hadrons escaping the barrel and endcaps of the HCAL. The HCAL is a so-called

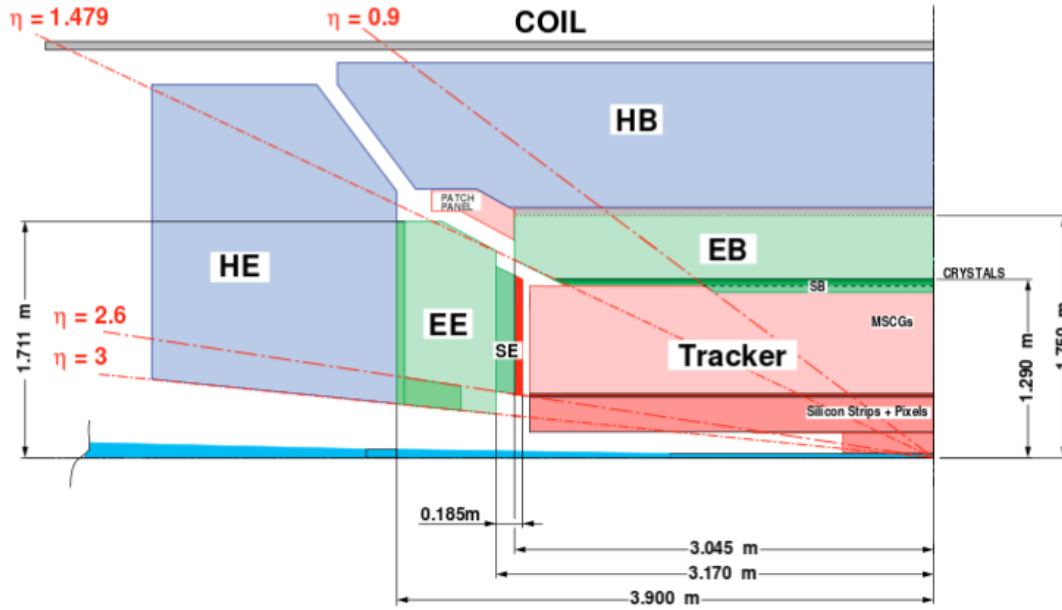


Figure 3.5: Quadrant of the calorimetry and tracking system presenting the size of the components and which pseudorapidity range is covered. [49]

sampling calorimeter stating that the particle's properties are measured by alternating layers of plastic scintillators as an active material and flat brass absorbers which are made of copper (70 %) and zinc (30 %). When a particle passes through, the induced light in the scintillators is collected by optical fibres and finally read out by photodiodes.

Test beam studies have determined the energy resolution of pions using the complete calorimetric system to be

$$\left(\frac{\sigma}{E}\right)_{\text{pions}} = \frac{127\%}{\sqrt{E/\text{GeV}}} \oplus 6.5\%.$$

The first error is a stochastic term and the second error is a constant contribution [51].

3.2.5 Superconducting Magnet

The CMS superconducting magnet has been designed to provide a homogeneous magnetic flux density of 4 T at the center of CMS. The magnet has a 6-m diameter and a magnetic length of 12.5 m. At a nominal current of about 19 kA and an inductance of 14.2 H an energy of 2.6 GJ can be stored inside the magnet. The iron yoke is installed to return the magnetic flux and is the heaviest part of the CMS detector and weighs 10000 t. Instead of operating the magnet at the full 4 T, a magnetic flux density of 3.8 T is chosen due to unknown aging effects of the coil [52].

3.2.6 Muon System

The name 'Compact Muon Solenoid' already suggests that identifying muons and measuring their trajectories is one of the main purposes of the detector. Muon reconstruction is a crucial task in the context of this analysis which looks into the electron-muon channel and also in many other BSM searches. Thus the muon system deserves some considerations.

The muon detectors are located at the very edge of the detector outside the magnet and the calorimetric system since muons can penetrate several meters even in iron without being stopped, whereas all other particles, except neutrinos, which are considered as missing transverse energy, should be stopped inside the magnet.

The muon system consists of in total 1400 chambers divided into 250 drift tube chambers (DTs) in the barrel and 540 cathode strip chambers (CSCs) in both endcaps. The hits of a traversing particle in the DTs and CSCs are used to reconstruct the particle's track and provide a trigger. A redundant trigger system is formed by 610 resistive plate chambers (RPCs) both in barrel and endcaps. For precision measurements, the DTs in the barrel, where the particle flux is lower, and the CSCs in the endcaps, where the particle flux is higher, are used. The RPCs are installed in both the barrel and the endcaps. The spatial resolution per chamber of the DTs and CSCs is in the order of $100 \mu\text{m}$, whereas for the RPCs the spatial resolution is about 1 cm [53]. The DTs cover $|\eta| < 1.3$, the CSCs $0.9 < |\eta| < 2.4$ and the RPCs $|\eta| < 2.1$ in pseudorapidity [54]. One can see the geometry of a CMS quadrant showing the different components and their geometrical sizes in figure 3.6.

The drift tubes are made of individual drift cells. Figure 3.7 illustrates a drift cell together with its electric field configuration. Each drift cell has a cross section of $13 \times 42 \text{ mm}^2$ and is filled with a Ar/CO_2 gas mixture, where one keeps the concentration of CO_2 in the range of $10 - 20 \%$. The cell consists of a gold-plated stainless-steel anode wire which has a diameter of $50 \mu\text{m}$. The cathode strips and the field electrodes are made of aluminium tape. When muons are passing through the gas volume, they ionize the gas molecules. Due to the electric field inside the cell, electrons and ions are separated and drifting away from each other to the anode and cathode. With the gas amplification near the central wire, a readable signal is obtained.

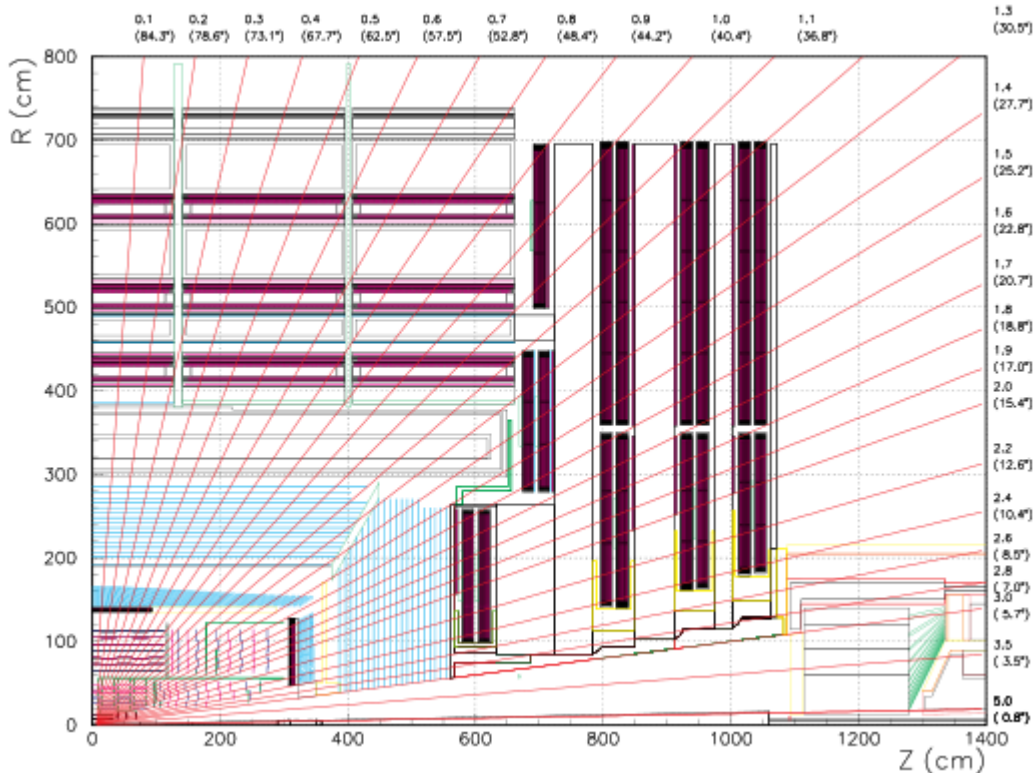


Figure 3.6: Quadrant of the CMS detector: the outer part in reddish colour are DTs (horizontal), RPCs (horizontal/vertical) and CSCs (vertical). [54]

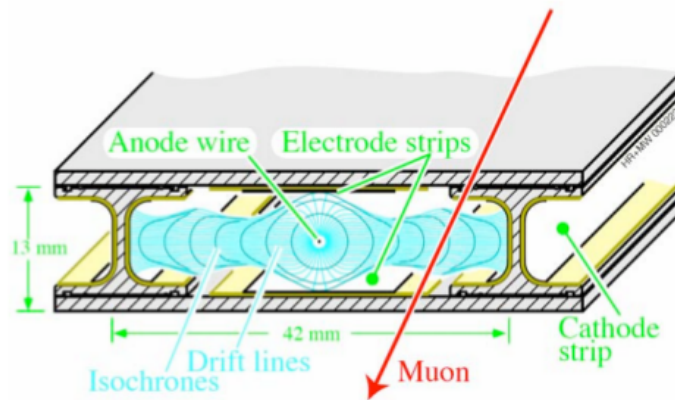


Figure 3.7: Drift cell of the muon DT chambers shown together with the electric field configuration. One can see the electrodes, isochrones and the drift lines. [47]

The cathode strip chambers belong to the class of multi-wire proportional gas chambers. A schematic view of the detection principle can be found in figure 3.8. The muon passes the gas volume and again ionizes the gas molecules causing the electrons to drift towards the anode wires. The avalanche of electrons due to the high electric field induces a charge in the cathode strips. Both information of the wires and cathode strips can be used to reconstruct a hit of a traversing muon. The CSCs provide a precision measurement and muon trigger in one device. The CSCs operate in an environment of high particle rates and large and inhomogeneous magnetic fields. This is why the CSCs are installed in the endcaps of the CMS detector [47]. The resistive plate chambers can be classified as gaseous parallel plate detectors. Besides a good spatial resolution, the RPCs offer a time resolution which is in the order of 3 ns. That is an important feature of the RPCs regarding the trigger system since there is only 25 ns between two consecutive bunch crossings at the LHC. 6 layers of RPCs are installed in the barrel region, where there are 2 layers located in each of the 2 innermost muon stations. With this redundancy, the trigger algorithm has access to at least 4 layers even for low- p_T muons.

Finally, the muon momentum resolution is a decisive figure-of-merit for the muon system. The standalone momentum resolution is for low- p_T muons ($p_T < 100$ GeV) 6%–12% and, for $p_T = 1$ TeV, 20% (barrel). Fortunately, one can combine the information from the

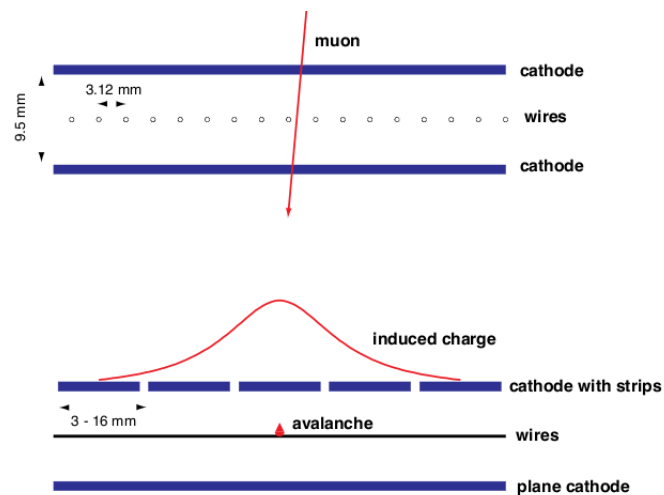


Figure 3.8: Principle of the muon detection with the CSCs. The traversing muon ionizes the gas molecules. The resulting free electrons are accelerated towards the wire and produce on their way new electrons causing a shower. The induced charge on the cathode strips can help to obtain a precise localisation of the avalanche along the wire direction and thus the localisation of the traversing muon.[47]

muon system with the inner tracker system resulting in a significantly better resolution. For low- p_T muons one gets 1%–2% and for $p_T = 1$ TeV a momentum resolution of 5% (barrel) [54].

A severe difficulty is to align the muon system among itself (barrel and endcap) and, more importantly, with respect to the inner tracker. The deformation of the iron yoke due to high magnetic fields puts limits on the momentum resolution. Solutions to the alignment problem can be found in [54].

3.2.7 Triggering, Data Acquisition and Computing

In 2015 Run-II data taking the bunch spacing is 25 ns resulting in a rate of 40 million collisions per second. To read-out and store all information of every event would be impossible¹⁷. Thus, a dedicated trigger system is needed to select events that are interesting for physical searches. The trigger decreases the rate so far that the data can further be stored on computer disks and in the end can be analysed.

The trigger system consists of 2 stages. The level-1 trigger is extremely fast and looks for simple signs of interesting physics, e.g. high energy depositions in the calorimeter system. After the level-1 trigger the rate of events is ~ 100 kHz. This is followed by a high-level trigger system (HLT), which performs a very basic reconstruction of the physical objects. The remaining event rate is ~ 100 Hz. Events passing both trigger stages are stored for offline analyses [55].

The generated data is then transferred to and stored at the Worldwide LHC Computing Grid (WLCG). The full reconstruction of the data events as well as the Monte Carlo (MC) simulation of events is done by this grid infrastructure. There are more than 170 computing centres in 42 countries participating [56].

¹⁷Additionally, reading out all events would most probably give only uninteresting low-energy collisions and the power to reveal new phenomena would be suppressed.

4 Physical Objects

This chapter will introduce those physical objects that are most relevant for this analysis, namely the muon and the electron. We will discuss the reconstruction algorithms and trigger stream of both the muon and the electron.

4.1 Muon

A muon traverses the detector depositing only a small fraction of its energy in the calorimeter system since muons are minimum ionizing particles. Thus the calorimeter system alone cannot be used to reconstruct muons. Instead the muon system and the tracker are used. Since all other detectable standard model particles should be stopped inside the calorimeter system, we expect only muons to deposit energy in the muon systems. This fact allows to construct a high-efficiency trigger for muon candidates.

In this section we first discuss the reconstruction algorithms of the muon candidates. Then we will talk about some general muon selection criteria and finally spend a few words on the muon trigger stream.

4.1.1 Muon Reconstruction

The track reconstruction algorithm fulfils the task to reconstruct a track from the different hits in the tracker system and muon detectors by fitting. The types of algorithms differ in what kind of hits are used in the fit procedure. Independent of what hits are used in the fit all types of algorithms follow a general sequence consisting of 4 stages.

The first stage is called Seeding. An estimated trajectory state or a set of hits that are compatible with the assumed physical process is used to find an initial point for the track reconstruction. The state-based seeds do not need any hits but instead a track segment with initial momentum and direction in the DTs or CSCs. The requirement for the hit-based seeds is that they should be compatible with the beam spot. This allows to attach an initial vector to the trajectory seed. Consequently, both types of seeds (hit-based and state-based) provide a direction which is used in the next stage. After Seeding the Trajectory Building is performed. Starting from the position of the trajectory seed one proceeds in the direction given by the seed to find compatible hits in subsequent detector layers. Now the track finding and fitting is performed with special combinatorial filters¹⁸. The output gives a huge amount of trajectories which is cleaned from ambiguities such as an overlap of the used hits. This is called Trajectory Cleaning. In the final stage denoted Trajectory Smoothing a backward fitting (smoothing) to all hits surviving the Cleaning is applied in order to take the full covariance matrix for the final fit track into account.

The algorithm determines a track from which the particle's properties such as momentum, energy and direction are extracted. All inputs of the track finding procedure have uncertainties which are propagated to the particle's properties and are stored for every track.

A short description of the different types of muon candidates (corresponding to different sets of hits used in the track fitting procedure) is given below. There are three basic reconstruction algorithms namely standalone muon, global muon and tracker muon:

- *Standalone muon*: The seeds for this algorithms are trajectory estimates by matching pairs of DT segments, CSC segments or both together and extracting the momentum from the curvature. The fit is done by picking up and fitting CSC and RPC hits and DT segments along the trajectory.

¹⁸More information on the combinatorial filters can be found in [57] and in its list of references.

- *Global muon*: These muons are a combination of the standalone muons with a matching track from the tracker. Seeds are standalone muons and matching tracks. The fit is performed with the track candidate hits and hits from layers that are crossed by the standalone muon. The track of the global muon is the one with the best fit probability. Since the momentum resolution for tracks up to $p_T = 200$ GeV reconstructed in the muon system only is dominated by multiple scattering, the tracker information is the best choice to reconstruct muons in this momentum region. Above that threshold, a combination of the tracker track and the standalone muon improves the momentum resolution.
- *Tracker muon*: Basically it is the opposite strategy compared to that of the global muon. The tracker muon algorithm starts with a tracker track and searches the corresponding muon signatures in the muon systems. This algorithm was invented to overcome problems with missing hits in the muon systems, e.g. due to low momentum.

However, several difficulties occur when reconstructing a high- p_T muon which is part of the signature this analysis is looking for. First of all, the curvature of the muon track in the magnetic field can not be measured that easily since the sagitta¹⁹ is inverse proportional to momentum and thus decreasing with increasing momentum and finally affecting the momentum measurement. Additionally high- p_T muons can radiate bremsstrahlung, e.g. when propagating through the iron causing electromagnetic showers. To overcome these challenges other, more sophisticated, reconstruction algorithms have been developed and used:

- *TPFMS muon*: The starting point of a TPFMS (Tracker Plus First Muon Station) muon is a global muon. The add-on is that the trajectory of the muon is refitted using only the tracker and the innermost available segment of the muon system. This has the advantage that even high- p_T muons with its radiation mostly in the iron yoke can be reconstructed well.
- *Picky muon*: In this case also the global muon reconstruction builds the starting point from which muon stations with high occupancy are subtracted since it is more likely that the muon produced an electromagnetic shower there. The criterion to eliminate these stations is a χ^2 fit. After elimination a refit is done.
- *TuneP muon*: This algorithm chooses the best reconstruction out of the above mentioned. The choice is based on a track-by-track evaluation using goodness-of-fit variables for each option.

The muon reconstruction used in this analysis relies on the TuneP algorithm. A more complete discussion of the reconstruction algorithms can be found in [57] and [58].

The muon momentum resolution is a decisive figure-of-merit for the CMS muon systems. The resolution is determined separately with only the tracker, with only the muon spectrometer and once with the full CMS tracker system. The differences in muon momentum resolution of these procedures are shown in figure 4.1.

It is worth mentioning that the reconstruction power of the muon detectors is limited by the quality of alignment. When combining the tracker system and the muon detectors in the reconstruction algorithm, one has to know the position and orientation of the two systems relative to one another. Dedicated studies to account for misalignment effects are performed in the CMS collaboration [57].

¹⁹For a circular arc, sagitta is defined as the distance from the centre of the arc to the centre of its base.

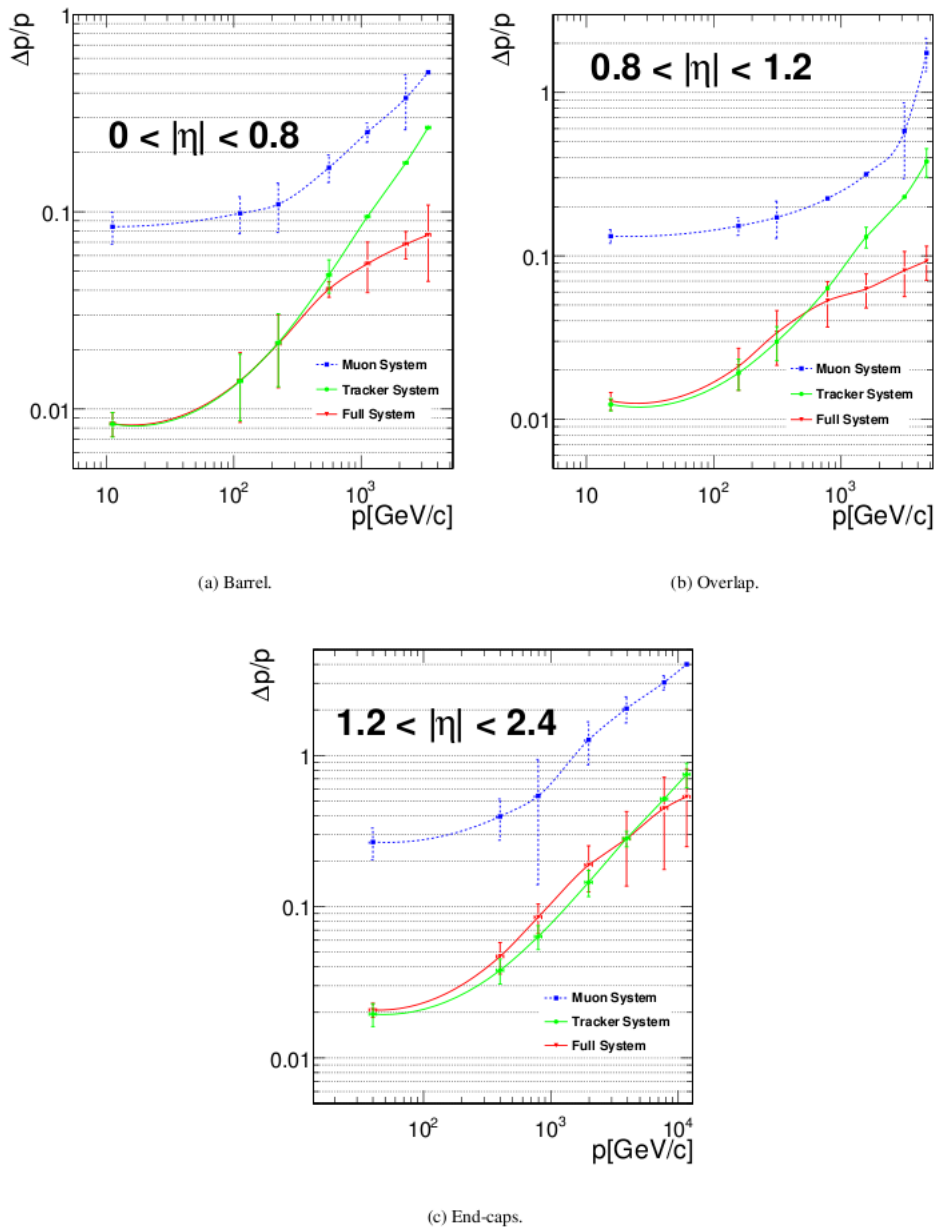


Figure 4.1: Muon momentum resolution as a function of momentum in different regions of pseudo-rapidity [57]. The resolution is determined with the tracker alone, with the muon spectrometer only and with the full CMS tracking system.

4.1.2 Muon Selection

The selection for high- p_T muons recommended by the Muon Physics Object Group (POG) [59] of CMS is used in this analysis. The following list gives a complete overview of the muon selection.

- The muon is required to be reconstructed as a global muon.
- The global-muon track fit should include at least one muon-chamber hit in order to suppress hadronic punch-through and muons from decays in flight.
- Muon segments should show up in at least two muon stations. This leads to further

suppression of punch-through and also a suppression of accidental track-to-segment matches. Furthermore, consistency with the muon trigger logic is guaranteed since the trigger requires segments in at least two muon stations to obtain a meaningful estimate of the muon transverse momentum.

- The tracker track ought to have a transverse impact parameter²⁰ of $d_{xy} < 2$ mm and the longitudinal distance d_z of the tracker track from the primary vertex should be less than 5 mm. Cosmic muons are suppressed by these criteria and a further reduction of muons from decay in flight and tracks from pileup vertices is achieved.
- At least one pixel hit is requested in order to further reject muons from decays in flight.
- Since a minimal number of tracker layers with hits guarantees a precise p_T measurement, more than 5 tracker layers with hits are required.

On top of this muon selection, cuts on muon candidates at analysis level are applied. This is the topic of section 5.5.1.

4.1.3 Muon Trigger

Due to the possibility to identify muons with a high efficiency over a large p_T range, muon candidates can also be used to define a trigger stream. In section 3.2.7 general aspects of the trigger system have been discussed. Thus, here, we only focus on the muon-specific features, i.e. the level-1 (L1) muon trigger and the single muon high-level trigger (HLT).

This analysis uses the unrescaled HLT_Mu50 trigger path, which is seeded by either L1_SingleMu16 or L1_SingleMu25. There are no isolation requirements on the HLT_Mu50 trigger path. The requirement on the transverse momentum of the muon candidate is $p_T > 50$ GeV [60].

The level-1 muon trigger is implemented in hardware and uses hits from the muon system. The muon candidates found by the level-1 trigger provide the seeds for the high-level trigger²¹. These seeds define a region of interest in the muon system which is the starting point of the trigger (online) reconstruction. Details about the trigger streams and their reconstruction can be found in [61].

4.2 Electron

The electron is the second part of the signature we are looking at in our search and thus the reconstruction and trigger streams of the electron deserve some consideration. An electron emerging from a proton-proton collision deposits energy in the tracker and finally reaches the electromagnetic calorimeter. There the electron induces an electromagnetic shower.

4.2.1 Electron Reconstruction

Reconstructing electrons in CMS is based on information from the calorimeter system and the tracker. The starting point of the electron reconstruction consists of the energy deposited in crystals of the electromagnetic calorimeter. Summing up energy depositions in adjacent crystals, clusters are formed. In the next step, a cluster with a high energy deposit is chosen and several clusters within a ϕ window around the starting point are grouped

²⁰The transverse impact parameter d_{xy} is the distance in the xy -plane from the primary vertex. For d_z , there is a similar definition w.r.t the z -axis.

²¹Including candidates that are not accepted by the level-1 trigger but selected candidates in the level-1 trigger stream.

into a so-called supercluster. The ϕ window extends up to maximal 0.3 rad in both directions. Electrons are radiating bremsstrahlung when traversing the tracker material and subsequently via pairproduction electron-positron pairs are created inside the tracker volume. Thus the clustering procedure of ECAL crystals helps to collect the energy radiated by bremsstrahlung [62; 63].

The superclusters are then combined with hits from the innermost tracker layers. The energy and positions of the supercluster allow to calculate a first estimate of the electron's trajectory. One looks into the two innermost tracker layers to find a pixel hit which is compatible with the trajectory. A new estimate of the trajectory is built including the hits from the two innermost layers. The same procedure is done including more and more outer layers. It can happen that several trajectories are found at each stage. This is reduced to maximal 2 trajectories by applying a χ^2 criterion. A final fit is performed with all remaining hits requiring at least 5 hits in the tracker [64; 61]. The electron's energy and momentum can be extracted from both the trajectory and the energy depositions in the ECAL.

This reconstruction is ECAL-based. In CMS, there is also a tracker-based reconstruction with benefits for low- p_T electrons (no bremsstrahlung) which is not discussed here since we are looking at high- p_T objects. The isolation and identification criteria are listed in the analysis specific section 5.5.2.

Like in the case of muon reconstruction, also the electron reconstruction relies on two different subdetectors of the CMS detector. Consequently, the alignment of the ECAL relative to the tracker is studied and has been determined to be less than 10 μm [65]. The effect is not as big as in the muon case ($\sim 100 \mu\text{m}$) since both the tracker and the ECAL are inside the solenoid.

In the context of this analysis an issue which one has to handle is the background induced by jets faking electrons. Thus it is worth mentioning a feature in the electron reconstruction to reject hadronic signatures. The superclusters of the ECAL are preselected using a hadronic veto cut before matching to the pixel hits in the tracker. By summing up the energy deposited in the HCAL within a cone of $\Delta R = 0.15$ around the position of the superclusters energy, one can look at the ratio $\frac{H}{E}$ ²² and define a cut.

4.2.2 Electron Trigger

The HLT electron trigger stream uses all events passing the level-1 trigger. The basic requirements of the HLT selection consists of matching the superclusters in the ECAL to the pixel hits of the tracker. The energy deposited in the ECAL should match the reconstructed track momentum in the tracker volume. Additionally, the electron candidate is said to fulfil some isolation requirements [61].

The electron trigger used in this analysis is the HLT_Ele105_CaloIdVT_GsfTrkIdT which is seeded by either L1.SingleEG35 or L1.SingleEG40 or L1.SingleJet200. The requirement on the transverse energy of the electron is set to be $E_T > 105 \text{ GeV}$. Several requirements are implemented in this electron trigger. These requirements can be looked up in reference [66].

²²The ratio $\frac{H}{E}$ is defined as the energy deposited in the HCAL over the energy in the ECAL.

5 Analysis

In this chapter, the analysis of the electron-muon channel is described. The following sections explain what data are used, how the standard model background and new-physics processes are simulated. The analysis-specific selection is described. Finally, a discussion of the systematic uncertainties is presented. The analysis is done within the CMS collaboration and a documentation can be found in [67]. The basic analysis concepts are also used in the CMS 8 TeV analysis of the electron-muon channel [4].

5.1 Recorded Data

The data for this analysis were taken in 2015 with the CMS detector at $\sqrt{s} = 13$ TeV summing up to an integrated luminosity of 2.7 fb^{-1} [68]. Single electron and single muon datstreams are used in this analysis with the reconstruction version of December, 16th 2015. For the muon dataset the high level trigger HLT_Mu50 selects interesting events and for the electron dataset the high level trigger HLT_Ele105_CaloIdVT_GsfTrkIdT is used. In order to prevent double counting a veto of the HLT_Mu50 trigger is implemented in the offline analysis when running over the electron-triggered dataset. In general, a ‘logical or’ of the single muon/electron trigger is implemented. The advantage of this trigger strategy compared to a simple single muon trigger is explained in section A.3. Both trigger paths are explained in more detail in section 4.2.2 and 4.1.3 for the single electron and single muon trigger respectively.

5.2 Simulation

Most of the standard model background processes and all of the signal processes are predicted by Monte Carlo (MC) simulation²³. For the standard model background the MC generators PYTHIA 6 [69], POWHEG [70], MADGRAPH [71] and aMCatNLO [72] are used. The RPV-SUSY samples are generated using CalcHEP [73] interfaced with PYTHIA 8 [74] for parton showering and hadronization²⁴. For the QBH signal a dedicated QBH event generator [75] produces the events again combined with PYTHIA 8 for parton showering and hadronization. The Z' samples are generated with PYTHIA 8²⁵.

After generating the processes the FULLSIM CMS detector simulation is used to get the detector response of the different processes. GEANT 4 [76] provides the simulation of particle interactions with the detector material. The reconstruction and selection procedure of MC generated events is analogous to data events.

5.3 Scale Factors

The above mentioned detector simulation is a sophisticated tool to simulate physical processes. However, it can happen that the output of the detector simulation differs from actual data. This problem is addressed by introducing scale factors for

- Muon trigger,
- Muon identification,

²³Except the ‘Wjets + QCD’ background which is determined with a data-driven approach (see section 5.6.2).

²⁴Parton showering by PYTHIA adds additional jets to the events that were not considered by the other MC generators. Hadronization combines generated quarks into hadrons and subsequently into jets.

²⁵The RPV-SUSY, QBH and Z' samples are hereafter often referred to as signal samples. Details of signal samples can be found in section A.4

- Muon isolation,
- Electron identification and
- Electron trigger²⁶.

The muon trigger scale factors are given in table 5.1 for different regions in p_T and η . The values are determined by a Count Method described in [60]. For the muon identification a

p_T range (GeV)	$ \eta $ range	Scale factor	Stat. Uncert.	Syst. Uncert. (frac. of SF)
$53 < p_T < 140$	$ \eta < 0.9$	0.9724	± 0.0010	0.005
	$0.9 < \eta < 1.2$	0.9656	± 0.0026	0.005
	$1.2 < \eta < 2.1$	0.9651	± 0.0015	0.005
	$2.1 < \eta < 2.4$	0.9584	± 0.0053	0.005
$140 < p_T < 5000$	$ \eta < 0.9$	0.969	± 0.011	0.005
	$0.9 < \eta < 1.2$	0.985	± 0.042	0.005
	$1.2 < \eta < 2.1$	1.006	± 0.022	0.005
	$2.1 < \eta < 2.4$	1.032	± 0.095	0.005

Table 5.1: Muon trigger scale factors and the associated statistical and systematic uncertainties as a function of the p_T and $|\eta|$ of the muon candidate. The $|\eta|$ ranges are following the geometrical arrangement of the components of the muon system. [60]

scale factor of 0.98 with a dominating systematic uncertainty of ± 0.01 is applied. For the muon isolation a factor of 1.00 ± 0.01 (syst) is used. Again the statistical error is negligible. These scale factors are determined by a Tag and Probe method [77].

The scale factor of the electron identification is given by 0.996 ± 0.002 (barrel) and 0.996 ± 0.005 (endcap) [78].

All scale factors mentioned above are used to reweight the selected events according to the kinematics of the selected electron-muon pair (see section 5.5).

5.4 Pileup

This section is concerned with corrections that take care of pileup effects. In section 3.1 there is an explanation of what pileup is and why it is important to take into account. Pileup denotes the effect of additional inelastic processes happening in the same or different proton-proton bunch crossings. To handle this effect, one needs to know the number of inelastic interactions in a fixed time range when a certain number of bunch crossings take place. This number can be obtained by measuring the instantaneous luminosity. Then, using the minimum bias cross section of inelastic proton-proton collisions $\sigma_{\text{inelastic}}^{pp} = 73.1$ mb at 13 TeV [79] one can determine the number of inelastic proton-proton collisions per time interval. This is measured separately for certain time ranges with the CMS detector in a complete run of the LHC. Comparing the obtained distribution of data with the simulation of the background and signal processes, one can reweight the simulated samples according to the measured pileup interactions. Figure 5.1 shows a comparison between data and simulated background as well as signal samples before and after pileup reweighting. One can clearly see that for the number of reconstructed primary vertices the agreement improves significantly.

²⁶The electron trigger scale factors are applied for the events triggered only by the electron trigger.

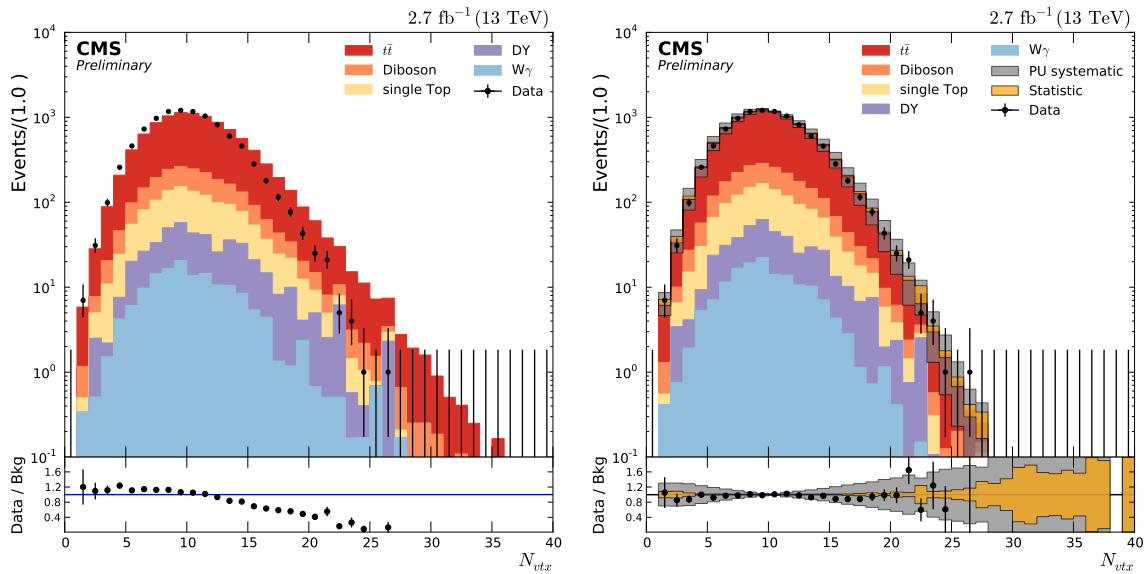


Figure 5.1: Number of reconstructed vertices before (left plot) and after (right plot) pileup reweighting. After the reweighting the systematic uncertainty due to the $\pm 5\%$ shift of the minimum bias cross section is shown as a grey shaded band. All shown events are required to pass the complete selection and contain therefore at least one electron and one muon. More information on the different background contribution shown here as coloured histograms can be found in section 5.6.

5.5 Analysis-Specific Selection

This section is devoted to the analysis-specific selection criteria for the muon and the electron. The criteria discussed in this section are applied on top of the criteria introduced in section 4.1 for the muon and in section 4.2 for the electron. The analysis-specific selection intends to be as model-independent as possible. With this general selection strategy, the results of this analysis can then be re-interpreted for all resonant-like signals decaying into an electron-muon pair.

5.5.1 Muon Criteria

The basic muon selection for high- p_T muons as recommended by the Muon POG of CMS is discussed in section 4.1.2. Additionally, other cuts are applied on analysis level. The muon candidate should have a $p_T > 53$ GeV in order to get around trigger turn-on effects. For the analysis only muons within the pseudorapidity range of $|\eta| < 2.4$ are used. The transverse momenta of measured tracks within a cone of $\Delta R < 0.3$ around the muon direction are summed up and divided by the muon transverse momentum. This ratio ought to be less than 10%. This is the tracker-based relative isolation criterion. This criterion is applied in order to reject muons that are part of a jet.

5.5.2 Electron Criteria

The electron selection of the analysis follows the High Energy Electron Pairs identification (HEEP ID) version 6.0 of the CMS EGamma POG [80]. Table 5.2 shows the complete list of all criteria. This list contains identification and isolation requirements at the same time. In the following the variables in table 5.2, which are not introduced so far, are discussed [80]:

- **isEcalDriven:** The reconstruction of the electron should be seeded by the calorimeter system.

- $|\Delta\eta_{in}^{seed}|$: The difference in η of, on the one hand, the track measured by the inner layer of the tracker system and subsequently extrapolated to the interaction vertex and extrapolated to the calorimeter and, on the other hand, the η of the superclusters in the calorimeter.
- $|\Delta\phi_{in}|$: The difference in ϕ determined with the same procedure as in the η case.
- H/E : We already know that this denotes the ratio of the energy deposited in the HCAL over the energy deposited in the ECAL. More explicitly, the energy of the ECAL is the energy of the electron's supercluster and in the HCAL case a cone of radius $\Delta R = 0.15$ around the electron's direction is defined to sum up all energy depositions in the HCAL. A tight cut on this variable helps rejecting jets.
- $5 \times 5 \sigma_{i\eta i\eta}$: This defines a measure of the spread in η in units of ECAL crystals of the electron's energy in a 5×5 block around the seed crystal. Details can be found in [81].
- $5 \times 5 E^{2 \times 5} / E^{5 \times 5}$: This variable is another measure of the spread. Here, the ratio of the highest energy 2×5 block containing the seed crystal over the total energy of the 5×5 block of the seed. It is shown in [82] that this further helps rejecting jets.
- EM + Had Depth 1 isolation: This isolation criterion uses both electromagnetic and hadronic isolation. The ECAL isolation uses the energy depositions of reconstructed hits with a certain energy threshold (barrel: $E_T > 0.08$ GeV, endcap: $E_T > 0.1$ GeV) in a cone of radius $\Delta R = 0.3$ around the electron's direction in the calorimeter excluding those hits within an inner cone with radius of 3 crystals. The hadronic isolation criterion sums up all energy deposition within a radius of 0.3 around the electron's position, excluding a cone of 0.15.
- Track Isolation: This isolation criterion is defined as the p_T sum of all tracks in a cone with the radius $\Delta R = 0.3$ excluding the inner cone within $\Delta R \leq 0.04$. This rejects electrons which are part of a jet since this quantity should assume low values for isolated electrons and high values for non-isolated electrons.

Variable	Barrel	Endcap
E_T	> 35 GeV	> 35 GeV
η range	$ \eta_{SC} < 1.4442$	$1.566 < \eta_{SC} < 2.5$
isEcalDriven	$= 1$	$= 1$
$ \Delta\eta_{in}^{seed} $	< 0.004	< 0.006
$ \Delta\phi_{in} $	< 0.06	< 0.06
H/E	$< 1/(E/\text{GeV}) + 0.05$	$< 5/(E/\text{GeV}) + 0.05$
full $5 \times 5 \sigma_{i\eta i\eta}$	-	< 0.03
full $5 \times 5 E^{2 \times 5} / E^{5 \times 5}$	> 0.94 OR $E^{1 \times 5} / E^{5 \times 5} > 0.83$	-
EM	$< 2 + 0.03 * (E_t/\text{GeV}) + 0.28 * \rho$	$< 2.5 + 0.28 * \rho$ for $E_t < 50$ GeV else
+ Had Depth 1 isolation		$< 2.5 + 0.03 * ((E_t/\text{GeV}) - 50) + 0.28 * \rho$
Track Isolation	< 5	< 5
Inner Layer Lost Hits	≤ 1	≤ 1
$ d_{xy} $	< 0.02 cm	< 0.05 cm

Table 5.2: HEEP ID (v6.0) cuts for electron. The criteria are applied to select electrons in this analysis. A description of the meaning of each variable can be found in the text. The variable E_t is defined by the supercluster's energy times $\sin \theta_{\text{trk}}$. θ_{trk} denotes the polar angle of the electron's direction measured at the inner tracker layer.

- Inner Layer Lost Hits: The track of an electron candidate is extrapolated towards the beam-line. By counting the number of times the extrapolation crosses active tracker material without a valid hit we obtain the number of lost hits. By cutting on this variable one intends to suppress electrons coming from conversions of prompt photons since it is very likely that the conversion happens somewhere inside the inner tracker.
- $|d_{xy}|$: The transverse impact parameter d_{xy} gives the distance of the track to the primary vertex. Again, we want to reduce the impact of non-prompt electrons.

5.5.3 General Selection Criteria

This section presents a list of general selection criteria applied on an event-by-event basis.

First of all, each event should contain at least one good muon (section 5.5.1) and one good electron (section 5.5.2). We further introduce an electron veto if a global muon with $p_T > 5$ GeV is found within a cone of $\Delta R < 0.1$ in order to account for muons that produce bremsstrahlung and subsequently produce superclusters in the ECAL. In events that are triggered by the single electron trigger and not by the single muon trigger, an additional cut on the p_T of the electron is applied in order to avoid trigger turn-on effects. A threshold of $p_T > 120$ GeV is introduced. Above that the efficiency that an electron passing the HEEP ID criteria matches the single electron requirements is 99 % [83]. Finally if there is more than one electron-muon pair in one event, we choose the pair with the highest invariant mass. The invariant $e\mu$ mass is defined by

$$M_{e\mu} = \sqrt{(p_e + p_\mu)^2}, \quad (5.1)$$

where $p_{e/\mu}$ are the 4-momenta of the electron and muon, respectively. The invariant $e\mu$ mass is invariant under Lorentz-transformations. This quantity plays a decisive role in the statistical interpretation of the results. It is required that all events pass the conditions of several missing-transverse-energy filters. Since the filters have almost no influence on the analysis they are only mentioned here for completeness. A list of all applied filters is given in [67]. Further explanations of the filters can be found in [84].

Other cuts are not applied due to different reasons. In general, the selection strategy aims to be as model-independent as possible. Additional cuts would undermine that strategy. In the following, some cuts and their advantages and disadvantages are discussed. None of the cuts mentioned below are included in the selection of this analysis.

A cut on opposite sign of the electron-muon pair would reduce the fraction of $t\bar{t}$ background. However, the cut is not used in this analysis to keep the analysis unaffected from lepton charge misidentification. In 7 TeV data, the lepton charge misidentification is measured in $Z/\gamma^* \rightarrow e^+e^-$ data for electrons. The charge misidentification probability is 0.1 % in the ECAL barrel and 0.3 % in the ECAL endcaps [85].²⁷ For muons, the charge misidentification probability is less than 10^{-4} and measured with cosmic rays [86]. One could also think about a b-jet veto or a cut on the $\Delta\phi(e, \mu)$. The cut on $\Delta\phi(e, \mu)$ would be motivated by the fact that the electron and muon are expected to be back-to-back for the signal signature. This can be seen in figure A.4. The b-jet veto would decrease the amount of $t\bar{t}$ background since this background has - most probably - two b-jets originating from the decay of the top-antitop pair. The 8 TeV $e\mu$ analysis [4] checked the influence of those cuts on the statistical interpretation. They found an improvement of the expected limit in the low mass region, whereas in the high mass region (> 1.2 TeV) there was none.

²⁷For very high- p_T electrons, this misidentification probability will increase. To be on the safe side in this kinematic regime, this analysis does not cut on the charge of the selected electron.

5.6 Standard Model Backgrounds

The standard model backgrounds for this search in the $e\mu$ final state can be divided in two categories. The first category, called prompt background, stems from standard model processes that actually have (among other particles) a muon and an electron in the final state. The second category is composed of processes that have a misidentified electron and/or muon, therefore called misidentified background. Contributions of each process from the two categories are determined separately and finally added to obtain the total event yield of the standard model prediction in the $e\mu$ channel. To finally compare the background event yield as a function of a kinematic variable to data it needs to be normalized to the integrated luminosity. A list of all backgrounds is given in section A.5 providing information for example about cross section, sample binnings and, if existing, the used MC generators.

5.6.1 Prompt Background

The dominating backgrounds for this analysis are among the prompt backgrounds. The leading background is the $t\bar{t}$ production followed by the diboson processes (WW, WZ, ZZ ²⁸). For invariant masses bigger than 1.5 TeV the WW becomes equally important as the $t\bar{t}$ production. Also single top processes are considered meaning the t and tW channels.

- $t\bar{t}$: The production of a top and an anti-top quark is the leading background in the $e\mu$ channel for a broad energy range. The top quark decays via a W boson most probable²⁹ into a b quark. The W boson subsequently decays into a lepton plus lepton neutrino pair. Similarly the anti-top decays. This case, if both W bosons decay leptonically, is often referred to as full-leptonic decay. If one of the leptons is an electron and the other one an anti-muon³⁰, one obtains a prompt background. For the high invariant mass region at $M_{ll} > 500$ GeV high statistics samples are used. These tail samples are produced only full-leptonically whereas the bulk samples include all decays. This background is produced with POWHEG.
- WW : The WW background is the most important fraction of the diboson background and becomes equally important as the $t\bar{t}$ background for invariant masses above 1.5 TeV. Again, this background contributes due to a full-leptonic decay of the W bosons and is produced for high masses with dedicated tail samples starting at $M_{ll} > 200$ GeV. All the WW samples are predicted by POWHEG.
- WZ and ZZ : These processes contribute much less to the final spectrum and are therefore only mentioned for completeness. They are also produced by POWHEG.
- Single Top: This name summarizes the backgrounds where a single (anti-)top is produced. This can happen in association with a W boson or quarks. Again by leptonic decay of the W boson one can obtain a muon and an electron in the final state.

5.6.2 Misidentified Background

The misidentified background consists of components that are determined by a MC generator, namely $W\gamma$ and Drell-Yan. The other component coming from 'Wjets + QCD' events are determined in a data-driven approach.

²⁸The diboson processes are ordered from dominant to subdominant.

²⁹See CKM matrix elements in section 2.1.

³⁰Of course, the same can happen with opposite charges.

The $W\gamma$ background contributes to the $e\mu$ channel since the W can decay into a muon and a muon-neutrino. The photon can be reconstructed as an electron which passes the selection. This happens for $W\gamma$ background only in rare cases since the photons are mostly low-energetic. Therefore, this background is very subdominant. This can be seen by looking at the high- p_T electron isolation and identification criteria in section 5.5.2.

We have to consider Drell-Yan processes ($Z/\gamma \rightarrow ll$) since either a muon can be reconstructed as an electron or vice versa and passes the selection criteria. Also tau-leptons are included in the Drell-Yan processes here, since a decay to 2 lighter leptons and two neutrinos can lead to an $e\mu$ pair in the final state.

The ‘ W jets + QCD’³¹ background consists of events where a jet is reconstructed as an electron or a muon which passes the corresponding selection. Since the latter case is less probable, only the electron case is considered. In contrast to all other background predictions of the standard model, the ‘ W jets + QCD’ background is not produced by a MC generator. Instead it is determined via a data-driven approach using the so-called ‘fake rate’ method. The idea and procedure of this approach will be explained in the following and is oriented towards the dielectron search in CMS [87]. To estimate the jet background via the data-driven approach one has to define an electron selection that is not as tight as the HEEP ID in the analysis. The basic idea of the cuts is to select ‘jet-like’ electrons. The variables and cuts are summarized in table 5.3. In the next step a dataset is selected with at least one muon passing the full selection and at least one electron passing the selection in table 5.3 but not the full selection defined in section 5.5.2. Both the QCD multijet and the W jets backgrounds are accounted for. Here, the QCD multijet is included since the cross section is a lot higher than for the W jets processes and thus, the probability that a jet fakes a muon is not negligible.

Now the ‘fake rate’ enters the game. The ‘fake rate’ is defined as the probability for a jet reconstructed as an electron to pass the HEEP ID. Of course in our case that probability has been determined with respect to the selection in table 5.3. Numerical values of the ‘fake rate’ can be seen in table 5.4. In each event the pair of the loose electron candidate and the muon candidate with the highest invariant mass is selected. Each event of the new dataset is reweighted by the factor $\frac{FR}{1-FR}$ evaluated at the E_T of the selected loose electron candidate. This dataset contains a non-negligible amount of prompt background which is subtracted using MC predictions in order to avoid double-counting. After subtraction the ‘ W jets + QCD’ background is obtained.

To check the validity of the data-driven approach the following test is done. We look at

variable	barrel	endcap
E_T	35 GeV	35 GeV
$ \eta $	< 1.4442	$1.566 < \eta < 2.5$
$\sigma_{i\eta i\eta}$	< 0.013	< 0.034
H/E	< 0.15	< 0.10
nr. missing hits	≤ 1	≤ 1
$ d_{xy} $	< 0.02 cm	< 0.05 cm

Table 5.3: The selection requirements for the starting point of the data-driven approach to determine the W jets+ QCD background. The cut values are taken from [87]. These requirements are less strict than the HEEP ID criteria. Especially, the H/E cut is not energy dependent and a lot looser than in the HEEP ID requirements.

³¹The name ‘ W jets + QCD’ denotes processes, where a W boson is produced in association with jets (W jets), and the QCD denotes processes of multijets.

Region	E_T range (GeV)	Functional form of 'fake rate'
barrel	$35 \leq E_T < 76.1$	$0.053 - 0.00059 \times E_T/\text{GeV}$
	$76.1 \leq E_T < 145.6$	$0.012 - (6 \times 10^{-5}) \times E_T/\text{GeV}$
	$E_T \geq 145.6$	0.00315
endcap $ \eta < 2.0$	$35 \leq E_T < 75.8$	$0.09 - 0.0008 \times E_T/\text{GeV}$
	$75.8 \leq E_T < 186.9$	$0.038 - (5 \times 10^{-5}) \times E_T/\text{GeV}$
	$E_T \geq 186.9$	0.0273
endcap $ \eta > 2.0$	$35 \leq E_T < 88.6$	$0.08 - 0.0005 \times E_T/\text{GeV}$
	$88.6 \leq E_T < 245.7$	$0.032 + (7 \times 10^{-5}) \times E_T/\text{GeV}$
	$E_T \geq 245.7$	0.051

Table 5.4: Functional form of the measured 'fake rate' for different kinematic regions. This has been determined with an independent single photon triggered dataset. The values of the functional form given in the right column are shown up to the digit where the statistical error of the parametrization starts. [87]

the invariant $e\mu$ mass plot which is explained in detail in section 6 and provides the basis for the statistical interpretation of this search. We compare the W jets background produced by a MC generator and the multijet contribution with the ' W jets + QCD' contribution from the data-driven approach. In the following it is explained how the multijet background, which is used in this comparison, is determined. On top of the usual event selection criteria, a charge requirement on the electron-muon pair is applied. The event yield of data and all backgrounds that are determined by MC generators as a function of the invariant $e\mu$ mass is shown in figure 5.2 left and right with the same-sign ($e^-\mu^-$ or $e^+\mu^+$) charge requirement and the opposite-sign ($e^+\mu^-$ or $e^-\mu^+$) charge requirement respectively. For the opposite

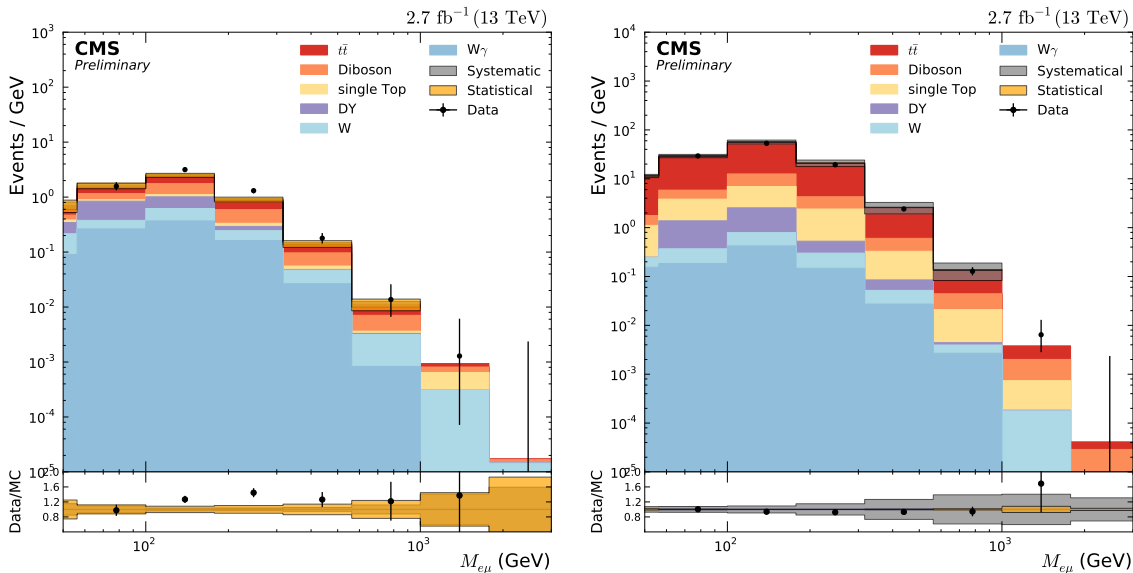


Figure 5.2: Event yield as a function of the $e\mu$ invariant mass. On top of the full selection opposite (right) and same (left) sign charge requirements are applied for the selected electron-muon pair. Here all backgrounds (including the W jets background from MC) are plotted except the data-driven ' W jets + QCD' background. We see a good agreement in the opposite sign distribution, whereas an offset between data and background can be observed in the same sign distribution. Twice this difference is taken as the multijet background in the cross check in figure 5.3

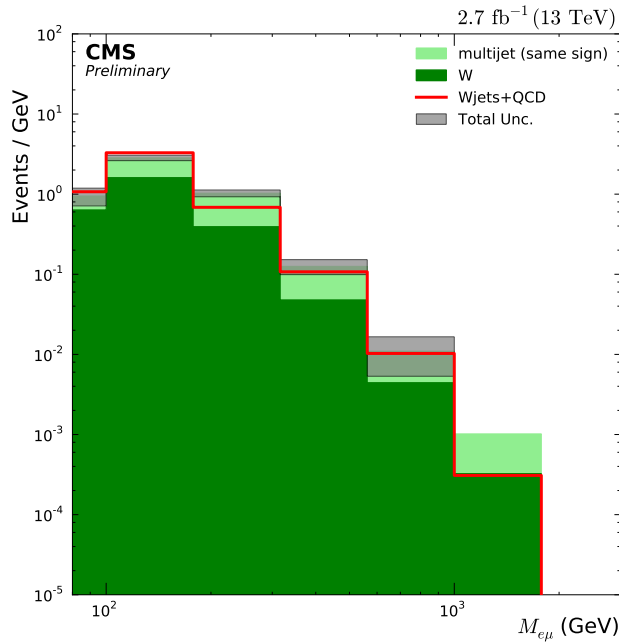


Figure 5.3: Comparison of the data-driven ‘Wjets+QCD’ (red line) with the W jets background determined by MC simulation, denoted by W in the legend, and the multijet background. The uncertainty in this plot is the total uncertainty of 50 % on the ‘Wjets + QCD’ background. The agreement provides a validation for the data-driven approach.

sign distribution, we observe a good agreement between data and backgrounds. In the same sign distribution, there is a difference due to the missing multijet background which is non-negligible for the same-sign spectrum. This is determined for the same-sign spectrum as the difference between data and the other backgrounds. Since the multijet is expected to be approximately invariant under flipping electric charges, we take twice the amount of the same-sign contribution for the total electron-muon channel. This is what is called multijet background in figure 5.3. We see in figure 5.3 that the contribution from the data-driven approach is in agreement with the W jets background from MC simulation and the multijet background determined via charge separation.

In figure 5.4 a distribution comparing the measured data with all standard model backgrounds stacked on top of each other is shown. Here, the event yield as a function of the pseudorapidity of the muon η^{muo} is plotted. Since these distributions, showing the event yield as a function of a kinematic variable, are very important in the following, we shortly focus on how they are obtained. To compare a certain amount of data with background and signal samples we have to weight each event of Monte-Carlo-produced background and signal samples according to

$$\omega = \frac{\mathcal{L} \cdot \sigma \cdot k_{weight}}{N_{ev}}.$$

In this equation \mathcal{L} denotes the integrated luminosity, σ the cross-section of the corresponding process. N_{ev} gives the number of events that were produced in the sample and k_{weight} denotes a weighting factor which takes corrections induced by higher orders into account. The values of the factors used for different processes can be found in table A.4. Additionally, each event is weighted according to the scale factors discussed in section 5.3 and pileup corrections described in section 5.4. Consequently one is able to compare background and signal processes with measured data. Figure 5.4 also introduces systematic errors, which are explained in detail in section 5.8. Another feature of figure 5.4 is that a comparison between

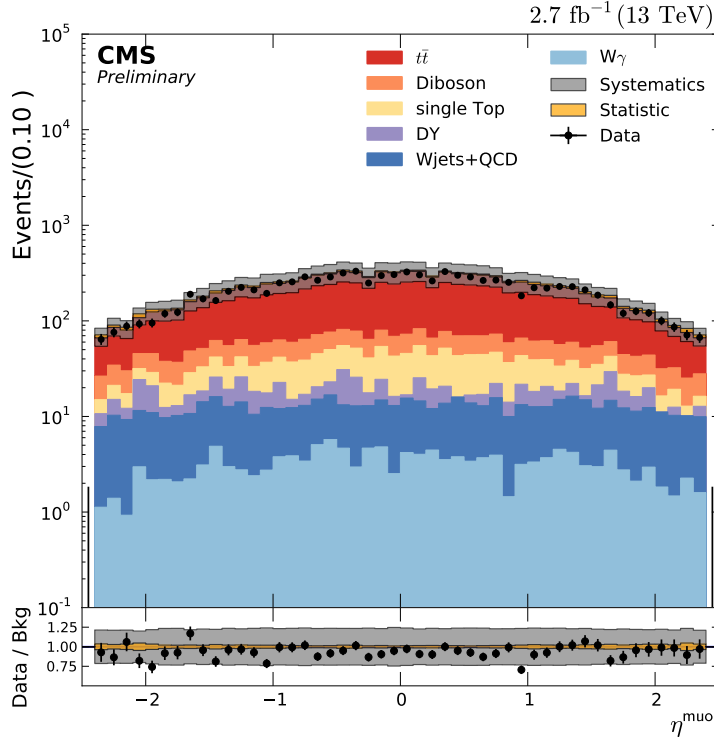


Figure 5.4: Distribution of the event yield as a function of the pseudorapidity of the muon η^{muo} . A comparison between data (black points) and background (coloured, filled and stacked histograms). Additionally, the grey and yellow bands denote the systematic and statistical uncertainties on the background event yield. The 'ratio plot' below presents the ratio of the data event yield over the background event yield for each bin. Again the uncertainties are presented by the coloured bands in order to directly read off significant differences between data and standard model expectation. The histogram is binned in η^{muo} .

data and complete background is shown. Together with the statistical and systematic uncertainties, one can directly observe if the distribution of data shows significant differences compared to the standard model background. Other distributions of kinematic variables of the selected muon as well as the selected electron can be found in section A.6.

5.7 Signal Models

The signal models are introduced in section 2.2 focusing on theoretical aspects and we know that they are produced by MC simulation (section 5.2). In this section we will discuss the signal efficiency of the different models. Another part of this section is concerned with the mass resolution of the resonant-like signal models (RPV-SUSY and Z'). Since the resonant-like signal models are treated differently in the statistical interpretation than the QBH models, the mass resolution is not determined in the QBH case. Both, the signal efficiency and the invariant mass resolution, play an important role in the statistical interpretation of the results.

5.7.1 Signal Efficiency

The signal efficiency³² is measured for all signal models. Figure 5.5 shows the signal effi-

³²In the following, 'acceptance times efficiency' ($A \times \epsilon$) will also be used as a synonym for signal efficiency.

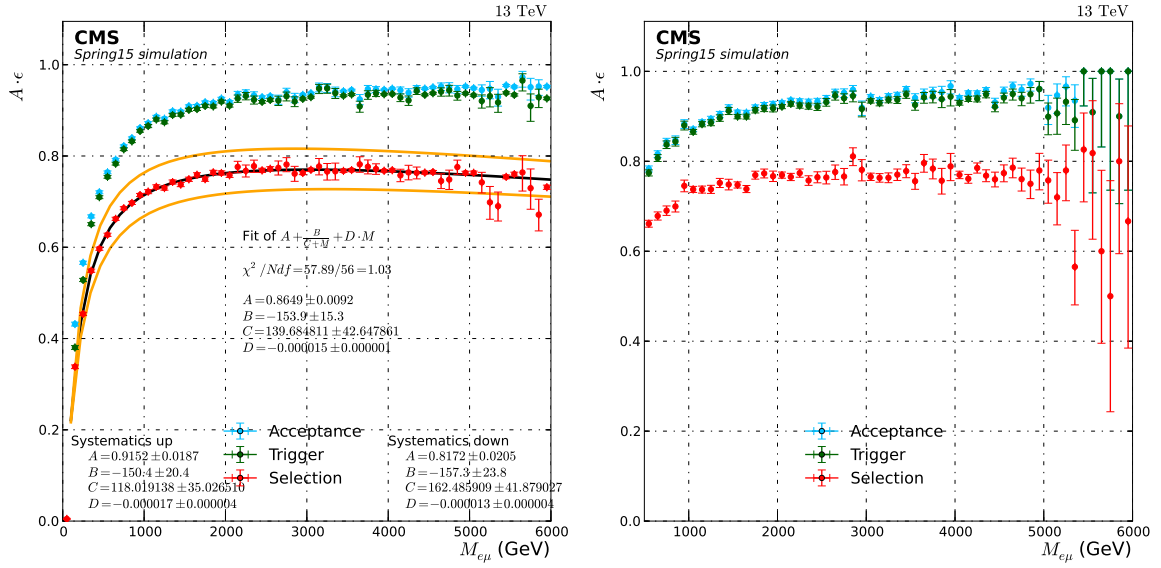


Figure 5.5: Signal efficiency of RPV-SUSY model (left) and QBH model (right). The efficiency of the Z' model is shown in figure A.7 since it is similar to the RPV-SUSY distribution. Different steps of the full event selection are also presented in different colours. In light blue, one can see the efficiency after acceptance criteria. The efficiency after trigger criteria is shown in green and after full selection, i.e. reconstruction and event selection criteria, in red. Additionally, for the RPV-SUSY models the solid lines represent a parametrization of the signal efficiency. The parametrization of the efficiency is shown in black. In blue and yellow, these are parametrization of the signal efficiency if one applies a variation (up/down) due to systematic uncertainties. This is further discussed in section 5.8.2. The quantity M in the parametrizations is given in GeV.

ciency determined with the RPV-SUSY model and the QBH models. The signal efficiency is defined as the efficiency after the full selection. That includes acceptance, trigger, reconstruction as well as event selection criteria. For RPV, we have a quite stable plateau of about 75 % above $M_{e\mu, \text{gen}} = 1.5$ TeV. Here the invariant $e\mu$ mass is the value at generator level, i.e. before reconstruction enters the game. For the QBH, one can see a stable plateau beginning at $M_{e\mu, \text{gen}} = 1$ TeV. For further modelling and statistical interpretation, a parametrization of the form

$$f_{\text{eff}}(M_{e\mu, \text{gen}}) = A + \frac{B}{C + M_{e\mu, \text{gen}}/\text{GeV}} + D \cdot M_{e\mu, \text{gen}}/\text{GeV} \quad (5.2)$$

is fitted to the RPV-SUSY model only since for the QBH models this is not necessary. The values of the parameters A , B , C and D are shown in figure 5.5. For the RPV-SUSY however the parametrization is important in order to interpret the results at arbitrary masses (section 7).

For the resonant-like signal models, the narrow width approximation holds. This allows to scale the cross section to arbitrary masses and coupling values. This parametrization of the signal efficiency is thanks to the NWA also used for different coupling values of λ_{132} and λ'_{311} . To check that the values of the couplings have no impact on the signal efficiency samples with different coupling values are produced.

5.7.2 Invariant Mass Resolution

The invariant mass resolution is defined by

$$\frac{M_{e\mu, \text{reco}} - M_{e\mu, \text{gen}}}{M_{e\mu, \text{gen}}} \quad (5.3)$$

on a per-event basis. Here the quantities $M_{e\mu,\text{gen}/\text{reco}}$ denote the invariant mass at generator level and after reconstruction, respectively. For each event, this quantity in equation 5.3 is collected in a histogram. An example at $M_{e\mu,\text{gen}} = 1.8$ TeV is shown in figure 5.6, where one can see that this distribution is centred around the origin and is relatively symmetric. The invariant mass resolution is determined with signal samples of the RPV-SUSY model. We now intend to extract the width of this distribution in order to get a measure of the mass resolution. Our method is simply to fit a Gaussian function to the core of the distribution and the resulting σ of the Gaussian is taken as the width. Since samples at different invariant masses are produced, one can proceed like this for every generated mass point. The resolution of each mass point is collected to obtain the red points in figure 5.7 in the end.

The invariant mass resolution is determined to be 2.5 % for $M_{e\mu,\text{gen}} = 1$ TeV and 4 % for $M_{e\mu,\text{gen}} = 4$ TeV. The deterioration of the resolution at high invariant masses is due to the muon measurement which suffers from the smaller bending of muons at high momenta. In addition, high-energetic muons induce showers in the iron yoke. The invariant mass resolution is used in the limit setting procedure described in section 7. That is the reason why a parametrization of the form

$$f_{\text{res}}(M_{e\mu,\text{gen}}) = A + B \cdot M_{e\mu,\text{gen}}/\text{GeV} + C \cdot (M_{e\mu,\text{gen}}/\text{GeV})^2 + D \cdot (M_{e\mu,\text{gen}}/\text{GeV})^3 \quad (5.4)$$

is used. The values of the individual parameters are listed in figure 5.7. Furthermore, the determination of the invariant mass resolution justifies the assumption made in section 2.2

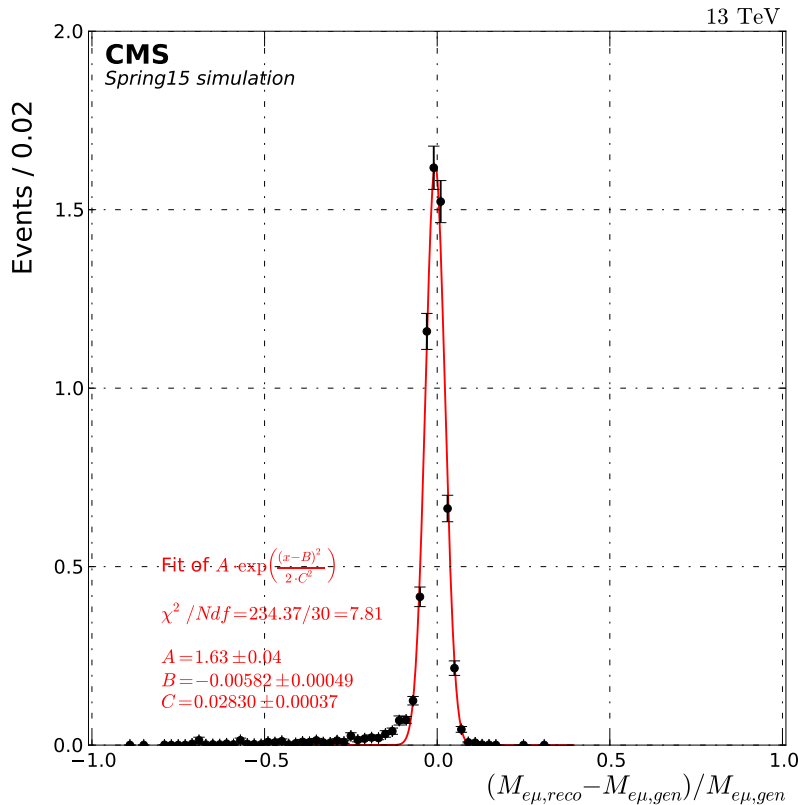


Figure 5.6: Gaussian fit of mass resolution for the signal mass point 1800 GeV. Studying the distribution more closely, one can observe a tail in the negative edge of the peak. The Gaussian fit is not respecting this feature. Thus, a Crystal ball function is tested and the resulting invariant mass resolution is shown in figure A.6. The difference compared to the Gaussian case is negligible. The Gaussian is used as a parametrization in this analysis since the parametrization is numerically more stable.

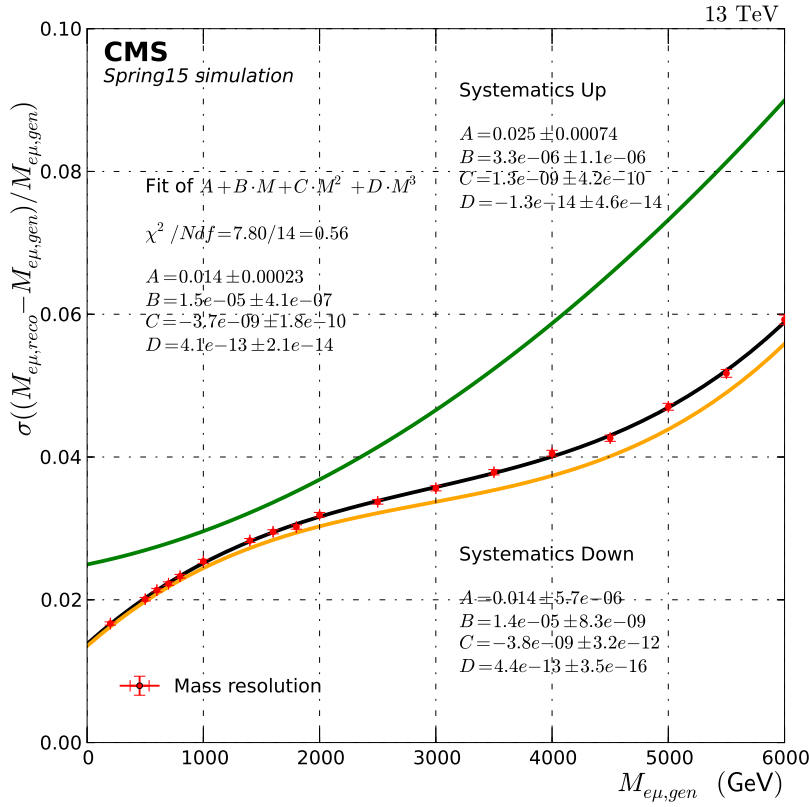


Figure 5.7: Relative invariant mass resolution of $e\mu$ pairs obtained from signal simulation. The systematic uncertainties are derived by propagating the effect of the systematic uncertainties described in section 5.8 towards the mass resolution. The quantity M in the parametrizations is given in GeV.

concerning the requirement of a resonant search for the RPV-SUSY models and the sequential standard model Z' .

5.8 Systematic Uncertainties

In every physical measurement one has to think about systematic effects that influence the measurement. In this section the systematic uncertainties affecting the invariant mass distribution are discussed. Systematic uncertainties may effect the shape or the normalization of the invariant mass distribution. We will later see that this distribution and its systematic uncertainties form the input for the statistical interpretation of the results and thus they are a decisive figure-of-merit. The systematic uncertainties of the standard model backgrounds are discussed as well as those for the different signal models.

5.8.1 Standard Model Background Systematic Uncertainties

There are two categories of background systematic uncertainties in this analysis. On the one hand, there are common systematic uncertainties for all measured physical processes. These are uncertainties concerning the measurement of the muon and the electron and other detector-specific uncertainties:

- Muon p_T scale: In order to determine the systematic uncertainty due to the muon momentum scale cosmic ray data are used [88]. Cosmic rays are measured since they provide muons with very high momenta of a few TeV in a sufficient amount compared

to data from collisions. The q/p_T (curvature) spectrum of the cosmic rays must go to zero for high transverse momenta. If the minimum of the spectrum is shifted from zero, one concludes that the reconstruction of high- p_T muons is not performing well enough. This is covered by introducing a bias on the curvature. The difference of the minimum from zero helps to quantify the bias. This procedure is called the 'endpoint method' and is more thoroughly described in [89]. For this analysis, a curvature bias $\kappa_b = 0.1/\text{TeV}$ is used to shift the transverse momentum of muons as follows

$$\frac{q}{p_T} \rightarrow \frac{q}{p_T} + \kappa_b. \quad (5.5)$$

The value of the curvature bias is taken from [90].

- Muon p_T resolution: The uncertainty arising due to the muon momentum resolution is also determined by a measurement with cosmic ray data [88]. Since the CMS detector is installed ~ 100 m underground the muons from cosmic rays prefer to traverse the detector vertically. In the determination of the momentum resolution only muon tracks close to the interaction point are taken into account. The method divides those tracks into an upper and a lower part. These parts are then reconstructed separately. The difference in momentum of the two tracks gives an estimate of the resolution. In this analysis the muon momentum resolution is handled by smearing the muon momentum in MC with a Gaussian. The width of the Gaussian is determined to be 4% [91].
- Muon scale factors: The scale factors for muon ID, isolation and trigger and the corresponding uncertainties are summarized in section 5.3.
- Electron p_T scale: The electron energy scale is varied by 0.4 % for electrons detected in the barrel region and 0.8 % for electrons in the endcaps. These values are determined by [87]. This analysis looks into the dielectron final state in 2015 CMS data. A comparison of data with simulation at the Z peak is performed in order to determine the scale uncertainties for barrel and endcap regions.
- Electron scale factors: The uncertainties of the scale factors for electron ID, isolation and trigger are introduced in section 5.3.
- Luminosity: The luminosity of the 2015 Run-II data-taking period is measured using the pixel cluster counting method. It can be determined with the instantaneous luminosity

$$\mathcal{L} = \frac{f \cdot \mu}{\sigma_0} = \frac{f \cdot \langle N_{\text{cluster}} \rangle}{\sigma_{\text{vis}}}, \quad (5.6)$$

where f is the revolution frequency of the beam, μ denotes the mean number of interactions, σ_0 represents the minimum bias cross section, $\langle N_{\text{cluster}} \rangle = \mu \cdot \langle N_{\text{cluster/interaction}} \rangle$ denotes the mean number of pixel clusters and $\sigma_{\text{vis}} \equiv \langle N_{\text{cluster/interaction}} \rangle \cdot \sigma_0$ is the visible inelastic cross section of proton-proton collisions. The visible cross section is determined using the Van-der-Meer scans. Within this method the overall uncertainty of the luminosity measurement is estimated to be 2.7 % [68].

- Pileup: The uncertainty due to pileup reweighting is estimated by shifting the minimum bias cross section by ± 5 %. Peculiarities of the procedure and a distribution showing the uncertainty can be found in section 5.4.

On the other hand, there are systematic uncertainties that are explicitly process-dependent:

- PDF and α_s : Since we are dealing with proton-proton collisions at the LHC which are not elementary particles we want to know the kinematics of the proton's constituents. Parton Distribution Functions (PDFs) give probabilities of how the momentum of the proton is distributed among its constituents. Since the PDFs are not calculable with a perturbative approach in theory, the experimental side steps in and helps to constrain the PDFs. There are uncertainties attached to PDFs. This PDF uncertainty together with a variation of the strong interaction constant α_s is taken into account and explained in the following. The procedure follows the recommendation for LHC Run-II physics by the PDF4LHC group [92]. The official PDF4LHC15_mc set with 100 different Monte Carlo replicas is used. For each of these replicas a cross section is determined which can vary. The amount of variation is propagated by taking the standard deviation of the cross section distribution. All those replicas are produced with a fixed $\alpha_s(M_Z^2) = 0.118$. One variation upwards ($\alpha_s(M_Z^2) = 0.1195$) and one downwards ($\alpha_s(M_Z^2) = 0.1165$) take the uncertainty in α_s into account. Both uncertainties are added in quadrature and result in a relative influence on the background event yield shown in figure 5.8.
- Cross sections: There is a systematic uncertainty assigned to the process-dependent cross section. For $t\bar{t}$, single top, Drell-Yan, WZ and ZZ a 5 % uncertainty is used and for WW a 4 % uncertainty is used [93]. For the $W\gamma$ background we assign a systematic uncertainty of 50 % since Monte-Carlo simulation is used when it comes to peculiarities like photon-to-electron misidentification rate or photon conversion.

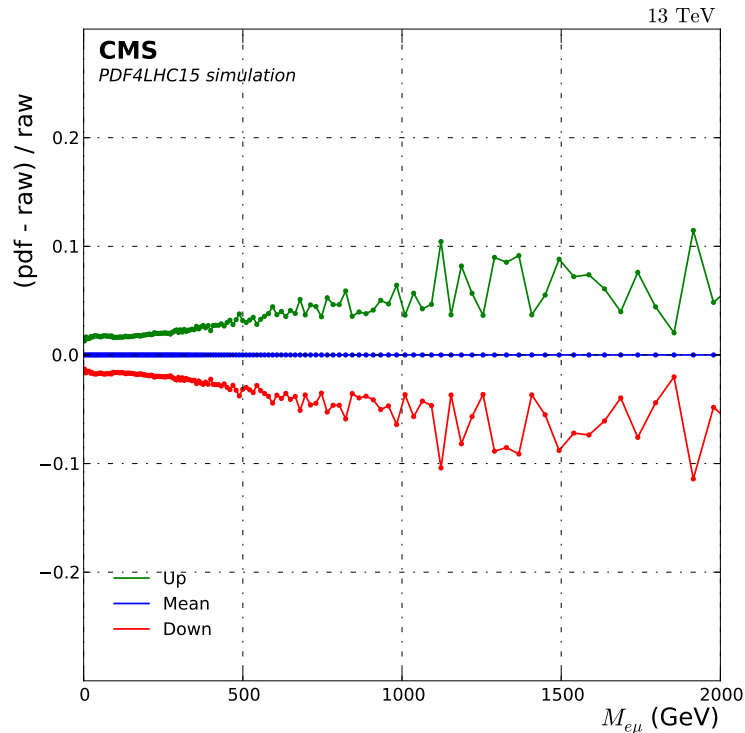


Figure 5.8: Relative uncertainty of the background event yield due to PDF + α_s variations as a function of the invariant electron-muon mass $M_{e\mu}$. Shown is the relative difference between the weighted sample, called 'pdf', and the unweighted sample, called 'raw'. One can see the 'up', 'down' and 'mean' distribution. The 'mean' distribution should be constantly 0 since the background samples are already produced with a NNLO PDF set.

- ‘Wjets + QCD’: A data-driven approach is used to determine the Wjets+QCD background. Due to the lack of precision in the functional form of the ‘fake rate’, we apply a systematic uncertainty of 50 % [87].
- ‘Top Envelope’: This is an uncertainty determined as the envelope of two separately determined uncertainties, both concerned with the shape of the $t\bar{t}$ background. Since we know that this background is dominant for a wide invariant mass range, this systematic deserves some consideration. One part of this shape uncertainty is estimated considering differential distributions of resummed cross sections at NLO+NNLO for the invariant $t\bar{t}$ mass $M_{t\bar{t}}$ [94]. These corrections are added linearly for each event according to its invariant $t\bar{t}$ mass. The functional form of the event weight is given by

$$\text{weight} = \begin{cases} 1 \pm \left(0.05 \cdot \frac{M_{t\bar{t}} - 2m_t}{0.5 \text{ TeV} - 2m_t} \right) & 2m_t < M_{t\bar{t}} < 0.5 \text{ TeV} \\ 1 \pm \left(0.05 + 0.25 \cdot \frac{M_{t\bar{t}} - 0.5 \text{ TeV}}{1.0 \text{ TeV} - 0.5 \text{ TeV}} \right) & 0.5 \text{ TeV} < M_{t\bar{t}} < 1 \text{ TeV} \\ 1 \pm \left(0.3 + 0.3 \cdot \frac{M_{t\bar{t}} - 1.0 \text{ TeV}}{1 \text{ TeV}} \right) & 1 \text{ TeV} < M_{t\bar{t}} < 3 \text{ TeV}, \end{cases} \quad (5.7)$$

where m_t is the mass of the top quark. This functional form is also visualized in figure 5.9. The other part of this uncertainty is estimated by varying QCD renormaliza-

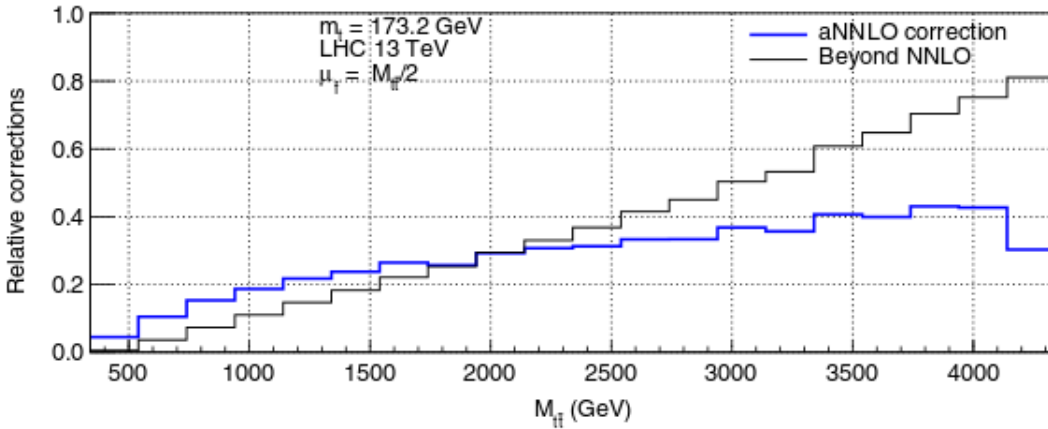


Figure 5.9: Relative corrections at approximate NNLO and beyond as a function of the invariant $t\bar{t}$ mass. [94]

tion and factorization scales. This variation reflects similar to the corrections coming from the resummed cross section the limited knowledge of higher order processes contributing to the $t\bar{t}$ background. For the up variation of the scales a factor 2 and for the down variation a factor $\frac{1}{2}$ is applied. The weighting factor is taken from MC simulation and the maximum of up/down is used. These two uncertainties contribute to the ‘Top Envelope’ systematic uncertainty. A comparison over the invariant mass range is presented in figure 5.10.

An overview over all systematic uncertainties together with the statistical uncertainty is given in figure 5.11 as a function of the invariant mass $M_{e\mu}$. For low invariant masses, the dominant systematic uncertainty is the ‘Top Envelope’ uncertainty of maximal 25 % which then decreases due to the decreasing $t\bar{t}$ background. At invariant masses $> 1.5 \text{ TeV}$ the muon p_T scale becomes equally important as the ‘Top Envelope’. The systematic uncertainties go into the statistical interpretation in section 7.

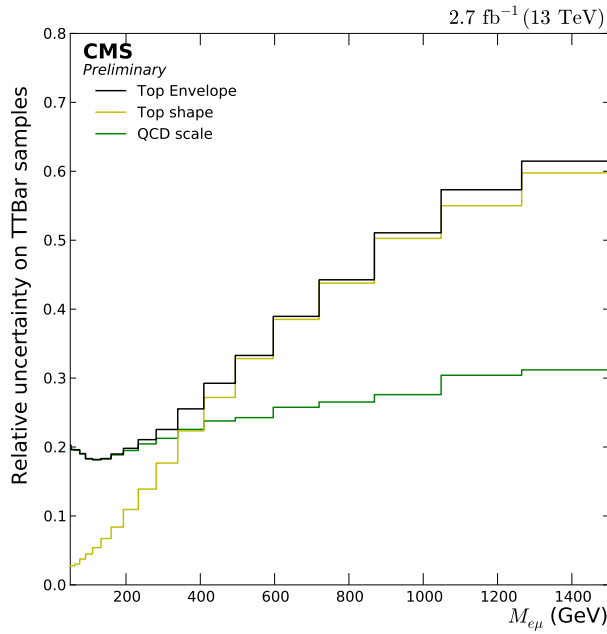


Figure 5.10: Relative systematic uncertainty on the event yield of the $t\bar{t}$ background as a function of $M_{e\mu}$ due to the top shape uncertainty. Both contributions are shown together with their envelope which is used in this analysis. For lower masses the systematic uncertainties from QCD scale variations dominate. For higher masses the envelope is mainly driven by the corrections from the resummed cross section calculation.

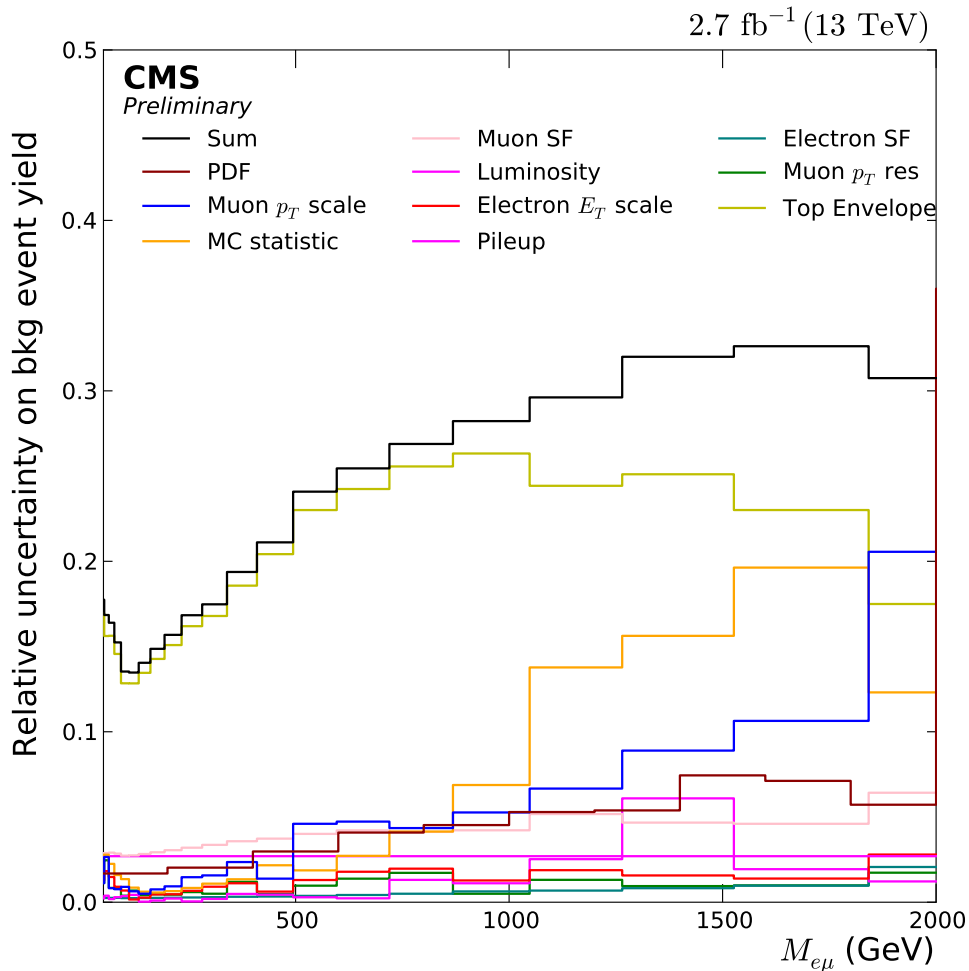


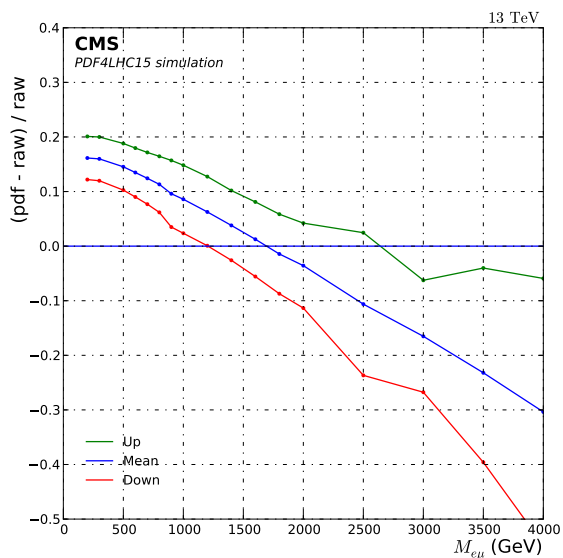
Figure 5.11: Relative uncertainty on the background event yield as a function of the invariant electron-muon mass $M_{e\mu}$. The systematic uncertainties that are mentioned in this section are shown as well as the statistical uncertainty on the background event yield. The 'Top Envelope' uncertainty is dominating for a large range of the invariant $e\mu$ mass spectrum.

5.8.2 Systematic Uncertainties of Resonant-like Models

The systematic uncertainties of the resonant-like (RPV-SUSY/ Z') samples are treated differently than those of the background. Basically, the same systematic uncertainties for the physical objects are considered. The difference in this case is that the mass resolution distribution is used to evaluate the impact of the systematic uncertainties. This is done since we intend to use arbitrary mass points for the statistical interpretation. Additionally, the uncertainties on $A \times \epsilon$ are taken into account. The uncertainties on the luminosity is also included for the resonant-like signal models.

- **Mass resolution:** The systematic uncertainty of the mass resolution is taken into account. Figure 5.7 includes the mass-dependency of the systematic uncertainty on the mass resolution. This is partially due to the muon part of the invariant mass where at high transverse momenta of the muon the reconstruction starts struggling with showering effects in the iron yoke of the muon chambers. For the statistical interpretation it is useful to know that this systematic uncertainty results in a change of the shape of the invariant mass distribution but does not affect the normalization. With the mass resolution uncertainty all systematic uncertainties of the object reconstruction (muon p_T scale/resolution, electron scale/resolution, scale factors) should be covered.
- **$A \times \epsilon$:** For the product $A \times \epsilon$ which is shown in figure 5.5 a systematic uncertainty is calculated as follows. A similar propagation of systematic errors is done as in the mass resolution. The acceptance times efficiency is determined with one σ variations due to the systematic uncertainties of the physical objects (muon p_T scale/resolution, electron scale/resolution, scale factors) separately. The deviations for each systematic are summed quadratically and the resulting up/down variation (yellow line in figure 5.5) is taken as the systematic uncertainty on $A \times \epsilon$ for the resonant-like signal models. Since this uncertainty should cover the PDF uncertainty on the signal samples as well, we set the uncertainty to 10 %. Figure 5.12 shows the PDF uncertainty for the RPV-SUSY model as a function of the generated invariant $e\mu$ mass. One can see that the uncertainty is $< 10\%$ for a wide mass window ³³.

Figure 5.12: Relative uncertainty of the RPV signal event yield due to PDF + α_s variations as a function of the generated invariant electron-muon mass $M_{e\mu}$. Shown is the relative difference between the weighted sample, called 'pdf', and the unweighted sample, called 'raw'. One can see the 'up', 'down' and 'mean' distribution. The 'mean' distribution is decreasing since the signal samples are produced at LO whereas the PDF uncertainty calculation expects NLO samples. In other words, the offset of the 'mean' distribution corresponds to a NLO k-factor, which is already taken into account for RPV-SUSY models.



³³The reason for this handling of the PDF uncertainties is due to the fact that this analysis is also an analysis of the CMS collaboration, where it is needed to be aligned with other analyses [87; 91]. This applies also to the PDF uncertainty in the QBH case.

- Luminosity: Here the same value of 2.7 % is used as in the background systematic uncertainties.

5.8.3 Systematic Uncertainties of QBH models

For the QBH samples, the systematic uncertainties are treated almost completely analogously to the background procedure. The systematic uncertainties corresponding to the physical objects, like the muon scale and resolution, the electron scale and resolution as well as the systematic uncertainties coming from the scale factors are handled the same way as in the background case described in section 5.8.1. Again a systematic uncertainty of 2.7 % on the integrated luminosity is applied. The systematic uncertainty on $A \times \epsilon$ is set to 10 %. This is a conservative value since it is supposed to cover the PDF uncertainties as well. The procedure of determining the systematic uncertainties differs from the RPV-SUSY and Z' systematic uncertainties due to the non-resonant shape of the QBH signal.

6 Results of Analysis in Electron-Muon Channel

In the following, the invariant mass distribution of the analysis (section 5) in the electron-muon channel at a centre-of-mass energy of 13 TeV with data taken in 2015 with the CMS detector are presented and discussed. This distribution is the starting point for the statistical interpretation discussed in section 7.

6.1 Invariant Mass Distribution

After full selection the invariant $e\mu$ mass distribution is obtained and can be seen in figure 6.1. All distributions in this section are binned in a manner that the bin contents are normalized by the bin width. In order to get the total expectation of the standard model backgrounds the distributions of different processes are stacked. Together with the standard model background an example of a RPV-SUSY model and an example of a QBH model are overlaid. The grey and yellow bands denote the systematic and statistical uncertainties on the background event yield, respectively. The origin and determination of the systematic uncertainties is the topic of section 5.8. The binning of the x -axis in figure 6.1 follows the

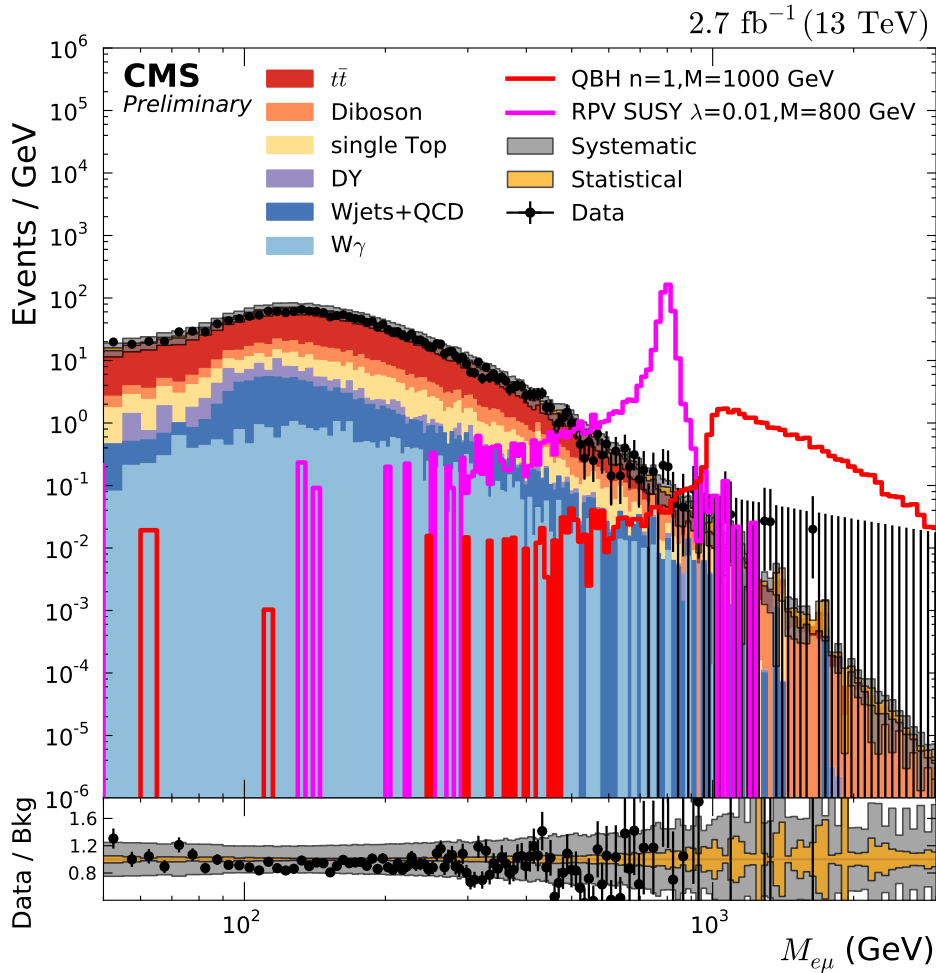


Figure 6.1: Invariant mass distribution: Event yield of data, standard model background and two signal examples shown as a function of the invariant $e\mu$ mass. Systematic and statistical uncertainties are presented as grey and yellow bands. The binning of the x -axis follows the estimated invariant mass resolution. For this variable binning, each bin content is normalized to its respective bin width.

estimated invariant mass resolution. In figure 6.2 one can see a rebinned version of the invariant mass distribution. There, the binning corresponds to a logarithmic function. In both ways of presenting the invariant mass distribution, the measured data and the expected SM background are in agreement within the uncertainties. Table 6.1 presents the composition of the standard model background expectation for different mass ranges. In figure 6.3 the

Process	$100 < \frac{M_{e\mu}}{\text{GeV}} < 200$	$200 < \frac{M_{e\mu}}{\text{GeV}} < 600$	$600 < \frac{M_{e\mu}}{\text{GeV}} < 1000$	$1000 < \frac{M_{e\mu}}{\text{GeV}} < 2000$	$2000 < \frac{M_{e\mu}}{\text{GeV}}$
single top	7 %	9 %	9 %	17 %	-
Drell-Yan	3 %	1 %	-	-	-
$W\gamma$	1 %	2 %	2 %	-	-
'Wjets + QCD'	13 %	9 %	18 %	15 %	-
WZ	1 %	2 %	4 %	5 %	-
ZZ	< 1 %	< 1 %	< 1 %	< 1 %	7 %
WW	8 %	7 %	13 %	27 %	71 %
$t\bar{t}$	67 %	71 %	51 %	37 %	22 %
Total Bkg	6077 ± 912	2823 ± 508	54 ± 14	4.1 ± 1.1	0.028 ± 0.013
Data	5285	2699	44	6	0

Table 6.1: Composition of the standard model background expectation. For the total background event yield the uncertainty is given as the quadratic sum of the statistical and systematic uncertainty.

cumulative version of the invariant mass distribution is shown. Here one can clearly see the three highest invariant mass events at around 1.6 TeV and 1.3 TeV. More information about the highest invariant mass events can be found in the appendix in table A.6. For the highest selected invariant $e\mu$ mass, figures 6.4 and 6.5 show the event display. Summing up over the total mass range of this search (looking at the first bin in figure 6.3) the SM background expectation predicts more events than measured in total. This might be due to the $t\bar{t}$ background and the disagreement is covered by the $t\bar{t}$ shape uncertainty. Consequently, all resulting distributions in the invariant mass suggest the same conclusion. The measured data show no significant disagreement with the standard model expectation. For the statistical interpretation of the results exclusion limits are set on the cross section times branching ratio of the studied models (RPV-SUSY, QBH and Z'). The goal is to exclude certain regimes of the parameter space of the different models. What is meant by this statement is discussed in detail in section 7.

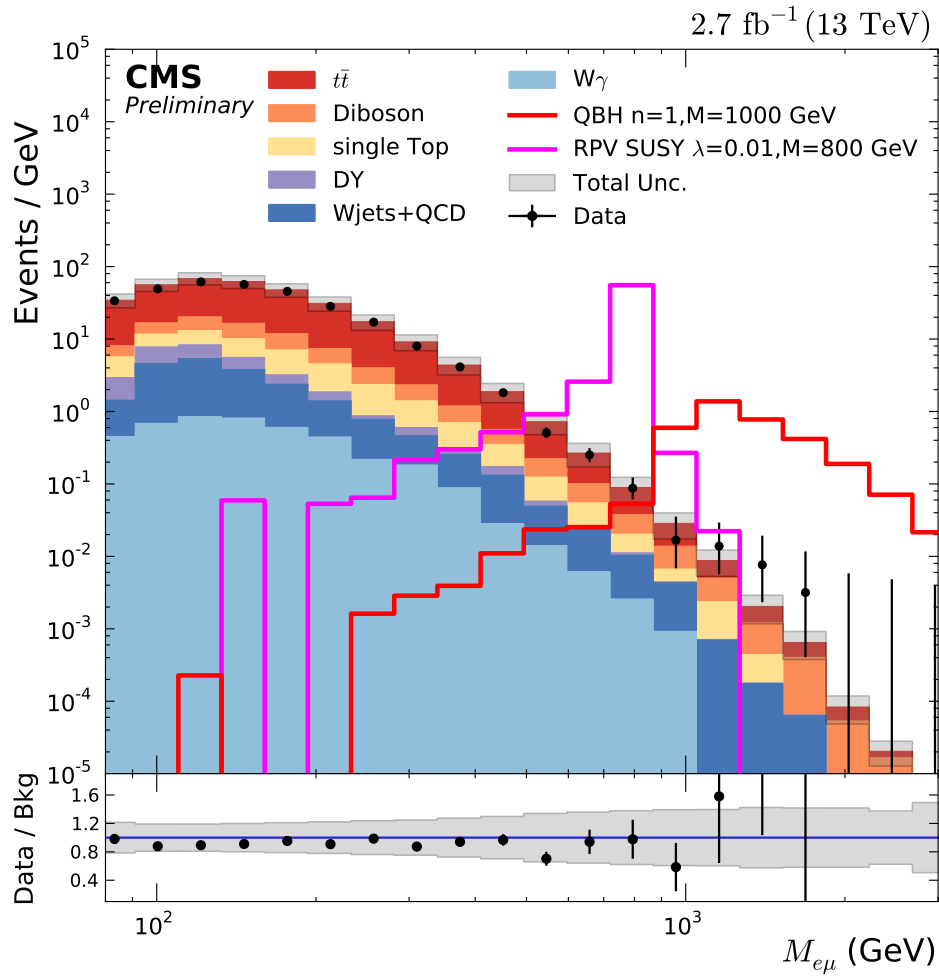


Figure 6.2: Invariant mass distribution with a coarse binning. The binning corresponds to logarithmic function. The systematic and statistical uncertainties are added quadratically and are represented by the light-greyish band.

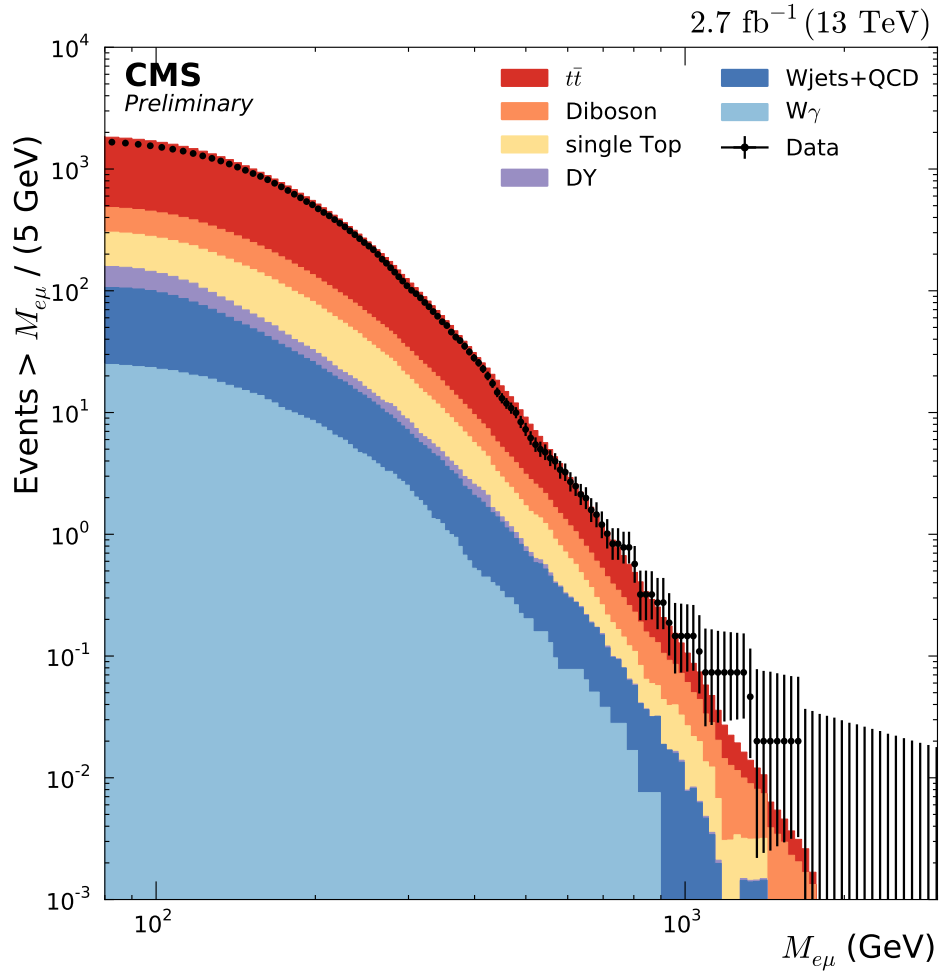


Figure 6.3: Invariant mass distribution in a cumulative way. In this distribution a constant binning of 5 GeV is used. The cumulative way represents the fact that each bin of this distribution shows the integral of the event yield above this minimal value.

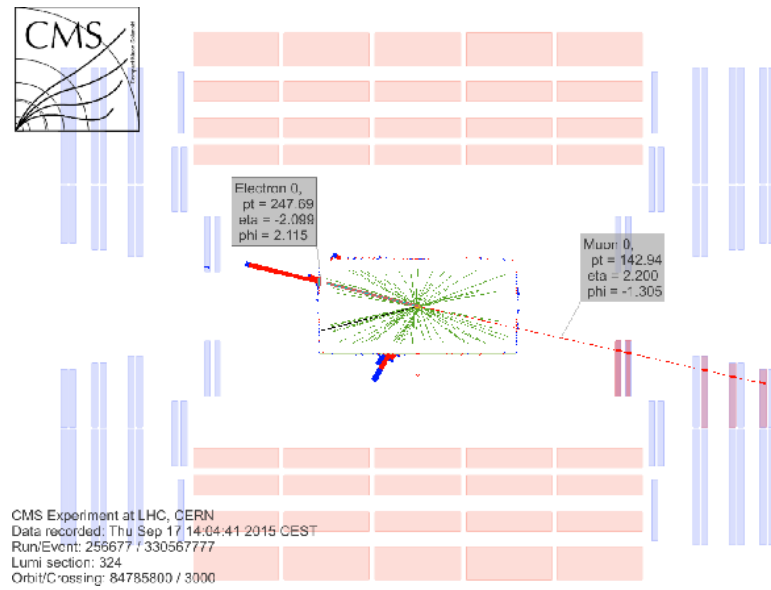


Figure 6.4: Event display of the highest invariant mass event ($M_{e\mu} = 1.6$ TeV) in 2015 CMS data at 13 TeV in the rz -plane. Both objects are very forward in the detector.

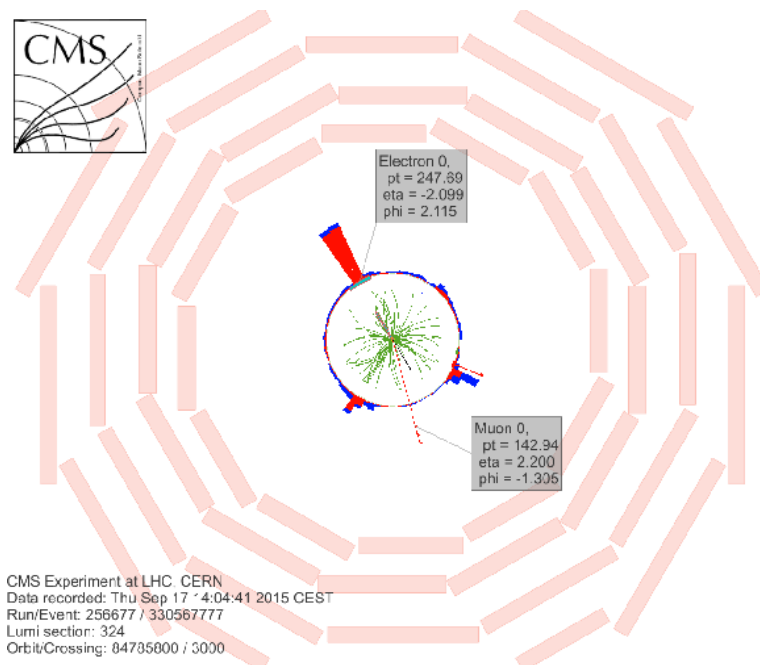


Figure 6.5: Event display of the highest invariant mass event ($M_{e\mu} = 1.6$ TeV) in 2015 CMS data at 13 TeV in the $r\phi$ -plane. The electron and the muon are not exactly back-to-back.

7 Statistical Interpretation

This section is concerned with the statistical interpretation of the results described in section 6. The interpretation is done by studying RPV-SUSY, QBH and SSM Z' models and setting exclusion limits within the different models. The first section is devoted to explain the basics of the limit setting strategy and define the relevant terms and introduce the procedure. After that, the reader should be able to comprehend the section which deals with the exclusion limits obtained for the different BSM physics.

7.1 Limit Setting

This section presents the basics of the limit setting used in this analysis. The explanation of the procedure is based on reference [95]³⁴. The idea of limit setting is to exclude a certain region in the parameter space of the models predicting new physics by making use of the agreement of standard model background with the measured data. The starting point of the limit setting is the so-called Bayesian approach, which is derived from the more fundamental Bayes' theorem saying

$$P(A|B) = \frac{P(B|A) \cdot P(A)}{P(B)}. \quad (7.1)$$

This is a statement about the conditional probability $P(A|B)$, i.e. the probability that A is happening given B . $P(A)$ denotes the probability that A is happening³⁵. However, Bayes' theorem can be reinterpreted by defining more specifically what is meant by the 'probability'. In the context of Bayesian (also called subjective) probability one reinterprets the probability $P(A)$ as the degree of belief that A is true. Using this interpretation, one can write the Bayesian approach as

$$P(\text{theory}|\text{data}) \propto P(\text{data}|\text{theory}) \cdot P(\text{theory}). \quad (7.2)$$

Here the $P(\text{theory})$ represents the prior probability that a given theory is true. $P(\text{data}|\text{theory})$ is called likelihood (L), which denotes the probability to observe the data that was measured under the assumption of the theory. $P(\text{theory}|\text{data})$ is called posterior probability and represents the probability that the theory is correct after seeing the experimental outcome. The proportionality in equation (7.2) can be turned into an equality by correct normalization to unity. The posterior probability is exactly what we want to determine. In the end, the posterior probability is used to derive limits.

The expression in equation (7.2) needs to be filled with decisive quantities describing the 'theory' and 'data'. The theory under investigation is represented by the number of expected signal events s if the theory is true. In words of data analysis this is the parameter of interest (POI). Furthermore the measured data are expressed in terms of the number of observed events N_{obs} . With this input one can rewrite equation (7.2) into

$$P(s|N_{obs}) = \frac{L(N_{obs}|s) \cdot \pi(s)}{\int L(N_{obs}|s') \cdot \pi(s') ds'}. \quad (7.3)$$

The denominator is here the normalization of the probabilities. A new function $\pi(s)$ denoting the prior probability is introduced here and explained in the following. The prior probability of the theory can be written as

$$\pi(s) = \begin{cases} 0 & , s < 0 \\ 1 & , s \geq 0 \end{cases}. \quad (7.4)$$

³⁴An introduction of fundamental concepts of statistical data analysis is also given in reference [95]. In this thesis, this knowledge is presupposed.

³⁵We will not go into detail of the set-theoretical concepts of probabilities.

This is called a flat prior for obvious reasons. The reader may have the impression that this choice of the prior probability is rather arbitrary. To some extent this is true since, in Bayesian statistics, there is no fundamental rule to assign a prior probability to a theory. However, this choice of the prior probability can be justified by the following arguments. A priori the number of signal events is expected to be $s \geq 0$ and every non-negative number of signal events should have the same probability due to a lack of further knowledge. It is worth mentioning that this simple approach of a flat prior brings along some conceptual drawbacks. One is that the upper limit is not invariant under non-linear transformations of the parameter of interest. For example, if you take the parameter of interest to be $a(s) = s^2$ and still use a flat prior, it will change the outcome [95]. Consequently, one should always be careful when comparing results of different analyses.

After discussing the prior function, one has to specify the functional form of the likelihood distribution $L(N_{obs}|s)$. This probability is distributed as a Poisson variable

$$L(N_{obs}|s) = \frac{(s+b)^{N_{obs}}}{N_{obs}!} \exp(-(s+b)). \quad (7.5)$$

The variable b represents the expected number of background events. In order to obtain an upper limit on the parameter of interest, an integration over the probability in equation (7.3) is performed setting the integral to 0.95

$$0.95 = \int_{-\infty}^{s_{up}} P(s|N_{obs}). \quad (7.6)$$

This equation determines s_{up} , the upper limit at 95 % confidence level. This value can be translated into an upper limit of a production cross section in the context of a signal model.

So far, we have not discussed the influence of (systematic) uncertainties on the limit setting. The statistical uncertainty is taken care of by the Poisson probability. To model the systematic uncertainties, the concept of nuisance parameters $\nu = (\nu_1, \dots, \nu_n)$ is used. There are two different types of systematic uncertainties in this limit setting procedure. One category consists of multiplicative uncertainties (e.g. luminosity) and the other category consists of shape uncertainties (e.g. muon momentum scale) resulting in an overall distortion in the shape of the observed spectrum. The following description of the handling of systematic uncertainties is based on reference [96].

The multiplicative corrections are modelled by introducing an additional prior probability $\pi(\alpha)$ in equation (7.3) for each nuisance parameter α . The choice is a log-normal distribution

$$P(x; \mu_\alpha, \sigma_\alpha) = \frac{1}{x\sigma_\alpha\sqrt{2\pi}} \exp\left[-\frac{(\ln x - \mu_\alpha)^2}{2\sigma_\alpha^2}\right], \quad (7.7)$$

where μ_α denotes the mean value of the nuisance parameter α and σ_α the corresponding uncertainty. The choice of a log-normal distribution is motivated by the fact that the multiplicative nuisance parameters represent physical quantities that should remain positive (e.g. luminosity or cross sections). That physical constraint is ensured by the logarithmic term in the exponent. However, there are other distributions for non-negative quantities. This is why one has to state that there are other properties of the log-normal distribution that justifies the choice. For example, a product of log-normal distributions is still a log-normal distribution.

For the shape uncertainties the central value β^0 of the number of expected events together with its up-variation β^+ and down-variation β^- is known. Consequently, we have three measures of the shape. The question is how to interpolate between those variations to obtain a continuous estimate. This is solved by introducing a 'morphing' parameter, f ,

which is distributed Gaussian-like with a mean value of $\mu_f = 0$ and an uncertainty of $\sigma_f = 1$. The value of β is interpolated quadratically for $|f| < 1$ and linearly out of this range:

$$\beta(f) = \begin{cases} \frac{f(f-1)}{2}\beta^- - (f-1)(f+1)\beta^0 + \frac{f(f+1)}{2}\beta^+ & , |f| < 1 \\ \beta^0 + f\frac{\beta^+ - \beta^-}{2} & , \text{else} \end{cases}. \quad (7.8)$$

The number of signal and background events is then replaced by $\beta(f)$ and the prior probability is a Gaussian with a mean of $\mu = 1$ and a width of $\sigma = 1$. This method of ‘morphing’ can be extended to several morphing parameters taking care of several systematic effects by adding linearly the deviations from the nominal value.

The dependence on the nuisance parameters (multiplicative and shape uncertainties) is eliminated by integrating them out in the posterior probability

$$P(s|N_{obs}) = \int P(s, \nu|N_{obs}) d\nu. \quad (7.9)$$

This integration is analytically not solvable due to its high number of dimensions (= number of systematic uncertainties) and therefore the Markov Chain Monte Carlo (MCMC) method is used [97].

Another peculiarity of limit setting is how we prepare the ‘input’ distributions. In this analysis a so-called multi-bin limit is calculated. This takes information about the shape of the signal and background distribution into account. The strategy, which is described above, works for one bin. Fortunately, the strategy can be easily generalized. In the multi-bin limit setting, multiplying the different probabilities of each bin results in a new definition of the upper limit

$$0.95 = \int_{-\infty}^{s_{up}} \prod_{i \in \text{bins}} P_i(s|N_{obs}). \quad (7.10)$$

The procedure that is described above gives observed limits since the measured data go into the calculation as the number of observed events. However it might also be interesting to look at the so-called expected limits and a comparison between expected and observed. In the context of the expected limit setting the number of observed events N_{obs} is replaced by a diced number of events based on the background estimation. Also the systematic uncertainties are diced according to their uncertainties. With the new input freshly diced every time the limit setting is performed over and over again, so that one can extract a median expected limit and the corresponding one (68 %) and two (95 %) sigma bands can be calculated. Assuming no deviation of the data from the standard model expectation, one expects the observed and expected limit to be overlaying within the uncertainty bands.

Regarding the implementation side of the limit calculation, the so-called Higgs Combine tool [98] is used, which is based on RooStats [99].

7.2 Exclusion Limits

In this section the focus lies on the limit setting in the context of the different signal models, namely RPV-SUSY, QBHs and SSM Z' . In general $\sigma \times BR$ (‘cross section times branching ratio’) is shown together with the theoretical cross section of the different models as a function of an important parameter, i.e. mass (thresholds) or couplings. The intersection point of the observed limit and the theoretical line gives the lower limit of this parameter. Above that intersection, one cannot exclude the given model.

7.2.1 RPV-SUSY Limits

Figure 7.1 shows the expected and observed limit of the product $\sigma_{prod} \cdot BR(\tilde{\nu}_\tau \rightarrow e\mu)$ for the RPV τ sneutrino as a function of the mass $M_{\tilde{\nu}_\tau}$. Different values of the couplings $\lambda_{132} = \lambda_{231}$ and λ'_{311} as mentioned in section 2.2.1 are considered here. Additionally the theoretical cross sections are represented by the solid coloured lines. For the couplings $\lambda_{132} = \lambda_{231} = \lambda'_{311} = 0.01$ a lower mass limit of 1.0 TeV is obtained. For $\lambda_{132} = \lambda_{231} = \lambda'_{311} = 0.1$ a mass limit of 2.7 TeV is set.

The limits on the RPV-SUSY models are obtained by using the distributions of the invariant mass resolution (figure 5.7) and $A \times \epsilon$ (figure 5.5). For a given mass point, a Gaussian is used with the mean of the tau sneutrino mass and the width taken from the invariant mass resolution. This Gaussian is scaled by the given luminosity and $A \times \epsilon$. According to this probability density function, values are diced and filled in a histogram with the same binning as the background distribution of the invariant $e\mu$ mass. The histogram is filled within the range of $\pm 8\sigma$ around the mean value and serves as an input histogram for the limit setting. This is done analogously for the Z' limit setting discussed in section 7.2.2.

Resonant-like models, like the RPV-SUSY models, are defined by the requirement that for the width $\Gamma_{\tilde{\nu}_\tau}$ the relation

$$\frac{\Gamma_{\tilde{\nu}_\tau}}{M_{\tilde{\nu}_\tau}} \ll \frac{\sigma(M_{e\mu})}{M_{e\mu}} \quad (7.11)$$

holds, i.e. the relative width is much smaller than the detector resolution in the electron-muon channel. This feature is also discussed in section 2.2 and 5.7.2. The observed exclu-

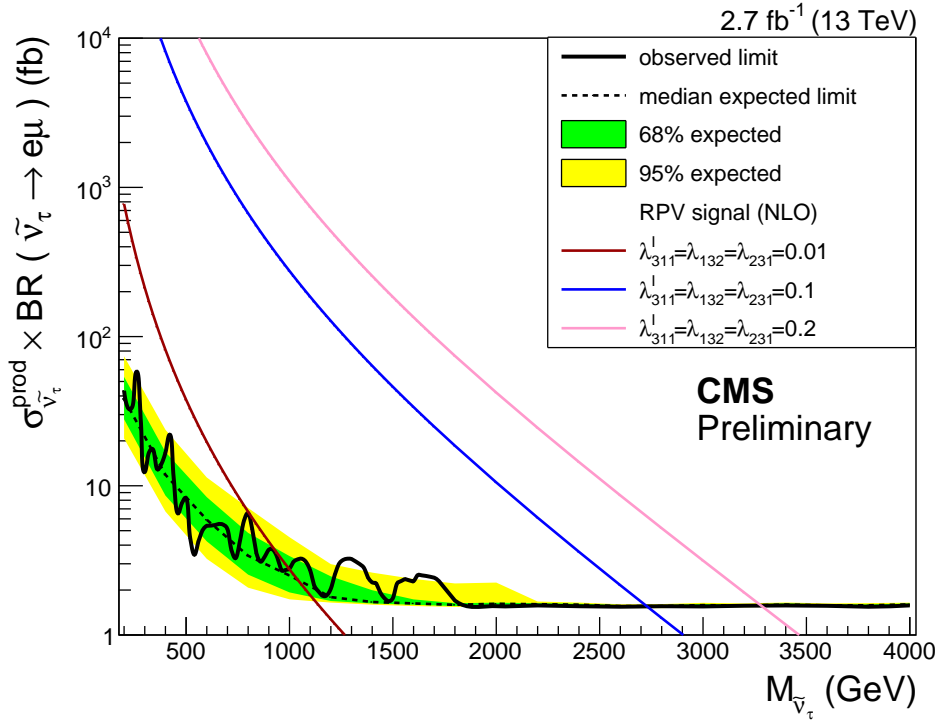


Figure 7.1: Expected and observed cross section limit in the $e\mu$ channel in the context of the RPV-SUSY models. The expected and observed limit are shown here as the dashed black and solid black line, respectively. The limits are obtained as discussed in section 7. The green and yellow band stand for the 68 % and 95 % uncertainty bands of the expected limit. The coloured solid lines represent the theoretical cross sections of the models with different coupling parameters. The excess of observed limit with respect to expected limit at 1.6 TeV is due to the highest invariant mass event.

sion limits on $\sigma \times BR$ in figure 7.1 are valid for any model as long as the shape of the signal is resonant-like and the signal efficiency stays the same as in the RPV case. The shape and efficiency condition are fulfilled in the parameter space that is studied in this analysis. This is why one can also set limits on the parameter space of the RPV-SUSY models that is not explicitly simulated by MC generators. These limits are shown in figure 7.2. This limit contour is obtained starting from the cross section formula in the narrow width approximation given in section 2.2.1

$$\sigma \times BR(\tilde{\nu}_\tau \rightarrow e^\pm \mu^\mp) = k(M_{\tilde{\nu}_\tau}) \cdot \frac{(\lambda'_{311})^2 \left((\lambda_{132}^{\text{fix}})^2 + (\lambda_{231}^{\text{fix}})^2 \right)}{3 (\lambda'_{311})^2 + \left((\lambda_{132}^{\text{fix}})^2 + (\lambda_{231}^{\text{fix}})^2 \right)}, \quad (7.12)$$

where the value of the λ_{132} is fixed. In order to obtain a limit on the other coupling parameter λ'_{311} one rearranges the equation until one gets

$$\lambda'_{311}{}^{\text{limit}} \left(M_{\tilde{\nu}_\tau}, \left(\lambda_{132}^{\text{fix}} \right)^2 + \left(\lambda_{231}^{\text{fix}} \right)^2 \right) = \sqrt{\frac{\left((\lambda_{132}^{\text{fix}})^2 + (\lambda_{231}^{\text{fix}})^2 \right)}{\frac{k(M_{\tilde{\nu}_\tau})}{(\sigma \times BR)_{\text{obs}}^{\text{excl}}(M_{\tilde{\nu}_\tau})} \cdot \left((\lambda_{132}^{\text{fix}})^2 + (\lambda_{231}^{\text{fix}})^2 \right) - 3}}}. \quad (7.13)$$

With the argument above, that the RPV-SUSY models studied here are 'resonant-like' one can plug in the $(\sigma \times BR)_{\text{obs}}^{\text{excl}}$ of the observed limit. Looking at equation (7.13), we have found

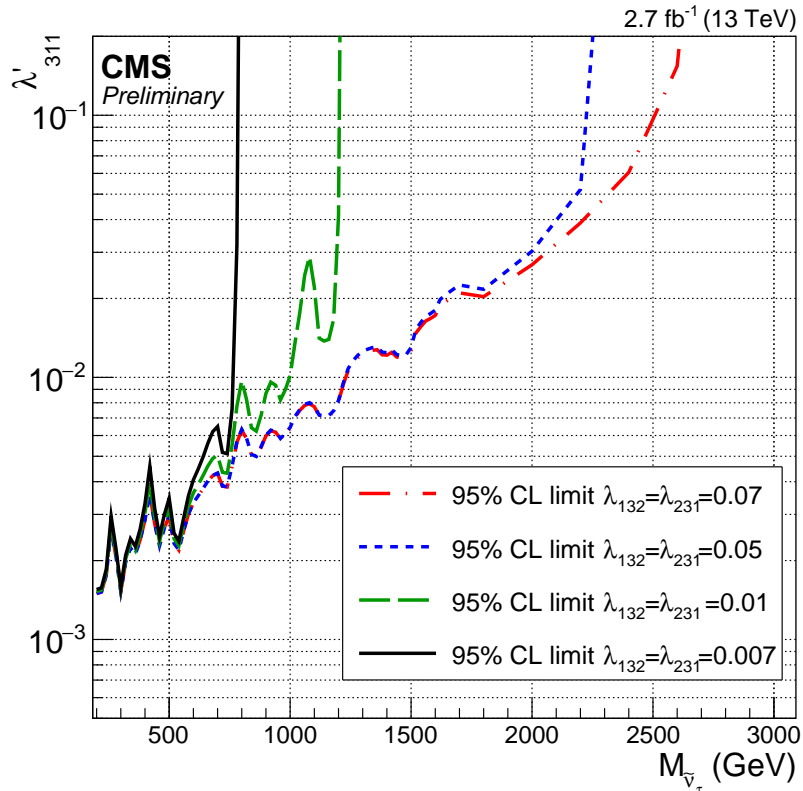


Figure 7.2: Expected limit contour at 95 % confidence level for the RPV signal in the $M_{\tilde{\nu}_\tau} - \lambda'_{311}$ parameter space. The values of the other coupling λ_{132} are fixed to 0.07, 0.05, 0.01, 0.007. The area above the lines is excluded for each fixed coupling λ_{132} . The lines are determined with the formula given in equation 7.13.

an expression which gives the coupling λ'_{311} as a function of $M_{\tilde{\nu}_\tau}$ and $(\lambda_{132}^{\text{fix}})^2 + (\lambda_{231}^{\text{fix}})^2$. The formula (7.13) is used in figure 7.2 where we see the expected limit contour at 95% confidence level for the RPV signal in the $M_{\tilde{\nu}_\tau} - \lambda'_{311}$ parameter space.

Studying the behaviour of the cross section formula further two striking features can be observed. For $\lambda'_{311} \ll \lambda_{132}$, the cross section becomes independent of the coupling λ_{132} . For $\lambda'_{311} \gg \lambda_{132}$, the cross section assumes the form

$$\sigma \times \text{BR} \approx \frac{2}{3} k (M_{\tilde{\nu}_\tau}) \left(\lambda_{132}^{\text{fix}} \right)^2. \quad (7.14)$$

In this case the cross section assumes its maximum. If the maximum cross section cannot be excluded by the observed limit, then no limit can be set on λ'_{311} . This feature manifests itself in the parameter space where the limit contour becomes a vertical line (see figure 7.2).

7.2.2 SSM Z' Limits

This section deals with the limit setting of the Z' model. This is very similar to the procedure of the RPV-SUSY case due to the equivalent resonant shape of the signal distribution and the similar signal efficiency and invariant mass resolution. For the input the signal efficiency in figure A.7 and the mass resolution in figure 5.7 are used³⁶. The parametrization, the binning of the input histograms and the considered mass range stay the same as in the RPV-SUSY case. However in this model, there is no parameter space which is scanned. Only the mass $M_{Z'}$ of the hypothetical Z' is a parameter in this search (section 2.2.2). Figure 7.3 presents $\sigma^{\text{prod}} \times \text{BR}$ as well as the observed and expected limits. The SSM Z' is excluded up to a mass of 3.3 TeV.

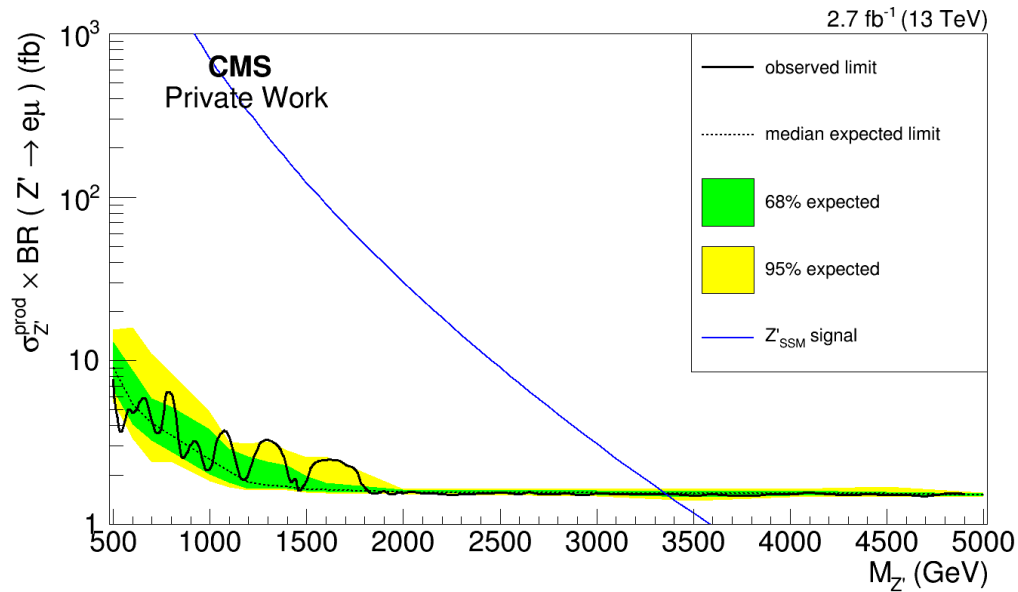


Figure 7.3: Expected and observed exclusion limits at 95% CL for the sequential standard model Z' signal in the $e\mu$ channel. The theoretical curve of the production cross section times branching ratio is the solid blue line. The expected and observed limits are presented in the same style as in figure 7.1.

³⁶It is checked that the invariant mass resolution obtained with the Z' samples is very similar to the one obtained with the RPV-SUSY samples.

7.2.3 QBH Limits

In the context of QBH models the exclusion limit is set on the threshold mass for the production of a QBH, M_{th} . The different models for the number of extra dimensions are introduced and discussed in section 2.2.3. Figure 7.4 shows $\sigma^{\text{prod}} \times \text{BR}$ of the QBH models as theory curves together with the observed and expected limit (+ uncertainty bands). Limits on $\sigma^{\text{prod}} \times \text{BR}$ are set at 95 % confidence level. The values of the limits are summarized in table 7.1.

In contrast to the resonant-like models, no parametrization is used for the QBH models. The original invariant $e\mu$ mass resolution at reconstruction level and full selection serves as an input to the limit setting.

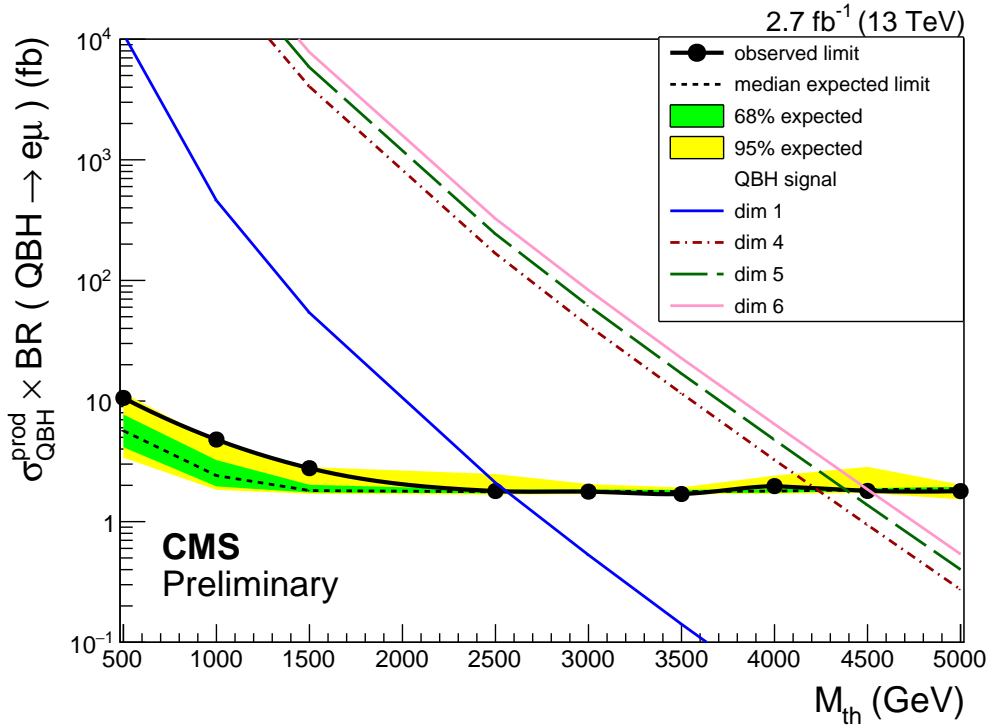


Figure 7.4: Expected and observed exclusion limits at 95% CL interpreted in the context of the extra dimensions models predicting QBHs decaying into $e\mu$. The theoretically predicted cross sections times branching ratios of the different QBH models are shown in coloured solid and dashed lines. 'dim 1' denotes the extra dimensions model with one extra dimension with the RS bulk model. 'dim 4/5/6' denote the models with the corresponding number of extra dimensions with the ADD bulk model.

Model	Number of extra dimensions n	Observed Limit on M_{th} (TeV)
RS	1	2.5
	4	4.2
ADD	5	4.3
	6	4.5

Table 7.1: Observed Limits of the QBH models at 95 % confidence level. The bulk model differs for different signal assumptions. For $n = 1$, it is the Randall-Sundrum (RS) model. For $n = 4, 5, 6$, the ADD model is used.

7.3 Influence of Systematic Uncertainties on Limit Setting

This section is devoted to determine the influence of the systematic uncertainties on the limit setting procedure. In section 5.8, the systematic uncertainties are determined to be of the order of $\sim 25\%$ over a large invariant mass range. One might wonder if the imprecise knowledge of the standard model background is a significant drawback when it comes to exclusion limits. These doubts are destroyed looking at figure 7.5. There one can see the dif-

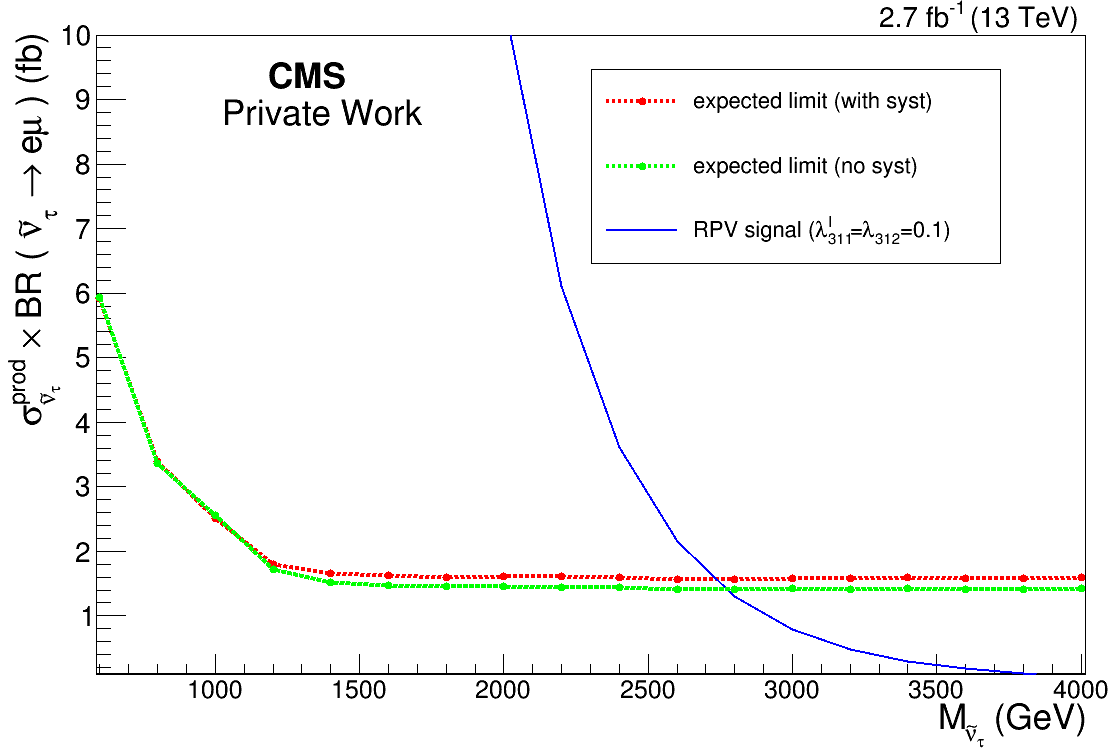


Figure 7.5: Expected limit of the RPV-SUSY model at 95 % confidence level. A comparison of the default limit setting procedure including all systematic uncertainties with the limit obtained when ignoring systematic uncertainties. The difference of the intersection points with the RPV-SUSY signal model ($\lambda_{311}^I = \lambda_{312} = 0.1$) is ~ 30 GeV.

ference of the expected limits using the RPV-SUSY model once determined with systematic uncertainties and once without systematic uncertainties. An explanation why the difference between the two is rather small for lower masses can be found in the multi-bin limit setting. Using this multi-bin approach, the systematic uncertainties can be constrained by the agreement between data and background. For higher masses, the very small amount of standard model background makes the influence of the systematic uncertainties minor. Consequently, one can live with these rather big systematic uncertainties when it comes to limit setting.

7.4 Comparison with other Searches for Lepton-Flavour-Violating Processes

Since observing LFV processes would be a clear signature for physics beyond the standard model, the community of particle physics has made quite an effort in the past few years (decades) to detect these processes. None of the collaborations reported any observation until today. Consequently, the resulting exclusion limits of this analysis can be compared to the other recent searches looking for LFV processes, also setting limits on the parameters of

BSM theories. In this section, we first focus on other searches performed at the LHC. Then we also consider low-energy experiments.

There have been several searches performed to look into the electron-muon channel at the LHC at different centre-of-mass energies. The LHC has provided data with a centre-of-mass energy of 7 TeV in 2010/2011 and of 8 TeV in 2012. The ATLAS collaboration has looked for heavy resonances decaying to electron-muon pairs at 7 TeV [1], 8 TeV [2] and currently at the 13 TeV data [3]. In the CMS collaboration, there is the analysis of 8 TeV data [4] and the analysis of 13 TeV [67], which is basically what this thesis is about.

Table 7.2 presents a comparison of the key results of the searches from ATLAS at 13 TeV and CMS at 8 TeV with this analysis. One can conclude that the 13 TeV limits for the QBH models on the mass thresholds are better than the limits obtained in the 8 TeV analysis. This is expected since we know that the cross section of the QBH production is growing stronger than the standard model background cross sections changing the centre-of-mass energy from 8 TeV to 13 TeV. A comparison of the different production cross sections is given quantitatively in reference [100]. Compared to the ATLAS 13 TeV analysis, this analysis is compatible. In the latest published results of the ATLAS analysis at 13 TeV [101], they give an $A \times \epsilon \sim 50\%$ in the electron-muon channel. This is lower than an $A \times \epsilon \sim 75\%$ in this analysis. Beside that, the difference may be a result of the different limit setting procedures. For the QBH production, the collaborations of ATLAS and CMS have performed other searches in different final states, for example QBHs decaying hadronically. Some of the corresponding results are given in references [102], [103] and [104].

In the RPV-SUSY models, the 13 TeV limits are not as good as the CMS 8 TeV analysis due to the lower luminosity.

For the Z' models, the present analysis differs from the ATLAS 13 TeV analysis again possibly due to the limit setting procedure and the lower $A \times \epsilon$ of $\sim 50\%$ [101] definitely matters.

Another possibility to search for LFV processes is at low-energy experiments. The detection principle of those experiments consists typically of muons inserted into targets of heavy nuclei, e.g. Au, Si or Al. Then one waits to observe a $\mu - e$ conversion. With this experimental setup, one is able to measure the conversion branching ratio $\text{BR}(\mu N \rightarrow e N)$, where N denotes the nucleus used in the experiment. That is how these experiments can set upper limits on RPV-SUSY couplings as a function of the τ sneutrino mass. There are several searches performed by different collaborations such as SINDRUM [5], COMET [6] and DeeMe [7]. Table 7.3 shows the results of the analyses of different experiments and collaborations and their exclusion limits on the RPV couplings [105; 106].

Considering the limits of table 7.3 the low-energy searches put strict limits at 90% confidence level on the RPV couplings. The SINDRUM collaboration sets a limit on the couplings

Model	Variable of observed limit	Thesis (13 TeV, 2.7 fb ⁻¹)	ATLAS (13 TeV, 3.2 fb ⁻¹)	CMS (8 TeV, 19.7 fb ⁻¹)
RPV-SUSY	$M_{\tilde{\nu}_\tau}$ for $\lambda_{132} = \lambda'_{311} = 0.01$	1.0 TeV	N/A	1.28 TeV
	$M_{\tilde{\nu}_\tau}$ for $\lambda_{132} = \lambda'_{311} = 0.1$	2.7 TeV	N/A	N/A
SSM Z'	$M_{Z'}$	3.3 TeV	3.01 TeV	N/A
QBH	$M_{th}^{n=1}$ (RS)	2.5 TeV	2.44 TeV	2.36 TeV
	$M_{th}^{n=6}$ (ADD)	4.5 TeV	4.54 TeV	3.63 TeV

Table 7.2: Comparison of this analysis with other similar analyses from the ATLAS collaboration and comparing this analysis to analyses at different centre-of-mass energies. The values in parentheses give the centre-of-mass energy and the total integrated luminosity of the analysed dataset.

Experiment	Limit on $\lambda'_{311} \cdot \lambda$ (90 % CL)
SINDRUM	$1.633 \times 10^{-7} \left(\frac{M_{\tilde{\nu}_\tau}}{\text{TeV}} \right)^2$
DeeMe	$1.550 \times 10^{-8} \left(\frac{M_{\tilde{\nu}_\tau}}{\text{TeV}} \right)^2$
COMET-I	$1.830 \times 10^{-8} \left(\frac{M_{\tilde{\nu}_\tau}}{\text{TeV}} \right)^2$
COMET-II	$1.198 \times 10^{-9} \left(\frac{M_{\tilde{\nu}_\tau}}{\text{TeV}} \right)^2$

Table 7.3: Comparison of this analysis with other low-energy analyses searching for LFV processes in the $\mu - e$ conversion. The limit at 90 % confidence level is given on the product of the couplings $\lambda'_{311} \cdot \lambda$, where λ'_{311} is the same coupling as already used in this search. The parameter λ just denotes that this is not only a limit on λ_{132} but also on other even permutations of the indices. The nuclei used in these searches are Au (SINDRUM), C and Si (DeeMe), Al and Ti (COMET-I and COMET-II). [105] [106]

of $|\lambda'_{311} \lambda_{132}| < 10^{-7}$ for $M_{\tilde{\nu}_\tau} = 1$ TeV. The difference among the low-energy experiments mainly comes from using different nuclei since their limit is dependent on the different muon capture rates [106].

Figure 7.6 shows a comparison of the limits from this thesis with the limits determined by the SINDRUM collaboration in the $\lambda'_{311} - \lambda_{132}$ parameter space. For the SINDRUM limits, the values of table 7.3 are used. The lines representing the limits obtained by this analysis are calculated with the formula given in equation (7.13), except that for this usecase not the value of $\lambda_{132} = \lambda_{231}$ is fixed but the tau sneutrino mass $M_{\tilde{\nu}_\tau}$.

The limits from low-energy experiments are significantly better than the limits of this analysis even though we put limits at 95 % confidence level. This is mainly due to the very low background in the low-energy experiments. Additionally, the signature of a single electron emerging from a nucleus at rest is very clean. However, one should not conclude that the direct searches of CMS and ATLAS are meaningless since it is always important to look at physical phenomena from different angles. Having two independent strategies (detector setup, energy scale, etc.) of detecting new phenomena is essential in science. If one of the experiments saw some indication of LFV processes, then the other experiment would be useful to cross-check the observation.

For the SSM Z' , electroweak precision measurements have set limits on the mass of the Z' of 1.4 TeV at 95 % confidence level [107]. However, a comparison with the results of this analysis is rather hard to provide since the electroweak precision measurements assume a mixing between the SM Z boson and the SSM Z' .

In the QBH case, the situation is quite different. Couplings of QBHs at this low energy scale, where the indirect searches test physics, are very weak [108]. However, if one assumes a continuous mass spectrum of QBHs instead of a discrete one, a sizeable contribution due to QBHs can be obtained [109]. On the other hand, if the mass spectrum is indeed non-continuous, as assumed in this search, the QBH states would not contribute significantly to processes like a Kaon decay into an electron-muon pair ($K_L \rightarrow e\mu$). Thus, there are no indirect limits from low energy experiments for comparison.

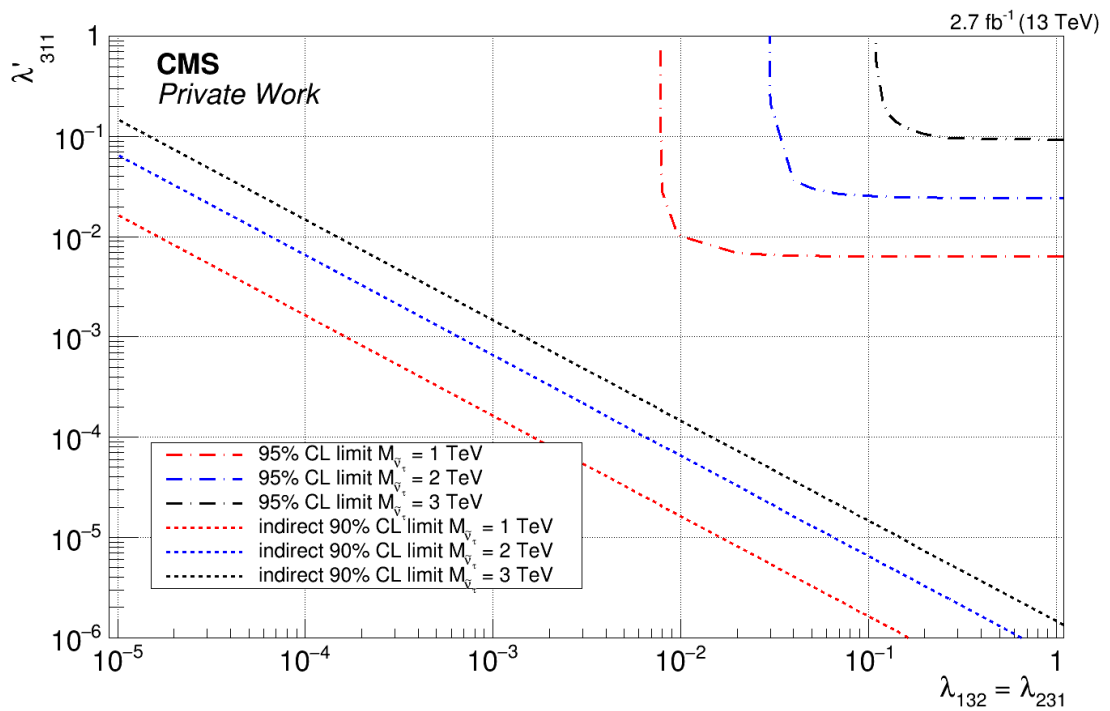


Figure 7.6: Expected limit in the $\lambda'_{311} - \lambda_{132}$ parameter space at 95% and 90% confidence level for the limits of this analysis and the limits from the SINDRUM collaboration, respectively. For each line, the area right above the line is excluded by the corresponding limit.

8 Summary and Conclusion

In this thesis, a search for lepton-flavour-violating processes in the electron-muon final state is presented. The 2015 CMS data at a centre-of-mass energy of 13 TeV summing up to an integrated luminosity of 2.7 fb^{-1} were used. The background expectation from standard model physics has been studied and its uncertainties have been evaluated.

Three models predicting new physics beyond the standard model have been studied. The resonant production of a tau sneutrino in RPV-SUSY, the production of a Z' in the context of the SSM and QBHs in several extra dimensions models. No indications of new physics have been found comparing the standard model expectation with the measured data. Exclusion limits on the parameters of the studied models have been set.

The tau sneutrino in RPV-SUSY has been excluded at 95 % confidence level for masses $M_{\tilde{\nu}_\tau} < 1.0 \text{ TeV}$ for couplings $\lambda_{132} = \lambda'_{311} = 0.01$ and for masses $M_{\tilde{\nu}_\tau} < 2.7 \text{ TeV}$ for couplings $\lambda_{132} = \lambda'_{311} = 0.1$. Within the sequential standard model, limits were set on the mass of the Z' resulting in an exclusion of Z' s of a mass of up to 3.3 TeV. For the models with extra dimensions, quantum black holes have been excluded at 95 % confidence level with a threshold mass of smaller than 2.5 TeV for $n = 1$ extra dimensions in the RS bulk model. For $n = 6$ extra dimensions and the ADD model, QBHs with threshold mass $M_{\text{th}} < 4.5 \text{ TeV}$ are excluded.

Due to the model-independent search strategy the results of this analysis can be re-interpreted for all models predicting a heavy, short-lived resonance decaying into an electron-muon pair.

It has been evaluated that this search is compatible with other current direct searches at the LHC. In some cases like for the QBHs this search beats the limits of former analyses by the ATLAS or CMS collaborations. The comparison with direct searches yields that these searches are excluding a bigger range in the parameter space of the RPV-SUSY models. For the QBHs, the indirect searches are currently not providing any results.

For the next few years, the plan of the LHC foresees a period of high luminosity. During this period, it is expected to measure an amount of data which corresponds to an integrated luminosity of $\sim 100 \text{ fb}^{-1}$ per year. In 2016 data taking, approximately $10 \times \mathcal{L}_{int,2015}$ has already been provided by the LHC. This will increase the sensitivity of the direct searches at the LHC. The field of direct searches for new physics will remain a subject of broad and current interest in particle physics.

A Appendix

A.1 Notation and Units

This section discusses the conventions used in this analysis, mainly describing notation and units. Since we are dealing with quantum mechanical and relativistic effects at the same time, there are formulae with the Planck constant and the velocity of light popping up everywhere. To simplify the equations, we choose the system of natural units, where

$$\hbar = c = 1 \quad (\text{A.1})$$

holds. This leaves the physics untouched, but has the nice consequence that the momentum, energy and mass have the same unit. In the case of particle physics one uses the Electronvolt $1 \text{ eV} = 1.602 \times 10^{-19} \text{ J}$.

The notation used in section 2 is called covariant notation, where Lorentz indices are denoted by Greek letters. The metric tensor can be written as

$$g_{\mu\nu} = \begin{bmatrix} 1 & & & \\ & -1 & & \\ & & -1 & \\ & & & -1 \end{bmatrix}. \quad (\text{A.2})$$

The product of two 4-vectors, like momenta, is defined by the metric tensor

$$x \cdot y = g_{\mu\nu} x^\mu y^\nu. \quad (\text{A.3})$$

For Latin letters we use the Einstein convention, if not indicated otherwise, which means that we are summing over the indices if they appear more than once in an expression. The so called 'slash notation' is given by

$$\not{p} = \gamma_\mu p^\mu, \quad (\text{A.4})$$

where p^μ is a 4-vector and γ_μ are the Dirac matrices. They are defined by fulfilling the anti-commutation relation

$$\{\gamma^\mu, \gamma^\nu\} = \gamma^\mu \gamma^\nu + \gamma^\nu \gamma^\mu = 2g^{\mu\nu} Id_4. \quad (\text{A.5})$$

A.2 Narrow Width Approximation

This section deals with the narrow width approximation (NWA) which is used to simplify calculations of scattering processes in high energy physics. The goal is to summarize under what conditions this approximation is valid and how this approximation simplifies the calculation. The NWA is extensively used in the RPV-SUSY model to calculate cross sections and justify some proceedings of the limit setting (section 2.2.1). This brief explanation is based on [110]. The required conditions to apply the NWA in a process are:

- (i) The total width of the particle should be much smaller than its mass: $\frac{\Gamma}{M} \ll 1$
- (ii) The particles that are products of the decay of the resonant particle ought to have much smaller masses: $m \ll M$
- (iii) The centre-of-mass energy is much greater than the mass of the particle: $\sqrt{s} \gg M$
- (iv) No (significant) interference with non-resonant processes
- (v) The resonant propagator is separable from the matrix element

For the RPV-SUSY case the conditions (i),(ii) and (iv) are fulfilled. Also the centre-of-mass energy is greater than the biggest mass we are looking for $M_{\tilde{\nu}_\tau} \leq 6$ TeV. The condition (v) is not so easy to verify since that is strictly speaking never fully true with daughter particle of finite mass ($m \neq 0$). However, one can argue that in the approximation $m \ll M$ the dependence on the mass is negligible. Since the muon as the heaviest daughter particle has a mass of $m_\mu = 105$ MeV [33] and the search region for RPV-SUSY starts at 200 GeV, this condition is fulfilled.

Condition (v) gives the starting point for the simplified calculations of cross sections. Since the propagator can be separated from the other components of the matrix element and the phase space factors, one can integrate it out and gets a constant for the propagator [110]. This allows us to factorize the cross section of a process into a production cross section and a branching ratio which denotes the fractional probability to decay into a specific final state. This is the justification to write the cross section like

$$\sigma(d\bar{d} \rightarrow \tilde{\nu}_\tau \rightarrow e\mu) = \sigma_{\text{prod}} \times \text{BR}(\tilde{\nu}_\tau \rightarrow e\mu) \quad (\text{A.6})$$

for the RPV-SUSY case. All of the above arguments are also valid for the SSM Z' model. The condition (iv) is also fulfilled since we produce the SSM samples without including interference effects with other copies of standard model gauge bosons.

A.3 Details of Trigger Strategy

In this thesis, a logical 'or' of the single electron and single muon trigger is used. This is a main difference compared to the version of the analysis inside CMS in [67], where only a single muon trigger was used. Thus, the following section tries to motivate the new strategy and address the improvements due to this update. First of all, one has to consider the single muon trigger. Since this is relying on muon reconstruction at high- p_T , the efficiency of single muon trigger is affected and, more importantly, decreased due to the misreconstruction of muons that are showering in the iron yoke. This problem of decreasing efficiency at high p_T can be seen in figure A.1. This figure shows the single muon trigger efficiency as a function

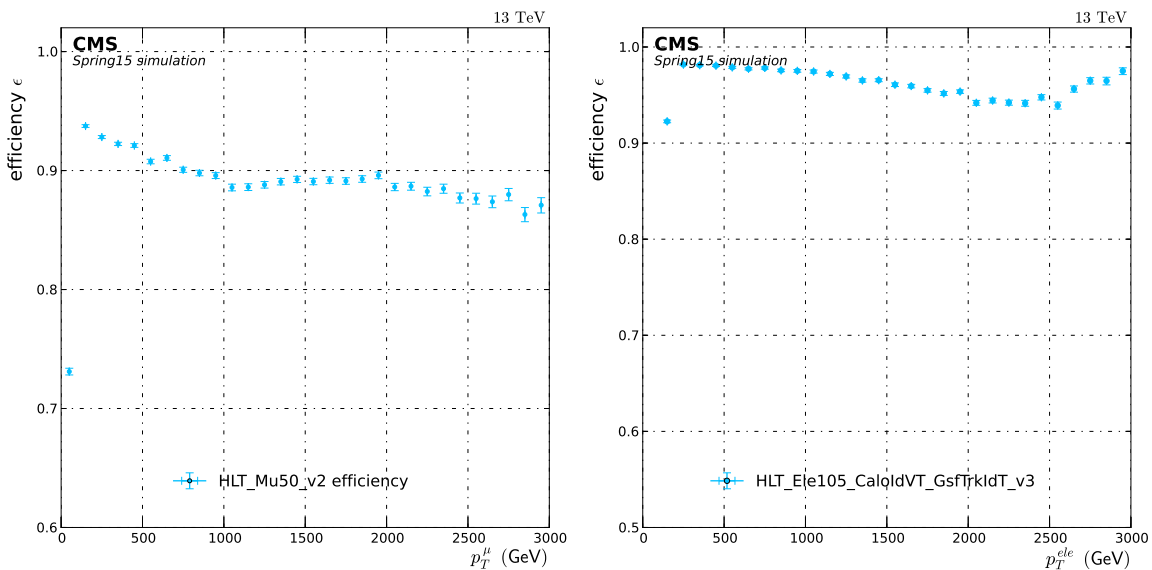


Figure A.1: Left: Efficiency of single muon trigger as a function of the p_T of the muon candidate. Right: Efficiency of single electron trigger as a function of the p_T of the electron candidate.

of the transverse momentum of the muon candidate. This is why the trigger strategy is updated by including also a single electron trigger. The behaviour of the efficiency at high p_T electrons is opposite to that of a single muon trigger, since for high transverse momenta the reconstruction of electron candidates does not suffer from bremsstrahlung effects as much as for low- p_T electrons. Figure A.1 presents the efficiency of the single electron trigger used in this analysis as a function of the p_T of the electron candidate.

A.4 Signal Samples

In this section the so-called signal samples (samples with new physics contents) are listed and some of their properties are given below. In table A.1 one can see the properties of the simulated RPV signal samples. The properties listed here are the coupling parameters λ_{132} and λ'_{311} as well as the mass $M_{\tilde{\nu}_\tau}$. In addition the corresponding cross section times branching ratio is given. Furthermore the correction factor of the cross section including NLO processes is mentioned. Table A.2 offers a summary of the SSM Z' signal samples. It gives the dependence of the production cross section times branching ratio compared to the only parameter in this search, the mass $M_{Z'}$. The table A.3 is concerned with the characteristics of the QBH signal samples. The number of extra dimensions, the threshold mass for QBH production and the corresponding cross section times branching ratio are listed there.

λ_{132}	λ'_{311}	$M_{\tilde{\nu}_\tau}$ [GeV]	$\sigma \cdot \text{BR}(\tilde{\nu}_\tau \rightarrow e^\pm \mu^\mp)$ [fb]	NLO (QCD) k-factor
0.01	0.01	200	585	1.34
0.01	0.01	300	158	1.36
0.01	0.01	400	59.9	1.37
0.01	0.01	500	27.6	1.37
0.01	0.01	600	14.4	1.37
0.01	0.01	700	8.18	1.37
0.01	0.01	800	4.95	1.36
0.01	0.01	900	3.13	1.35
0.01	0.01	1000	2.06	1.34
0.01	0.01	1200	0.969	1.32
0.01	0.01	1400	0.493	1.30
0.01	0.01	1600	0.267	1.27
0.01	0.01	1800	0.150	1.25
0.01	0.01	2000	0.0864	1.22
0.01	0.01	2500	0.0239	1.16
0.01	0.01	3000	0.00716	1.11
0.01	0.01	3500	0.00214	1.08
0.01	0.01	4000	0.000642	1.05
0.01	0.01	4500	0.000185	1.05
0.01	0.01	5000	$5.14 \cdot 10^{-05}$	1.08
0.01	0.01	5500	$1.35 \cdot 10^{-05}$	1.17
0.01	0.01	6000	$3.31 \cdot 10^{-06}$	1.36
0.01	0.01	6500	$7.87 \cdot 10^{-07}$	1.68
0.1	0.1	3000	0.716	1.12
0.1	0.1	3500	0.217	1.08
0.1	0.1	4000	0.0658	1.06
0.2	0.2	4000	0.282	1.06
0.2	0.2	4500	0.0902	1.05
0.2	0.2	5000	0.0306	1.10
0.2	0.2	5500	0.0120	1.23
0.2	0.2	6000	0.00585	1.33
0.2	0.2	6500	0.00351	1.0
0.5	0.5	4000	2.60	1.06
0.5	0.5	4500	1.07	1.05
0.5	0.5	5000	0.517	1.09
0.5	0.5	5500	0.290	1.18
0.5	0.5	6000	0.184	1.4
0.5	0.5	6500	0.127	1.6

Table A.1: Summary of simulated RPV signal samples. Each sample contains 15000 generated events. The cross section is taken from the event generator CalcHEP using the PDF set CTEQ6L1. The samples where the couplings are greater than 0.01 are only used to verify if the acceptance times efficiency is not effected by different coupling values.

$M_{Z'}$ [GeV]	$\sigma \cdot \text{BR}(Z' \rightarrow e^\pm \mu^\mp)$ [pb]
500	10.1
600	4.77
700	2.61
800	1.84
900	1.18
1000	0.616
1100	0.466
1200	0.328
1300	0.240
1400	0.164
1500	0.133
1600	0.0928
1700	0.0643
1800	0.0426
1900	0.0414
2000	0.0306
2200	0.0203
2400	0.0118
2600	0.00759
2800	0.00440
3000	0.00295
3500	0.00113
4000	0.000523
4500	0.000206
5000	0.000113

Table A.2: Summary of simulated SSM Z' signal samples. The cross section is taken from the event generator PYTHIA 8. Each sample contains $\sim 10\text{k}$ generated events.

N_{dim}	Threshold mass for QBH production [GeV]	$\sigma \cdot \text{BR}(QBH \rightarrow e\mu)$ [pb]
1	500	11.0
1	1000	0.459
1	1500	0.0539
1	2000	0.00951
1	2500	0.00210
1	3000	0.000529
1	3500	0.000141
1	4000	0.0000394
1	4500	0.0000113
1	5000	0.00000323
1	5500	0.000000927
1	6000	0.000000260
1	6500	0.000000071
4	500	719
4	1000	32.8
4	1500	4.05
4	2000	0.744
4	2500	0.167
4	3000	0.0420
4	3500	0.0116
4	4000	0.00325
4	4500	0.000939
4	5000	0.000274
4	5500	0.0000792
4	6000	0.0000223
4	6500	0.00000604
5	500	1030
5	1000	47.2
5	1500	5.84
5	4000	0.00477
5	4500	0.00137
5	5500	0.000115
6	500	1350
6	1000	62.7
6	1500	7.80
6	2000	1.43
6	2500	0.325
6	3000	0.0831
6	3500	0.0226
6	4000	0.00643
6	4500	0.00185
6	5000	0.000538
6	5500	0.000153
6	6000	0.0000441
6	6500	0.0000119

Table A.3: Summary of simulated QBH signal samples. The number of extra dimensions is listed as well as the threshold mass for QBH production and the corresponding cross section. The cross section is taken from the QBH generator. [75]

A.5 Standard Model Background Samples

In this section the background samples are listed in tables A.4 and A.5 and some of their properties are given. The Monte Carlo generator for each sample as well as the kinematic cuts, the cross section and the number of events used in the simulations are mentioned. For both tables, the cross section is given with 3 significant digits since the systematic uncertainty is in the order of percent. For the number of events denoted as N_{events} an order of magnitude is given.

Generator	Process	Kinematic Cuts [GeV]	σ_{used} [pb]	k-factor used	N_{events}
Drell-Yan					
POWHEG	$Z \rightarrow \mu\mu$	$50 \leq M_{\mu\mu} \leq 120$	1980.0 (NLO)	No	$\sim 2.8\text{M}$
POWHEG	$Z \rightarrow \mu\mu$	$120 \leq M_{\mu\mu} \leq 200$	19.3 (NLO)	No	$\sim 100\text{k}$
POWHEG	$Z \rightarrow \mu\mu$	$200 \leq M_{\mu\mu} \leq 400$	2.73 (NLO)	No	$\sim 100\text{k}$
POWHEG	$Z \rightarrow \mu\mu$	$400 \leq M_{\mu\mu} \leq 800$	0.241 (NLO)	No	$\sim 100\text{k}$
POWHEG	$Z \rightarrow \mu\mu$	$800 \leq M_{\mu\mu} \leq 1400$	0.0168 (NLO)	No	$\sim 100\text{k}$
POWHEG	$Z \rightarrow \mu\mu$	$1400 \leq M_{\mu\mu} \leq 2300$	0.00139 (NLO)	No	$\sim 100\text{k}$
POWHEG	$Z \rightarrow \mu\mu$	$2300 \leq M_{\mu\mu} \leq 3500$	8.95e-05 (NLO)	No	$\sim 100\text{k}$
POWHEG	$Z \rightarrow \mu\mu$	$3500 \leq M_{\mu\mu} \leq 4500$	4.14e-06 (NLO)	No	$\sim 100\text{k}$
POWHEG	$Z \rightarrow \mu\mu$	$4500 \leq M_{\mu\mu} \leq 6000$	4.56e-07 (NLO)	No	$\sim 100\text{k}$
POWHEG	$Z \rightarrow \mu\mu$	$M_{\mu\mu} \geq 6000$	2.07e-08 (NLO)	No	$\sim 100\text{k}$
POWHEG	$Z \rightarrow ee$	$50 \leq M_{ee} \leq 120$	1980.0 (NLO)	No	$\sim 3\text{M}$
POWHEG	$Z \rightarrow ee$	$120 \leq M_{ee} \leq 200$	19.3 (NLO)	No	$\sim 100\text{k}$
POWHEG	$Z \rightarrow ee$	$200 \leq M_{ee} \leq 400$	2.73 (NLO)	No	$\sim 100\text{k}$
POWHEG	$Z \rightarrow ee$	$400 \leq M_{ee} \leq 800$	0.241 (NLO)	No	$\sim 100\text{k}$
POWHEG	$Z \rightarrow ee$	$800 \leq M_{ee} \leq 1400$	0.0168 (NLO)	No	$\sim 100\text{k}$
POWHEG	$Z \rightarrow ee$	$1400 \leq M_{ee} \leq 2300$	0.00139 (NLO)	No	$\sim 100\text{k}$
POWHEG	$Z \rightarrow ee$	$2300 \leq M_{ee} \leq 3500$	8.95e-05 (NLO)	No	$\sim 100\text{k}$
POWHEG	$Z \rightarrow ee$	$3500 \leq M_{ee} \leq 4500$	4.14e-06 (NLO)	No	$\sim 100\text{k}$
POWHEG	$Z \rightarrow ee$	$4500 \leq M_{ee} \leq 6000$	4.56e-07 (NLO)	No	$\sim 100\text{k}$
POWHEG	$Z \rightarrow ee$	$M_{ee} \geq 6000$	2.07e-08 (NLO)	No	$\sim 100\text{k}$
aMCatNLO	$Z \rightarrow ll + \text{Njets}$	$M > 50$	6100 (NLO)	No	$\sim 28.7\text{M}$
aMCatNLO	$Z \rightarrow ll + \text{Njets}$	$100 < M < 200$	226 (NLO)	No	$\sim 100\text{k}$
aMCatNLO	$Z \rightarrow ll + \text{Njets}$	$400 < M < 500$	0.423 (NLO)	No	$\sim 100\text{k}$
aMCatNLO	$Z \rightarrow ll + \text{Njets}$	$500 < M < 700$	0.240 (NLO)	No	$\sim 100\text{k}$
aMCatNLO	$Z \rightarrow ll + \text{Njets}$	$700 < M < 800$	0.035 (NLO)	No	$\sim 100\text{k}$
aMCatNLO	$Z \rightarrow ll + \text{Njets}$	$800 < M < 1000$	0.03 (NLO)	No	$\sim 100\text{k}$
aMCatNLO	$Z \rightarrow ll + \text{Njets}$	$1500 < M < 2000$	0.002 (NLO)	No	$\sim 100\text{k}$
aMCatNLO	$Z \rightarrow ll + \text{Njets}$	$2000 < M < 3000$	0.00054 (NLO)	No	$\sim 100\text{k}$
$t\bar{t}$					
POWHEG	$t\bar{t}$	-	730 (LO)	Yes, 1.116 (NLO)	$\sim 116\text{M}$
POWHEG	$t\bar{t}$	$700 \leq M_{t\bar{t}} \leq 1000$	67.3 (LO)	Yes, 1.116 (NLO)	$\sim 3.1\text{M}$
POWHEG	$t\bar{t}$	$M_{t\bar{t}} \geq 1000$	18.7 (LO)	Yes, 1.116 (NLO)	$\sim 1.8\text{M}$
$t\bar{t}$ high mass samples					
POWHEG	$t\bar{t}$	$500 \leq M_{ll} \leq 800$	0.286 (LO)	Yes, 1.116 (NLO)	$\sim 200\text{k}$
POWHEG	$t\bar{t}$	$800 \leq M_{ll} \leq 1200$	0.0286 (LO)	Yes, 1.116 (NLO)	$\sim 200\text{k}$
POWHEG	$t\bar{t}$	$1200 \leq M_{ll} \leq 1800$	0.00267 (LO)	Yes, 1.116 (NLO)	$\sim 200\text{k}$
POWHEG	$t\bar{t}$	$M_{ll} \geq 1800$	0.000153 (LO)	Yes, 1.116 (NLO)	$\sim 40\text{k}$
Single top					
POWHEG	$tq \rightarrow l\nu b q$ (t channel)	-	103 (NNLO)	No	$\sim 3.3\text{M}$
POWHEG	$\bar{t}q \rightarrow l\nu b q$ (t channel)	-	80.9 (NNLO)	No	$\sim 1.7\text{M}$
POWHEG	$tW \rightarrow 2l2\nu b$	-	38.1 (NNLO)	No	$\sim 1\text{M}$
POWHEG	$\bar{t}W \rightarrow 2l2\nu \bar{b}$	-	38.1 (NNLO)	No	$\sim 1\text{M}$
$W\gamma$					
MADGRAPH	$W\gamma \rightarrow l\nu\gamma$	-	405 (LO)	No	$\sim 6.1\text{M}$
Diboson					
POWHEG	$WZ \rightarrow 3l\nu$	-	4.43 (LO)	No	1.9M
POWHEG	$WW \rightarrow 2l2\nu$	-	12.2 (LO)	Yes, 1.1619 (NLO)	1.9M
POWHEG	$WW \rightarrow 4q$	-	51.7 (LO)	Yes, 1.1619 (NLO)	2M
POWHEG	$WW \rightarrow l\nu qq$	-	49.9 (LO)	Yes, 1.1619 (NLO)	2M
POWHEG	$ZZ \rightarrow 2l2\nu$	-	0.564 (LO)	No	8.4M
POWHEG	$ZZ \rightarrow 4l$	-	1.26 (LO)	No	6.7M
WW high mass samples					
POWHEG	$WW \rightarrow 2l2\nu$	$200 \leq M_{ll} \leq 600$	1.19 (LO)	Yes, 1.1619 (NLO)	$\sim 200\text{k}$
POWHEG	$WW \rightarrow 2l2\nu$	$600 \leq M_{ll} \leq 1200$	0.0487 (LO)	Yes, 1.1619 (NLO)	$\sim 200\text{k}$
POWHEG	$WW \rightarrow 2l2\nu$	$1200 \leq M_{ll} \leq 2500$	0.00306 (LO)	Yes, 1.1619 (NLO)	$\sim 200\text{k}$
POWHEG	$WW \rightarrow 2l2\nu$	$M_{ll} \geq 2500$	0.0000464 (LO)	Yes, 1.1619 (NLO)	$\sim 40\text{k}$

Table A.4: Information about the background Monte Carlo samples from official production.

Generator	Process	Kinematic Cuts (in GeV)	σ_{used} (pb)	k-fact used	N_{events}
Wjets					
MADGRAPH	$W(l\nu) + jets$	-	50700 (NNLO)	No	$\sim 65M$
MADGRAPH	$W(l\nu) + jets$	$100 < H_T < 200$	1290.0 (NNLO)	No	$\sim 10M$
MADGRAPH	$W(l\nu) + jets$	$200 < H_T < 400$	386 (NNLO)	No	$\sim 5M$
MADGRAPH	$W(l\nu) + jets$	$400 < H_T < 600$	48.0 (NNLO)	No	$\sim 2M$
MADGRAPH	$W(l\nu) + jets$	$600 < H_T < 800$	12.9 (NNLO)	No	$\sim 4M$
MADGRAPH	$W(l\nu) + jets$	$800 < H_T < 1200$	5.26 (NNLO)	No	$\sim 2M$
MADGRAPH	$W(l\nu) + jets$	$1200 < H_T < 2500$	1.33 (NNLO)	No	$\sim 250k$
MADGRAPH	$W(l\nu) + jets$	$2500 < H_T < Inf$	0.0309 (NNLO)	No	$\sim 250k$
QCD					
PYTHIA 8	QCD	$20 \leq p_T \leq 30$	2970000 (LO)	No	$\sim 16M$
PYTHIA 8	QCD	$30 \leq p_T \leq 50$	1650000 (LO)	No	$\sim 14M$
PYTHIA 8	QCD	$50 \leq p_T \leq 80$	438000 (LO)	No	$\sim 19M$
PYTHIA 8	QCD	$80 \leq p_T \leq 120$	106000 (LO)	No	$\sim 3.9M$
PYTHIA 8	QCD	$120 \leq p_T \leq 170$	25200 (LO)	No	$\sim 4M$
PYTHIA 8	QCD	$170 \leq p_T \leq 300$	8650 (LO)	No	$\sim 4M$
PYTHIA 8	QCD	$300 \leq p_T \leq 470$	797 (LO)	No	$\sim 3M$
PYTHIA 8	QCD	$470 \leq p_T \leq 600$	79.0 (LO)	No	$\sim 2M$
PYTHIA 8	QCD	$600 \leq p_T \leq 800$	25.1 (LO)	No	$\sim 2M$
PYTHIA 8	QCD	$800 \leq p_T \leq 1000$	4.71 (LO)	No	$\sim 2M$
PYTHIA 8	QCD	$p_T \geq 1000$	1.62 (LO)	No	$\sim 2M$

Table A.5: Information about the jet-misidentified-as-an-electron background Monte Carlo samples from official production. This is only used in the closure test of the datadriven approach. These Monte Carlo samples are not used further in any statistical interpretation of the results.

A.6 Distributions of Lepton Kinematics

This section presents a few more kinematic event yield distributions of the muon (A.2) and electron (figure A.3) after final selection. Standard Model background samples and data are compared and shown together with two signal examples from RPV-SUSY and QBH. Additionally kinematic information of the highest invariant mass events in 2015 CMS data are summarized in table A.6. The distribution of the $\Delta\phi(e, \mu)$ between the selected electron and muon is shown in figure A.4. To obtain the graphic below the event yield distribution the following calculation is done for each bin. The distribution called Data/Bkg is defined as

$$\text{Data/Bkg} = \frac{N_{\text{Data}}}{N_{\text{Bkg}}}, \quad (\text{A.7})$$

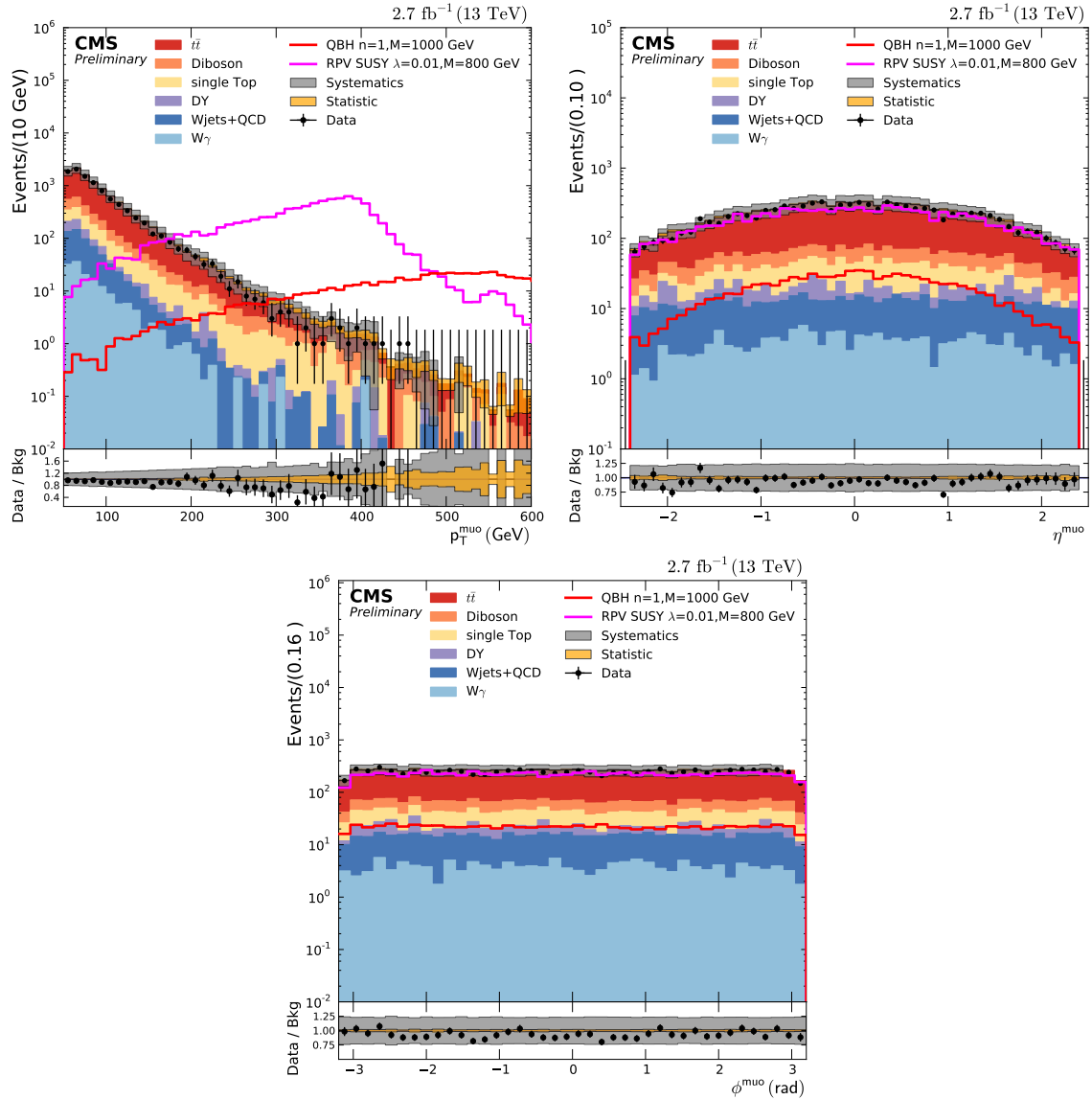


Figure A.2: p_T (top left), η (top right) and ϕ (bottom) distributions of selected muon candidates. All shown events are required to pass the complete selection described in section 5.5.1 and contain therefore at least one electron and one muon.

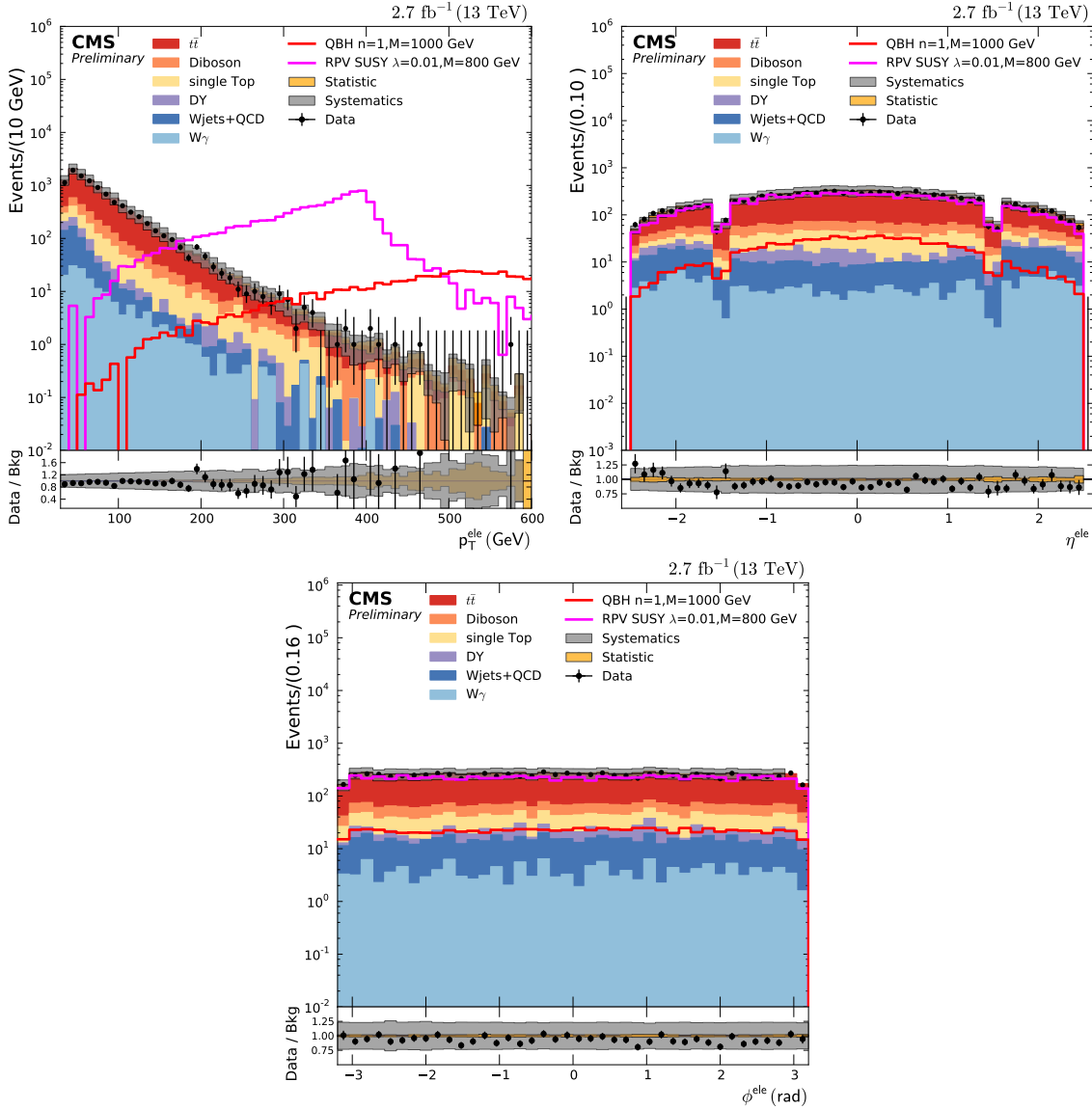


Figure A.3: p_T (top left), η (top right) and ϕ (bottom) distributions of selected electron candidates. All shown events are required to pass the complete selection described in section 5.5.2 and contain therefore at least one electron and one muon.

with the corresponding uncertainty

$$\sigma = \frac{\sigma(N_{\text{Bkg}})}{N_{\text{Bkg}}} \quad (\text{A.8})$$

represented by the grey and yellow bands for systematic and statistical uncertainty of the background event yield, respectively. This ratio is shown in order to directly see whether there are significant differences between expected background and data in the corresponding spectrum.

Mass (GeV)	p_T^e (GeV)	η^e	ϕ^e	p_T^μ (GeV)	η^μ	ϕ^μ
1635	247	-2.1	2.11	142.9	2.2	-1.3
1329	326	2.26	0.24	223.2	-0.84	-3.05
1274	282.3	-2.18	2.77	247.5	0.88	-0.69
1069	199.6	1.85	-0.6	155	-1.7	2.82
1039	578	-0.26	0.40	360	0.79	-2.92
942	66.4	-2.41	-1.18	150.7	2.06	1.06
916	146.6	1.71	0.46	117.5	-2.13	-2.53

Table A.6: Some information about the highest invariant mass events selected in the electron-muon analysis in 2015 CMS data. The transverse momentum p_T , pseudorapidity η , and the angle ϕ of the selected electron and muon of the event are listed. No uncertainties are shown here.

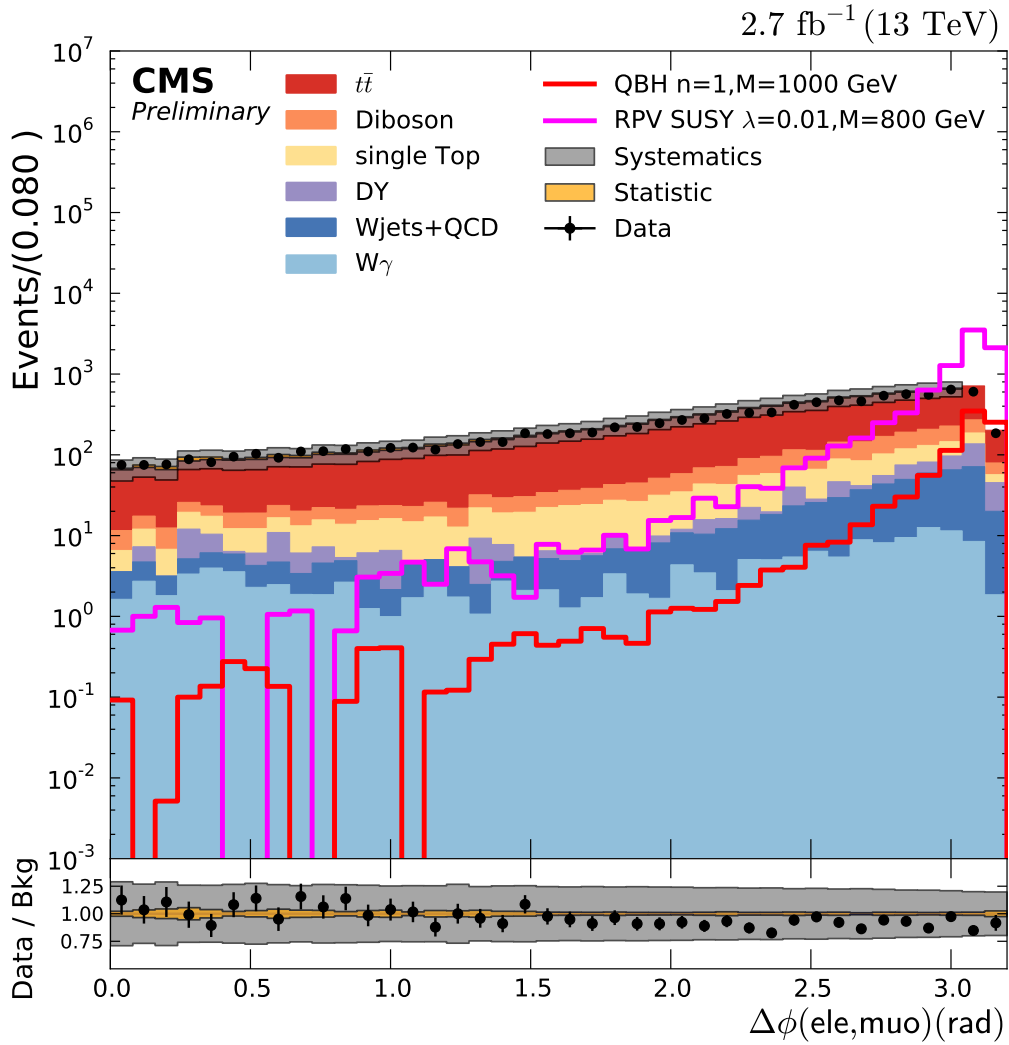


Figure A.4: Event yield as a function of $\Delta\phi(e, \mu)$ for signal and standard model background samples as well as data. The signal samples peak at $\Delta\phi(e, \mu) = \pi$, whereas the background distribution is flatter.

A.7 Investigations on Mass Resolution

In this section, a method is presented to check whether the amount of uncertainty in the invariant mass resolution (see e.g. figure 5.7) is sufficient to cover effects of different muon alignment scenarios. The reason why this cross check is performed is explained in the following. At high- p_T the muon momentum reconstruction is crucially dependent on detector alignment, most importantly the muon chambers with respect to each other and with respect to the inner tracker, which also plays a role in muon reconstruction. Thus, the standard method for analyses of high- p_T objects is usually to check the impact of different muon alignment scenarios in order to obtain the systematic uncertainty on the invariant mass resolution.

For this cross check, two different alignment scenarios are used. The ‘asymptotic’ scenario should be the final alignment scenario after final track-based alignment. All plots in this thesis are by default based on the ‘asymptotic’ scenario. The other scenario is called ‘startup’ and is a hardware-based alignment of the DT chambers and for the CSC chambers a comparison of the Run-I hardware alignment and the final track-based results is performed.

The ‘asymptotic’ is already studied in the analysis section. For the ‘startup’ scenario the method to determine the mass resolution is the same. Figure A.5 shows the comparison of the two different scenarios and one can conclude that this deviation in the high mass region is covered by the systematic uncertainties on the mass resolution in figure 5.7.

Another issue of the mass resolution concerning the parametrization of the method is

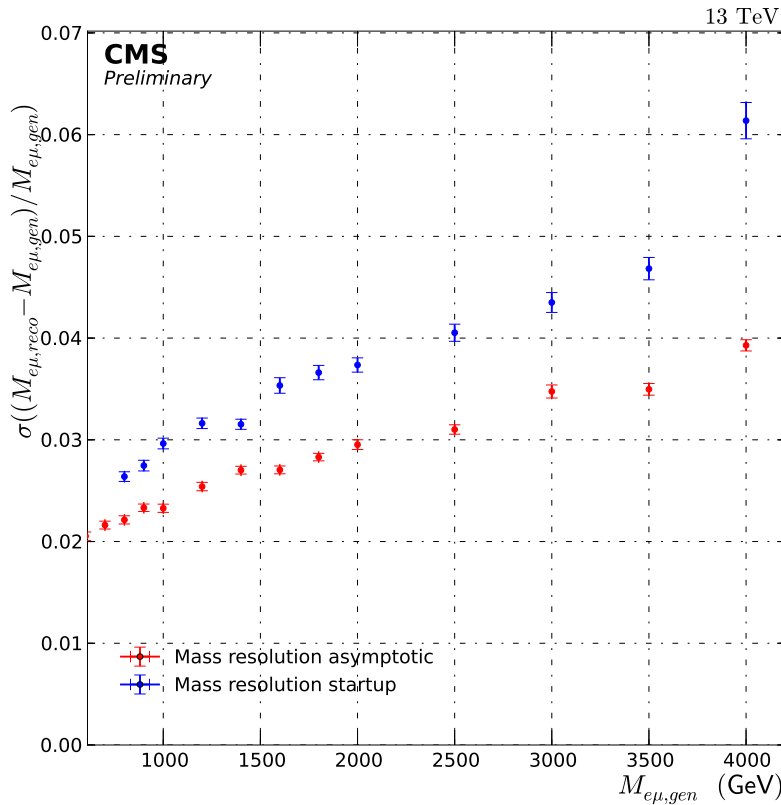


Figure A.5: Comparison of the impact on the invariant mass resolution of the different muon alignment scenarios denoted here as ‘asymptotic’ and ‘startup’. The ‘asymptotic’ alignment is the default muon alignment in this analysis. The difference between the two muon alignment scenarios is covered by the systematic uncertainties discussed in section 5.8.2.

investigated. The distributions of the individual mass resolution plots have a tail in the negative region partially due to effect that muons radiate Bremsstrahlung. This causes a deficit in the reconstructed invariant mass and consequently leads to an asymmetry of the individual mass resolution distribution with respect to the origin. Another reason could be the electron leg not being reconstructed correctly, since this is already apparent at masses of $m_{\tilde{\nu}_\tau} = 1200$ GeV, where Bremsstrahlung induced by muons should not be a big issue. Thus, a Gaussian is not the best parametrization one can think of. As an alternative to the Gaussian, another parametrization using Crystal Ball function is studied. From the left plot of figure A.6 it can be seen that the parametrization is better for Crystal Ball since it includes the tail in the negative region.

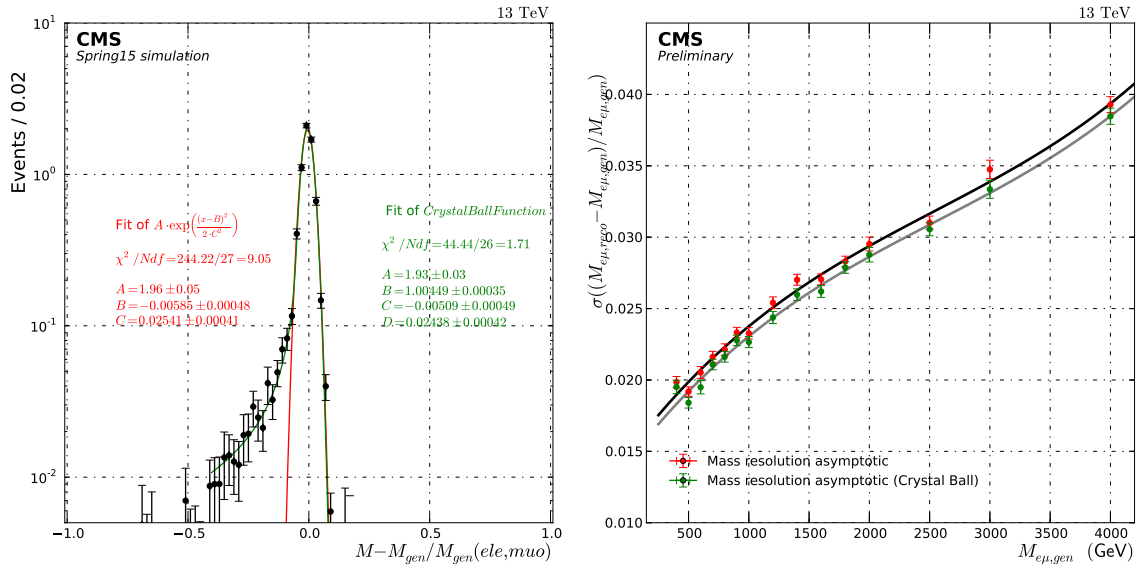


Figure A.6: Left plot : Parametrization of mass resolution for an example signal mass point of 1200 GeV using two different functions, Crystal Ball (in green) and Gaussian (in red). Right plot : Difference between invariant mass resolution using the two different parametrizations.

The right plot of figure A.6 shows the difference between the invariant mass resolution using the two different parametrization. Though the Crystal Ball performs better, the resulting difference in the mass resolution plot over the whole mass range is rather small. A Gaussian function is used in this analysis since the Crystall Ball fit is numerically unstable.

A.8 Additional Signal Efficiency Plots

In section 5.7.1, the distributions of signal efficiency (RPV-SUSY, QBH) are presented and discussed. Here, the remaining distribution of the Z' signal efficiency is shown in figure A.7. It is not included in section 5.7.1 because it is similar to the signal efficiency determined with RPV-SUSY samples. This resemblance of the shape and values of the signal efficiency between RPV-SUSY and Z' allows to treat the two signal models similarly (input, parametrization, mass range,...) in the limit setting procedure.

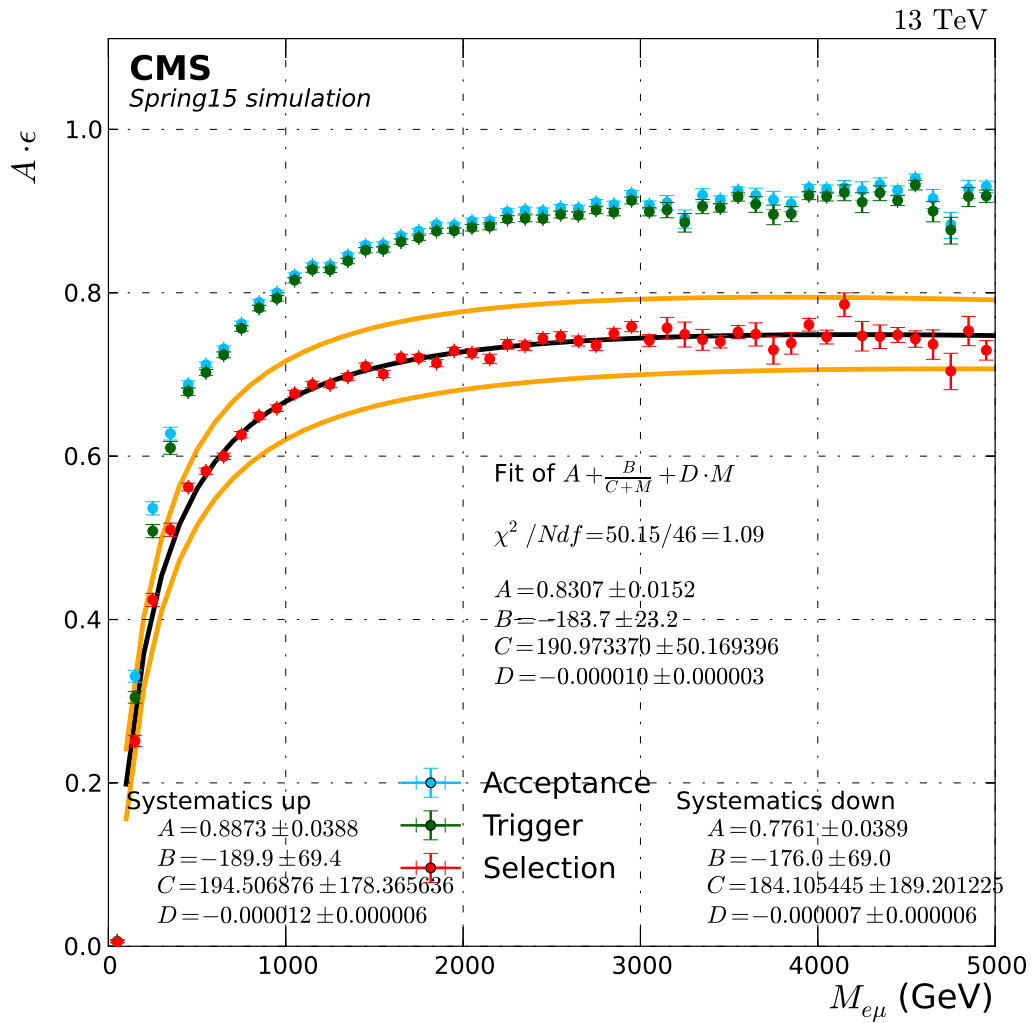


Figure A.7: Signal Efficiency determined with the Z' samples. The plateau of the efficiency is reached at ~ 1 TeV. The $A \times \epsilon \approx 75\%$ in the plateau region. One observes a similar shape of the signal efficiency as in the RPV-SUSY case.

Bibliography

- [1] **ATLAS** Collaboration, G. Aad *et al.*, “Search for a heavy narrow resonance decaying to $e\mu$, $e\tau$, or $\mu\tau$ with the ATLAS detector in $\sqrt{s} = 7$ TeV pp collisions at the LHC”, *Physics Letters B* **723** no. 13, (2013) 15 – 32. <http://www.sciencedirect.com/science/article/pii/S0370269313003249>.
- [2] **ATLAS** Collaboration, G. Aad *et al.*, “Search for a Heavy Neutral Particle Decaying to $e\mu$, $e\tau$, or $\mu\tau$ in pp Collisions at $\sqrt{s} = 8$ TeV with the ATLAS Detector”, *Phys. Rev. Lett.* **115** no. 3, (2015) 031801, [arXiv:1503.04430](https://arxiv.org/abs/1503.04430) [hep-ex].
- [3] **ATLAS** Collaboration, “Search for beyond the Standard Model phenomena in $e\mu$ final states in pp collisions at $\sqrt{s} = 13$ TeV with the ATLAS detector”, 2015. ATLAS-CONF-2015-072.
- [4] **CMS** Collaboration, “Search for Lepton Flavour Violating Decays of Heavy Resonances and Quantum Black Holes to electron/muon Pairs in pp Collisions at a centre of mass energy of 8 TeV”, 2015. CMS-PAS-EXO-13-002.
- [5] **SINDRUM II** Collaboration, W. H. Bertl *et al.*, “A Search for muon to electron conversion in muonic gold”, *Eur. Phys. J.* **C47** (2006) 337–346.
- [6] **COMET** Collaboration, Y. Kuno, “A search for muon-to-electron conversion at J-PARC: the COMET experiment”, *PTEP* **022C01** (2013) .
- [7] **DeeMe** Collaboration, Y. Nakatsugawa, “Search for Muon to Electron Conversion in Nuclear Field at J-PARC MLF”, *Nucl. Part. Phys. Proc.* **273-275** (2016) 1692–1698.
- [8] M. E. Peskin and D. V. Schroeder, *An introduction to quantum field theory*. Advanced book program. Westview Press Reading (Mass.), Boulder (Colo.), 1995. <http://opac.inria.fr/record=b1131978>. Autre tirage : 1997.
- [9] D. Griffiths, *Introduction to Elementary Particles*. Physics textbook. Wiley, 2008. <https://books.google.de/books?id=w9Dz56myXm8C>.
- [10] M. Czakon, “Quantum field theory: Lecture notes”, July, 2015. RWTH Aachen University.
- [11] M. Erdmann, “Particle Physics I and II: Lecture Notes .” RWTH Aachen University, 2014/2015.
- [12] C. Berger, *Elementarteilchenphysik: Von den Grundlagen zu den modernen Experimenten*. Springer, 2014.
- [13] D. H. Perkins, *Introduction to High Energy Physics*. University of Oxford, 2000.
- [14] “Standard Model of Elementary Particles”, 2013. https://en.wikipedia.org/wiki/File:Standard_Model_of_Elementary_Particles.svg.
- [15] B. Delamotte, “Group Theory: Lecture Notes.” Master 2 Noyaux Particules Astroparticules Cosmologie, 2014/2015.
- [16] S. Weinberg, “A model of leptons”, *Phys. Rev. Lett.* **19** (Nov, 1967) 1264–1266. <http://link.aps.org/doi/10.1103/PhysRevLett.19.1264>.

- [17] A. Salam, “Renormalizability of gauge theories”, *Phys. Rev.* **127** (Jul, 1962) 331–334.
<http://link.aps.org/doi/10.1103/PhysRev.127.331>.
- [18] CMS Collaboration, S. Chatrchyan *et al.*, “Observation of a new boson at a mass of 125 GeV with the CMS experiment at the LHC”, *Phys. Lett.* **B716** (2012) 30–61,
 arXiv:1207.7235 [hep-ex]. CMS-HIG-12-028, CERN-PH-EP-2012-220.
- [19] P. W. Higgs, “Spontaneous symmetry breakdown without massless bosons”, *Phys. Rev.* **145** (May, 1966) 1156–1163.
<http://link.aps.org/doi/10.1103/PhysRev.145.1156>.
- [20] F. Englert and R. Brout, “Broken symmetry and the mass of gauge vector mesons”, *Phys. Rev. Lett.* **13** (Aug, 1964) 321–323.
<http://link.aps.org/doi/10.1103/PhysRevLett.13.321>.
- [21] CMS Collaboration, “Combination of standard model Higgs boson searches and measurements of the properties of the new boson with a mass near 125 GeV”, Tech. Rep. CMS-PAS-HIG-13-005, CERN, Geneva, 2013.
<http://cds.cern.ch/record/1542387>.
- [22] CMS Collaboration, “Standard Model Physics Publication”, July, 2015.
<http://cms-results.web.cern.ch/cms-results/public-results/publications/SMP/index.html>.
- [23] Particle Data Group Collaboration, K. A. Olive *et al.*, “Review of Particle Physics, The CKM Quark-Mixing Matrix”, *Chin. Phys.* **C38** (2014) 090001.
- [24] Particle Data Group Collaboration, K. A. Olive *et al.*, “Review of Particle Physics, Neutrino Mixing”, *Chin. Phys.* **C38** (2014) 090001.
- [25] Particle Data Group Collaboration, K. A. Olive *et al.*, “Review of Particle Physics, Quantum Chromodynamics”, *Chin. Phys.* **C38** (2014) 090001.
- [26] G. F. Giudice, “Naturalness after LHC8”, *PoS EPS-HEP2013* (2013) 163,
 arXiv:1307.7879 [hep-ph]. CERN-PH-TH-2013-180.
- [27] G. Bertone, D. Hooper, and J. Silk, “Particle dark matter: evidence, candidates and constraints”, *Physics Reports* **405** no. 56, (2005) 279 – 390. <http://www.sciencedirect.com/science/article/pii/S0370157304003515>.
- [28] Planck Collaboration, P. A. R. Ade *et al.*, “Planck 2015 results. XIII. Cosmological parameters”, arXiv:1502.01589 [astro-ph.CO].
- [29] D. Clowe, M. Brada, A. H. Gonzalez, M. Markevitch, S. W. Randall, C. Jones, and D. Zaritsky, “A direct empirical proof of the existence of dark matter”, *The Astrophysical Journal Letters* **648** no. 2, (2006) L109.
<http://stacks.iop.org/1538-4357/648/i=2/a=L109>.
- [30] CMS Collaboration, “CMS Exotica Public Physics Results ”, <https://twiki.cern.ch/twiki/bin/view/CMSPublic/PhysicsResultsEXO>.
- [31] C. Wiebusch, “Astroteilchenphysik: Skript SS 2010.”. RWTH Aachen University.
- [32] Particle Data Group Collaboration, K. A. Olive *et al.*, “Review of Particle Physics, Supersymmetry: Part 1”, *Chin. Phys.* **C38** (2014) 090001.

- [33] **Particle Data Group** Collaboration, J. Beringer *et al.*, “Review of particle physics”, *Phys. Rev. D* **86** (Jul, 2012) 010001.
<http://link.aps.org/doi/10.1103/PhysRevD.86.010001>.
- [34] R. Barbier *et al.*, “R-parity violating supersymmetry”, *Phys. Rept.* **420** (2005) 1–202, [arXiv:hep-ph/0406039](https://arxiv.org/abs/hep-ph/0406039) [hep-ph].
- [35] H. K. Dreiner, C. Luhn, and M. Thormeier, “What is the discrete gauge symmetry of the minimal supersymmetric standard model”, *Phys. Rev. D* **73** (Apr, 2006) 075007.
<http://link.aps.org/doi/10.1103/PhysRevD.73.075007>.
- [36] **Particle Data Group** Collaboration, K. A. Olive *et al.*, “Review of Particle Physics, Structure Functions”, *Chin. Phys.* **C38** (2014) 090001.
- [37] H. K. Dreiner, S. Grab, M. Kramer, and M. K. Trenkel, “Supersymmetric NLO QCD corrections to resonant slepton production and signals at the Tevatron and the CERN LHC”, *Phys. Rev.* **D75** (2007) 035003, [arXiv:hep-ph/0611195](https://arxiv.org/abs/hep-ph/0611195) [hep-ph].
- [38] T. G. Rizzo, “ Z' phenomenology and the LHC”, [arXiv:hep-ph/0610104](https://arxiv.org/abs/hep-ph/0610104) [hep-ph]. <https://arxiv.org/abs/hep-ph/0610104>.
- [39] L. Randall and R. Sundrum, “A large mass hierarchy from a small extra dimension”, *Phys. Rev. Lett.* **83** (1999) 3370–3373, [arXiv:hep-ph/9905221](https://arxiv.org/abs/hep-ph/9905221) [hep-ph].
- [40] N. Arkani-Hamed, S. Dimopoulos, and G. R. Dvali, “The Hierarchy problem and new dimensions at a millimeter”, *Phys. Lett.* **B429** (1998) 263–272, [arXiv:hep-ph/9803315](https://arxiv.org/abs/hep-ph/9803315) [hep-ph].
- [41] X. Calmet and N. Gausmann, “Non-thermal quantum black holes with quantized masses”, *Int. J. Mod. Phys.* **A28** (2013) 1350045, [arXiv:1209.4618](https://arxiv.org/abs/1209.4618) [hep-ph].
- [42] X. Calmet, D. Fragkakis, and N. Gausmann, “Non Thermal Small Black Holes”, in *Black Holes: Evolution, Theory and Thermodynamics*, A. J. Bauer and D. G. Eifel, eds., p. 165. 2012. [arXiv:1201.4463](https://arxiv.org/abs/1201.4463) [hep-ph].
- [43] G. Dvali, C. Gomez, and S. Mukhanov, “Black Hole Masses are Quantized”, [arXiv:1106.5894](https://arxiv.org/abs/1106.5894) [hep-ph].
- [44] L. Evans and P. Bryant, “LHC Machine”, *Journal of Instrumentation* **3** no. 08, (2008) .
<http://stacks.iop.org/1748-0221/3/i=08/a=S08001>.
- [45] C. Lefèvre, “The CERN accelerator complex. Complexe des accélérateurs du CERN.” Dec, 2008.
- [46] L. Taylor, “CMS detector design”, 2011.
<http://cms.web.cern.ch/news/cms-detector-design>.
- [47] **CMS** Collaboration, “The CMS experiment at the CERN LHC”, *Journal of Instrumentation* **3** no. 08, (2008) S08004.
<http://stacks.iop.org/1748-0221/3/i=08/a=S08004>.
- [48] **CMS** Collaboration, V. Karimki *et al.*, *The CMS tracker system project: Technical Design Report*. Technical Design Report CMS. CERN, Geneva, 1997.
<http://cds.cern.ch/record/368412>.

- [49] CMS Collaboration, *The CMS electromagnetic calorimeter project: Technical Design Report*. Technical Design Report CMS. CERN, Geneva, 1997.
<http://cds.cern.ch/record/349375>.
- [50] P. Adzic, “Energy resolution of the barrel of the cms electromagnetic calorimeter”, *Journal of Instrumentation* **2** no. 04, (2007) P04004.
<http://stacks.iop.org/1748-0221/2/i=04/a=P04004>.
- [51] V.V. Abramov et al., “Studies of the response of the prototype CMS hadron calorimeter, including magnetic field effects, to pion, electron, and muon beams”, *Nuclear Instruments and Methods in Physics Research Section A: Accelerators, Spectrometers, Detectors and Associated Equipment* **457** no. 12, (2001) 75 – 100. <http://www.sciencedirect.com/science/article/pii/S0168900200007117>.
- [52] CMS Collaboration, “Precise mapping of the magnetic field in the CMS barrel yoke using cosmic rays”, *Journal of Instrumentation* **5** no. 03, (2010) T03021.
<http://stacks.iop.org/1748-0221/5/i=03/a=T03021>.
- [53] CMS Collaboration, “The performance of the CMS muon detector in proton-proton collisions at $\sqrt{s} = 7$ TeV at the LHC”, 2011. CMS PAPER MUO-11-001.
- [54] CMS Collaboration, “The muon project: Technical design report.” 1997.
- [55] CMS Collaboration, S. Cittolin, A. Rácz, and P. Spiccas, *CMS The TriDAS Project: Technical Design Report, Volume 2: Data Acquisition and High-Level Trigger. CMS trigger and data-acquisition project*. Technical Design Report CMS. CERN, Geneva, 2002.
<http://cds.cern.ch/record/578006>.
- [56] I. Bird *et al.*, “LHC Computing Grid: Technical Design Report”, 2005.
- [57] CMS Collaboration, G. Abbiendi *et al.*, “Muon Reconstruction in the CMS Detector.” CMS Analysis Note AN-2008-97, 2008.
- [58] CMS Collaboration, M. Chen *et al.*, “Search for New High-Mass Resonances Decaying to Muon Pairs in the CMS Experiment.” CMS Analysis Note AN-2007-38, 2007.
- [59] CMS Collaboration, “Baseline muon selections for Run-II”, 2016.
<https://twiki.cern.ch/twiki/bin/view/CMS/SWGuideMuonIdRun2>.
- [60] CMS Collaboration, S. S. Chhibra *et al.*, “Single muon trigger studies for high-pT muons: Presentation in the Dimuon meeting.”
https://indico.cern.ch/event/460554/contributions/1131268/attachments/1184020/1715836/Zprime_Mu50TrgEff_9Nov2015.pdf.
- [61] CMS Collaboration, G. L. Bayatian *et al.*, *CMS Physics: Technical Design Report Volume 1: Detector Performance and Software*. Technical Design Report CMS. CERN, Geneva, 2006. <https://cds.cern.ch/record/922757>.
- [62] CMS Collaboration, “Electron and Photon Physics Object Offline Guide”, 2013.
<https://twiki.cern.ch/twiki/bin/view/CMSPublic/SWGuideEgamma>.
- [63] CMS Collaboration, “Performance of electron reconstruction and selection with the CMS detector at $\sqrt{s} = 8$ TeV.” 2014.

- [64] S. Baffioni, C. Charlot, F. Ferri, D. Futyan, P. Meridiani, I. Puljak, C. Rovelli, R. Salerno, and Y. Sirois, “Electron reconstruction in CMS”, *The European Physical Journal C* **49** no. 4, (2007) 1099–1116. <http://dx.doi.org/10.1140/epjc/s10052-006-0175-5>.
- [65] CMS Collaboration, S. Chatrchyan *et al.*, “Alignment of the CMS tracker with LHC and cosmic ray data”, *JINST* **9** (2014) P06009, arXiv:1403.2286 [physics.ins-det].
- [66] CMS Collaboration, “Gsf electron object, CMS twiki.” 2010.
- [67] CMS Collaboration, “Search for high-mass resonances and quantum black holes in the $e\mu$ final state in proton-proton collisions at $\sqrt{s} = 13$ TeV”, http://cms.cern.ch/iCMS/jsp/db_notes/noteInfo.jsp?cmsnoteid=CMS%20AN-2015/191.
- [68] CMS Collaboration, “CMS Luminosity Measurement for the 2015 Data Taking Period”, CMS Physical Analysis Summary: CMS-PAS-2015/001.
- [69] T. Sjöstrand, S. Mrenna, and P. Skands, “PYTHIA 6.4 physics and manual”, *Journal of High Energy Physics* **2006** no. 05, (2006) 026. <http://stacks.iop.org/1126-6708/2006/i=05/a=026>.
- [70] S. Frixione, P. Nason, and C. Oleari, “Matching NLO QCD computations with Parton Shower simulations: the POWHEG method”, *JHEP* **11** (2007) 070, arXiv:0709.2092 [hep-ph].
- [71] T. Stelzer and W. Long, “Automatic generation of tree level helicity amplitudes”, *Computer Physics Communications* **81** no. 3, (1994) 357 – 371. <http://www.sciencedirect.com/science/article/pii/0010465594900841>.
- [72] S. Frixione and B. R. Webber, “Matching NLO QCD computations and parton shower simulations”, *Journal of High Energy Physics* **2002** no. 06, (2002) 029. <http://stacks.iop.org/1126-6708/2002/i=06/a=029>.
- [73] A. Belyaev, N. D. Christensen, and A. Pukhov, “Calcchep 3.4 for collider physics within and beyond the standard model”, *Computer Physics Communications* **184** no. 7, (2013) 1729 – 1769. <http://www.sciencedirect.com/science/article/pii/S0010465513000313>.
- [74] T. Sjöstrand, S. Mrenna, and P. Skands, “A brief introduction to PYTHIA 8.1”, *Computer Physics Communications* **178** no. 11, (2008) 852 – 867. <http://www.sciencedirect.com/science/article/pii/S0010465508000441>.
- [75] D. M. Gingrich, “Monte Carlo event generator for black hole production and decay in proton-proton collisions QBH version 1.02”, *Computer Physics Communications* **181** no. 11, (2010) 1917 – 1924. <http://www.sciencedirect.com/science/article/pii/S0010465510002602>.
- [76] S. Agostinelli *et al.*, “Geant4a simulation toolkit”, *Nuclear Instruments and Methods in Physics Research Section A: Accelerators, Spectrometers, Detectors and Associated Equipment* **506** no. 3, (2003) 250 – 303. <http://www.sciencedirect.com/science/article/pii/S0168900203013688>.

- [77] CMS Collaboration, A. Lanyov, “High-pT ID and Tracker-based Isolation Efficiency using Tag Probe for Run2015: Presentation in the Muon POG meeting.” https://indico.cern.ch/event/465390/contributions/1141124/attachments/1197504/1741010/Lanyov_Highpt_eff_TnP_01.12.2015.pdf.
- [78] CMS Collaboration, W. Fang *et al.*, “HEEP6.0 scale factor study after primary vertex weight for 25ns: HEEP + DiMuon meeting”, 2015. https://indico.cern.ch/event/453282/contributions/1117975/attachments/1169324/1687354/ScaleFactorStudy_25ns.pdf.
- [79] PVT group, “Pileup reweighting.” https://twiki.cern.ch/twiki/bin/view/CMS/PileupJSONFileforData#2015_%Pileup_JSON_Files.
- [80] CMS Collaboration, “HEEP Electron ID and isolation”, 2016. <https://twiki.cern.ch/twiki/bin/view/CMS/HEEPElectronIdentificationRun2>.
- [81] CMS Collaboration, S. Harper and C. Shepherd-Themistocleous, “Improving Sigma Eta Eta.” https://indico.cern.ch/event/27560/contributions/1618477/attachments/499353/689807/sigmaEtaEta_sharper.pdf.
- [82] CMS Collaboration, S. Harper and C. Shepherd-Themistocleous, “Improving Sigma Eta Eta: Showershape Studies.” <https://indico.cern.ch/event/27573/contributions/1618731/attachments/499754/690382/e2x5Endcap.pdf>.
- [83] CMS Collaboration, “Search for new physics, focused on W' production, in the single electron/muon plus missing-Et final states using ppcollision data at $\sqrt{s} = 13$ TeV.” 2015.
- [84] JETMET POG, “MET Filters for Run II.” <https://twiki.cern.ch/twiki/bin/view/CMS/MissingETOptionalFiltersRun2>.
- [85] CMS Collaboration, S. Chatrchyan *et al.*, “Measurement of the electron charge asymmetry in inclusive W production in pp collisions at $\sqrt{s} = 7$ TeV”, *Phys. Rev. Lett.* **109** (2012) 111806, arXiv:1206.2598 [hep-ex]. CMS-SMP-12-001, CERN-PH-EP-2012-151.
- [86] CMS Collaboration, S. Chatrchyan *et al.*, “Measurement of the lepton charge asymmetry in inclusive W production in pp collisions at $\sqrt{s} = 7$ TeV”, *JHEP* **04** (2011) 050, arXiv:1103.3470 [hep-ex]. CERN-PH-EP-2011-024, CMS-EWK-10-006.
- [87] CMS Collaboration, B. Clerbaux *et al.*, “Dielectron resonance search in Run 2 at $\sqrt{s} = 13$ TeV pp collisions.” CMS Note: AN-2015/222, 2015.
- [88] CMS Collaboration, “Muon Resolution twiki: Muon POG”, 2015. <https://twiki.cern.ch/twiki/bin/view/CMS/MuonReferenceResolution>.
- [89] CMS Collaboration, “Performance of CMS muon reconstruction in pp collisions at $\sqrt{s} = 7$ TeV.” <https://twiki.cern.ch/twiki/bin/view/CMS/MuonRecoPerformance2010>.
- [90] CMS Collaboration, “Talk at the Muon POG, 22 May 2015.” https://indico.cern.ch/event/396030/contributions/941047/attachments/793548/1087719/cosmics_talkv2.pdf.
- [91] CMS Collaboration, “Search for High-Mass Resonances Decaying to Muon Pairs in pp Collisions at $\sqrt{s} = 13$ TeV.” CMS Note: AN-2015/223, 2015.

- [92] J. Butterworth *et al.*, “PDF4LHC recommendations for LHC Run II”, *J. Phys.* **G43** (2016) 023001, arXiv:1510.03865 [hep-ph].
- [93] CMS Collaboration, “Standard Model Cross Sections for CMS at 13 TeV.” <https://twiki.cern.ch/twiki/bin/viewauth/CMS/StandardModelCrossSection%sat13TeV>.
- [94] B. D. Pecjak, D. J. Scott, X. Wang, and L. L. Yang, “Resummed differential cross sections for top-quark pairs at the LHC”, *Phys. Rev. Lett.* **116** no. 20, (2016) 202001, arXiv:1601.07020 [hep-ph].
- [95] G. Cowan, *Statistical Data Analysis*. Oxford University Press, 1998. <http://opac.inria.fr/record=b1131978>.
- [96] J. S. Conway, “Incorporating Nuisance Parameters in Likelihoods for Multisource Spectra”, in *Proceedings, PHYSTAT 2011 Workshop on Statistical Issues Related to Discovery Claims in Search Experiments and Unfolding, CERN, Geneva, Switzerland 17-20 January 2011*, pp. 115–120. 2011. arXiv:1103.0354 [physics.data-an]. <https://inspirehep.net/record/891252/files/arXiv:1103.0354.pdf>.
- [97] A. D. Christophe Andrieu, Nando De Freitas and M. I. Jordan, “An Introduction to MCMC for Machine Learning”, 2003.
- [98] CMS Collaboration, “Documentation of the RooStats -based statistics tools for Higgs PAG”, https://twiki.cern.ch/twiki/bin/viewauth/CMS/SWGuideHiggsAnalysisCombinedLimit#MarkovChainMC_algorithm.
- [99] RooStats Collaboration, “RooStats page in CMS, Twiki”, 2012. <https://twiki.cern.ch/twiki/bin/view/CMS/RooStats>.
- [100] A. Belyaev and X. Calmet, “Quantum Black Holes and their Lepton Signatures at the LHC with CalCHEP”, *JHEP* **08** (2015) 139, arXiv:1412.2661 [hep-ph].
- [101] ATLAS Collaboration, “Search for new phenomena in different-flavour high mass dilepton final states in pp collisions at a centre-of-mass energy of 13 TeV with the ATLAS detector.” <https://atlas.web.cern.ch/Atlas/GROUPS/PHYSICS/PAPERS/EXOT-2015-20>.
- [102] CMS Collaboration, S. Chatrchyan *et al.*, “Search for microscopic black holes in pp collisions at $\sqrt{s} = 8$ TeV”, *JHEP* **07** (2013) 178, arXiv:1303.5338 [hep-ex].
- [103] CMS Collaboration, V. Khachatryan *et al.*, “Search for resonances and quantum black holes using dijet mass spectra in proton-proton collisions at $\sqrt{s} = 8$ TeV”, *Phys. Rev.* **D91** no. 5, (2015) 052009, arXiv:1501.04198 [hep-ex].
- [104] CMS Collaboration, V. Khachatryan *et al.*, “Search for narrow resonances decaying to dijets in proton-proton collisions at $\sqrt{s} = 13$ TeV”, *Phys. Rev. Lett.* **116** no. 7, (2016) 071801, arXiv:1512.01224 [hep-ex].
- [105] J. Sato and M. Yamanaka, “A way to crosscheck μ - e conversion in the case of no signals of $\mu \rightarrow e\gamma$ and $\mu \rightarrow 3e$ ”, *Phys. Rev.* **D91** (2015) 055018, arXiv:1409.1697 [hep-ph].

- [106] J. Sato and M. Yamanaka, “Way to crosscheck $\mu - e$ conversion in the case of no signals of $\mu \rightarrow e\gamma$ and $\mu \rightarrow 3e$ ”, *Phys. Rev. D* **91** (Mar, 2015) 055018.
<http://link.aps.org/doi/10.1103/PhysRevD.91.055018>.
- [107] J. Erler, P. Langacker, S. Munir, and E. Rojas, “Improved Constraints on Z-prime Bosons from Electroweak Precision Data”, *JHEP* **08** (2009) 017, [arXiv:0906.2435](https://arxiv.org/abs/0906.2435) [hep-ph].
- [108] X. Calmet, S. D. H. Hsu, and D. Reeb, “Quantum gravity at a TeV and the renormalization of Newton’s constant”, *Phys. Rev.* **D77** (2008) 125015, [arXiv:0803.1836](https://arxiv.org/abs/0803.1836) [hep-th].
- [109] X. Calmet, “Virtual Black Holes, Remnants and the Information Paradox”, *Class. Quant. Grav.* **32** no. 4, (2015) 045007, [arXiv:1412.6270](https://arxiv.org/abs/1412.6270) [gr-qc].
- [110] D. Berdine, N. Kauer, and D. Rainwater, “Breakdown of the Narrow Width Approximation for New Physics”, *Phys. Rev. Lett.* **99** (2007) 111601, [arXiv:hep-ph/0703058](https://arxiv.org/abs/hep-ph/0703058) [hep-ph].

Acknowledgements

I would very much like to thank my supervisor Prof. Thomas Hebbeker for giving me the opportunity to work in the field of particle physics. I am very thankful that Prof. Christopher Wiebusch agreed to be the second corrector of this thesis.

I would express my thankfulness to all members of the team that contributed to this analysis. I thank Dr. Arnd Meyer for continuously sharing his physical insights. The other members of this team, namely Sören Erdweg, Andreas Güth and Swagata Mukherjee, always helped with their knowledge and experience during the entire time of this work. I profited a lot from the expertise and spirit of this team.

I very much like to thank all other members of the institute, who made the time at the institute very pleasant. I want to mention those, who I directly worked with: Andreas Albert, Fabian Bispinck, Michael Brodski, Deborah Duchardt, Matthias Endres, Thomas Esch, Simon Knutzen, Viktor Kutzner, Jonas Lieb, Marcel Materok, Markus Merschmeyer, Philipp Millet, Mark Olschewski, Klaas Padeken, Tobias Pook, Markus Radziej, Jonas Roemer, Daniel Theyssier and Sebastian Thüer.

The analysis of this thesis is part of the CMS collaboration, consisting of thousands of physicist around the world. Clearly, without the infrastructure and resources provided by the collaboration and its members this work could have never been done.

Last but not least, I very much like to thank my family and friends for supporting me unconditionally.

